WAVE-CISK IN A BAROCLINIC BASIC STATE

by

Thomas Nehrkorn

Vordiplom, Universität Hamburg

(1978)

M.S., Colorado State University

(1981)

SUBMITTED IN PARTIAL FULFILLMENT
OF THE REQUIREMENTS OF THE
DEGREE OF

DOCTOR OF PHILOSOPHY

IN METEOROLOGY

at the

MASSACHUSETTS INSTITUTE OF TECHNOLOGY

February 1985

Signature of Author _____
Department of Earth, Atmospheric, and Planetary Science
November 15, 1984

Certified by _____
Kerry A. Emanuel
Thesis Supervisor

Accepted by _____
Theodore R. Madden
Chairman, Departmental Committee on Graduate Students

Wave - CISK in a Baroclinic Basic State

by

Thomas Nehrkorn

Submitted to the Department of Earth, Atmospheric and Planetary Science on November 15, 1984 in partial fulfillment of the requirements for the degree of Doctor of Philosophy in Meteorology.

ABSTRACT

Prefrontal squall lines are mesoscale convective systems that often cannot be linked to any preexisting organizing mechanism. This suggests the possibility that they are self-forced disturbances, driven by a cooperative interaction between convective and larger scales. To investigate this hypothesis, a wave-CISK model is developed for two-dimensional disturbances in a baroclinic basic state with constant vertical wind shear. The governing equations are the linearized Boussinesq equations for an inviscid and hydrostatic fluid on an f-plane. The model domain is infinite in the horizontal and consists of two layers in the vertical, representing the troposphere and the stratosphere. The model troposphere has constant static stability and wind shear, and the stratosphere has a larger static stability and no wind shear. The convective heating is confined to the troposphere. Normal mode solutions are assumed and the convective heating is parameterized in the standard CISK fashion: its vertical structure is specified, and it is set proportional to the low level vertical velocity. The model allows for arbitrary orientations of the disturbance axis.

Results show the existence of two modes: large scale Eady modes, which are amplified slightly by heating, and smaller scale wave-CISK modes. The Eady modes are found to have their largest growth rates on the baroclinic axis, i.e. with the disturbance axis perpendicular to the shear vector. Wavelengths of maximum growth are on the synoptic scale (on the order of 3600 km). The wave-CISK modes have their maximum growth rates near the symmetric axis, i.e. with disturbance axes approximately parallel to the shear vector. For heating amplitudes that are not unrealistically large, wavelengths of maximum growth are finite and on the mesoscale (on the order of 500 km).

Sensitivity experiments for these wave-CISK modes show that the value of the maximum growth rate and the wavelength of maximum growth are not very sensitive to the form of the vertical heating profile, while other characteristics of the fastest growing mode are. In particular, the orientation of the disturbance axis depends on the heating profile: for maximum heating in the middle troposphere the disturbance axis is rotated 20°-30° clockwise from the symmetric axis, implying upshear propagation, while for higher levels of maximum heating the disturbance is more nearly aligned with the shear vector or rotated slightly in the opposite direction. If low level cooling is included in the heating profile, disturbance axes are rotated further counterclockwise. The phase speeds

of the fastest growing modes are larger for higher levels of maximum heating, due to the basic state shear component in the direction of propagation. Variations of the heating amplitude, the stratospheric static stability, and the bulk Richardson number show a tendency for a clockwise rotation as the heating amplitude and the stratospheric stability are decreased, and the Richardson number is increased. The growth rate and the wavenumber of the fastest growing mode are found to decrease with decreasing static stability of the stratosphere, and to be approximately proportional to the magnitude of the basic state wind shear.

Comparisons with observations of squall lines in the atmosphere show some aspects of the solution, such as its vertical structure, to be in qualitative agreement. The orientation angle of the fastest growing mode, however, is near to observed values only if heating profiles with heating maxima at upper levels and cooling at lower levels are used. Predicted phase speeds of these modes are too high by a factor of two to five. The wave-CISK theory, at least in its current formulation, is thus unable to account for the observed characteristics of squall lines.

Thesis Supervisor: Dr. Kerry A. Emanuel

Title: Assistant Professor of Meteorology

Table of Contents

Acknowledgements

I would like to thank my advisor, Dr. Kerry Emanuel, for his guidance and support throughout this thesis. I am also indebted to my other committee members, Dr. Fred Sanders, Dr. Peter Stone, and Dr. Ka-Kit Tung, for helpful suggestions and discussions. Valuable suggestions concerning the numerical method were provided by Dr. Keith Seitter. Figures were drafted by Michael Rocha and Isabelle Kole. Most of the calculations were carried out at the National Center for Atmospheric Research (NCAR). NCAR is supported by the National Science Foundation.

List of Figures

Fig. 4.8: As Fig. 4.6, but for the reference run Eady mode with z_m=0.5, at ℓ=1.75 and α=30°.

Fig. 4.9: As Fig. 4.6, but for the reference run Eady mode with z_m=0.5, at ℓ=1.75 and α=-30°.

Fig. 4.10: As Fig. 4.6, but for the reference run Eady mode with z_m=0.8, at ℓ=1.75 and α=90°.

Fig. 4.11: Results for the wave-CISK mode, for the reference run with z_m=0.5. Growth rate (a) and phase speed (b) are shown as a function of total wavenumber. Curves are labeled with the value of the angle α.

Fig. 4.12: As Fig. 4.11, but for z_m=0.6.

Fig. 4.13: As Fig. 4.11, but for z_m=0.7.

Fig. 4.14: As Fig. 4.11, but for z_m=0.8.

Fig. 4.15: Vertical structure and energetics for the wave-CISK mode, for the reference run with z_m=0.8, at ℓ=10 and α=0°. Contour plots of the nondimensional ψ'(a),u'(b), p'(c), and b'(d), normalized by their maximum value in the domain (given at the bottom of each panel). The dashed line in a) indicates an angular momentum surface. e): energy conversion terms as a function of height, normalized by the maximum value. f): vertically integrated energy budget.

Fig. 4.16: As Fig. 4.15, but for ℓ=6.

Fig. 4.17: As Fig. 4.15, but for z_m=0.5.

Fig. 4.18: As Fig. 4.15, but for α=+10°.

Fig. 4.19: As Fig. 4.15, but for α=-10°.

Fig. 4.20: As Fig. 4.15, but for z_m=0.5, at ℓ=14 and α=-30°.

Fig. 4.21: As Fig. 4.11, but for E=70% and z_m=0.5.

Fig. 4.22: As Fig. 4.11, but for E=70% and z_m=0.8.

Fig. 4.23: Characteristics of the fastest growing wave-CISK mode as a function of the precipitation efficiency E. Shown are the growth rate $-\sigma_{i,max}$ (thin solid line), the phase speed c_{max} (thick solid line), and the wavelength ℓ_{max} (dashed line). All curves are labeled by the value of z_m.

Fig. 4.24: As Fig. 4.11, but for N_s/N_t=1 and z_m=0.5.

Fig. 4.25: As Fig. 4.11, but for N_s/N_t=1 and z_m=0.8.

Fig. 4.26: As Fig. 4.11, but for N_s/N_t=10 and z_m=0.5.

Fig. 4.27: As Fig. 4.11, but for N_s/N_t=10 and z_m=0.8.

Fig. 4.28: As Fig. 4.11, but for N_s/N_t=1000 and z_m=0.5.

Fig. 4.29: As Fig. 4.11, but for N_s/N_t=1000 and z_m=0.8.

Fig. 4.30: As Fig. 4.11, but for mode N for positive angles, for N_s/N_t=1000 and z_m=0.5.

Fig. 4.31: As Fig. 4.11, but for mode N for negative angles, for N_s/N_t=1000 and z_m=0.5.

Fig. 4.32: As Fig. 4.11, but for mode N for positive angles, for N_s/N_t=1000 and z_m=0.8.

Fig. 4.33: As Fig. 4.11, but for mode N for negative angles, for N_s/N_t=1000 and z_m=0.8.

Fig. 4.34: As Fig. 4.23, but for the fastest growing wave-CISK mode as a function of the nondimensional stratospheric Brunt-Väisälä frequency, N_s/N_t.

Fig. 4.35: As Fig.4.11, but for Ri=1.3 and z_m=0.5

Fig. 4.36: As Fig.4.11, but for Ri=1.3 and z_m=0.8

Fig. 4.37: As Fig.4.11, but for Ri=50 and z_m=0.5

Fig. 4.38: As Fig.4.11, but for Ri=50 and z_m=0.8

Fig. 4.39: As Fig.4.23, but for the fastest growing wave-CISK mode as a function of the bulk Richardson number, Ri.

Fig. 4.40: The heating profile, as modified by downdraft cooling, for z_m=0.8 and β=0 (solid line), β=1/6 (dashed line), and β=1/3 (dash-dotted line).

Fig. 4.41: Contour plot of growth rate for case of downdraft cooling; a): E=75%, β=1/6, b): E=60%, β=1/3. Plotting conventions same as in Fig. 4.1.

Fig. 5.1: Mean hodographs in squall line relative coordinates. The arrow indicates the cell motion. From Bluestein and Jain (1984).

Fig. 5.2: Standard deviations of the mean hodographs in squall line relative coordinates. Solid line is the cross-line, dashed line the along-line component. From Bluestein and Jain (1984).

Fig. 5.3: Mean hodograph and associated standard deviations (solid line u, dashed line v) in squall line relative coordinates for all 64 cases. Data taken from Wyss and Emanuel (1984).

Fig. 5.4: As Fig. 5.3, but for the 20 case subsample with more nearly linear shear. Data taken from Wyss and Emanuel (1984).

1. Introduction

Deep convection in the atmosphere is frequently organized on a scale fundamentally larger than the cloud scale itself, but smaller than the synoptic scale. This range of scales constitutes the so-called mesoscale. The mesoscale organization can take the form of circular or line-shaped features. The former, referred to as clusters in the tropics and mesoscale convective complexes (MCCs) in midlatitudes, occur in an environment that is characterized by weak shear, whereas squall lines are found in a strongly sheared environment. Midlatitude squall lines are classified into those that coincide with surface cold fronts (frontal squall lines) and those that occur ahead of cold fronts, in the warm sector of baroclinic cyclones (prefrontal squall lines).

Since prefrontal squall lines do not require a preexisting organizing mechanism, such as frontogenetical forcing, for their formation, the possibility exists that they are self-excited disturbances in which a mesoscale circulation and smaller scale, convective heat sources feed on each other and lead to an ampliflifying disturbance. This hypothesis will be investigated here with a linear wave-CISK[1] model, in which the larger, mesoscale motions are resolved explicitly and the effects of convection are parameterized as a heat source. The convection will be assumed to respond instantaneously to the large scale forcing, which is represented by the vertical velocity at some level. Wave-CISK models, which are discussed in more detail in the next chapter, have been used by a number

---

1) CISK - Conditional Instability of the Second Kind

of investigators for tropical disturbances, especially easterly waves. Midlatitude applications have been proposed for large-scale circulations (Mak,1982), thunderstorms (Raymond,1975), and squall lines (Emanuel,1982). Emanuel assumed a baroclinic basic state with constant wind shear, and considered two-dimensional disturbances whose axes are aligned with the wind shear vector.

In the following, a generalized version of Emanuel's wave-CISK model that allows for cross-line shear is used to investigate the susceptibility of linear shear flow on an f-plane to wave-CISK instability.

The background literature about prefrontal squall lines and wave-CISK theory are reviewed in the next chapter. The model equations are discussed in chapter 3, and the results of this model are presented in chapter 4. Growing modes are found that are convectively amplified baroclinic instability modes, and other modes that constitute the extension of the symmetric wave-CISK modes to general orientation angles. The wave-CISK modes are compared to observations of squall lines in chapter 5, and chapter 6 contains the summary and conclusions. The details of the numerical procedures are given in Appendix A, and adiabatic growing modes at low Richardson numbers are discussed in Appendix B.

2. Background

Observations indicate that prefrontal squall lines typically occur eighty to fivehundred kilometers ahead of a surface cold front. Their spatial dimensions are on the order of several hundred kilometers in length, and one hundred kilometers or less in width (Breiland,1958 and Fulks,1958). Newton (1950) summarized the observations made during The Thunderstorm project. Prefrontal squall lines were found to form at or above a surface cold front and subsequently move out ahead of it, or to from in situ in the warm sector. In the latter case, Breiland (1958) found that this occurs where low-level winds have a confluence zone. This location typically also is on the anticyclonic side of the upper level jet stream. The propagation speed of prefrontal squall lines is faster than that of the surface cold front, and their orientation is to within 45° to the left of the wind direction in the lower and middle troposphere. Squall lines are found to be either of a cellular character with a series of distinct convection cells, or to consist of a more nearly two-dimensional circulation.

Because of the nearly two-dimensional structure, mean streamlines of a two-dimensional circulation in the plane perpendicular to the squall line have been constructed by a number of investigators (Newton, 1950, 1966; Browning and Ludlam, 1962; Ogura and Liou, 1982). The main feature of all these cross sections is a strong updraft which originates at the leading edge of the line at low levels and tilts back, i.e. upshear with height. An attempt to explain this upshear tilt with a conservation of horizontal momentum argument was made by Newton (1950) and supported by more recent observations by Ogura and Liou (1980).

Heavy precipitation and severe weather events are concentrated at the

leading edge of the squall line. Behind the leading edge is the main downdraft of the squall line. In cases where the squall line has a steering level, the midlevel inflow of this downdraft occurs at the rear of the system. This is evident in a cross section in Newton (1950). If the squall line moves faster than the environmental flow at all levels, the downdraft inflow must come from the front of the system. This is the case in some tropical squall lines (Zipser, 1977); Ogura and Liou (1980) documented a midlatitude case where a substantial part of the downdraft air originated ahead of the line. Thermodynamic considerations point to middle levels for the source region of the downdraft, and to low levels for the updraft air source region. The resulting draft structure for these propagating squall lines is then inherently three-dimensional, and two-dimensional analyses cannot be expected to accurately reflect parcel motions. In particular, equivalent potential temperature will not be conserved along mean two-dimensional streamlines. A characteristic feature of tropical squall lines is a large area of mesoscale ascent in the anvil behind the leading edge; this anvil contributes a significant part of the total precipitation of the system. The squall line studied by Ogura and Liou also had a trailing anvil that produced precipitation in the decaying phase of the system. It is unclear at this point how common the mesoscale area of stratiform precipitation is in midlatitude squall lines, and what role it plays in their dynamics.

The surface pressure variations associated with squall lines, and other forms of intense convection, have been documented by a number of investigators. Large amplitude (several mb) pressure waves have been observed in connection with convective lines, in cases where the squall lines extend across the surface warm front into the cold sector (e.g.,

Miller and Sanders, 1980). In the case studied by Miller and Sanders the pressure waves propagated at approximately 15 m/s, which was about 5 m/s faster than the suqall lines. Lindzen and Tung (1976) suggested that such pressure waves represent ducted gravity waves in the cool, stable boundary layer air. They concluded that for efficient ducting, the air above the boundary layer needs to be conditionally unstable and contain wind shear with a critical level. Even in the absence of ducted waves, however, squall line passages are associated with characteristic pressure signatures: the pressure tends to be lower several tens of kilometers ahead of the system (Hoxit et al., 1976), and rise sharply immediately before the onset of precipitation. A slight pressure fall is observed after the passage of the squall line. A part of this variation, especially the sharp pressure rise, is certainly due to convective scale effects, but part of it occurs on the mesoscale. Hoxit et al. (1976) attributed the pressure minimum ahead of the system to upper level subsidence from thunderstorm outflow.

Based on the observational evidence, a number of hypotheses have been advanced to explain the formation of squall lines. Most of these relate squall line formation to some synoptic scale forcing mechanism, such as confluence lines in the warm sector, or a downgliding motion of air along the cold frontal surface that would force low level convergence ahead of the cold front. Another hypothesis is that the boundary of cold air from thunderstorm outflows acts like a pseudo cold front, the dynamics of which can be understood in terms of density current theory. Newton and Newton (1959) showed that a pure density current can only account for about half the observed propagation speed of squall lines, however. They related the excess speed to vertical transports of horizontal momentum by

the cumulus clouds, which would act to accelerate the line by mixing down high cross-line momentum (in the case of substantial cross-line shear), or high along-line momentum (in the case of mostly along-line shear), which in turn would lead to cross-line Coriolis accelerations.

Theoretical models of squall lines have concentrated on and exploited their apparent two-dimensionality. Nonlinear, analytical models have been constructed by Moncrieff and coworkers for two-dimensional and steady state conditions. Moncrieff (1981) summarized the results and differentiated steering level and propagating squall lines. The propagating squall lines have a three-dimensional structure which was implicitly included in the analytical model by separately considering the interlocking up- and downdrafts. In the steering level case the modeled circulation was strictly two-dimensional. The two different types of convective overturning were found to correspond to different values of a convective Richardson number, which is a measure of the convective available potential energy (the positive area of a lifted parcel on a thermodynamic diagram) and the environmental shear. A major inconsistency of this theory in the case of the steering level squall line was the predicted downshear slope of the updraft, which does not agree with the observations and which is also inconsistent with the steady state assumption because precipitation would be falling into the updraft inflow, thus destroying the buoyancy of the updraft air. Thorpe, Miller and Moncrieff (1982) were able to produce persistent storms with the correct updraft slope in a two-dimensional, time-dependent numerical model by concentrating the wind shear in the lower levels. Schlesinger (1973) and Hane (1973) were also able to simulate fairly persistent convection with

upshear sloping updrafts in two-dimensional numerical convection models. Seitter and Kuo (1983) used a two-dimensional model to demonstrate a possible mechanism for producing the upshear tilt. They suggested that the asymmetric deceleration of the updraft by liquid water loading, which is strongest at the upshear edge of the updraft at low levels, together with the evaporation of rain, are responsible for the tilt of the updraft. Seitter and Kuo (1983) also noted a basic problem with two-dimensional convection models: since environmental air cannot flow around penetrating clouds in the model, as it does at least partially in nature, it is forced to descend from the top of the model. This subsidence leads to warming at midlevels, which will eventually suppress the convection unless the initial state is altered by artificially reducing the static stability and/or the storm relative-flow at upper levels.

Three-dimensional simulations with numerical models have been attempted both with convective scale models, which explicitly resolve cloud motions, and with synoptic or mesoscale models that parameterize the effects of cumulus clouds in terms of large scale variables. The former, e.g. Wilhelmson and Klemp (1981), relate squall line formation to the interaction of cold outflow boundaries from decaying storms with those of other storms and the environmental flow. The latter emphasize larger scale forcing, such as confluence zones, amplified by convective feedback (e.g., Chang et al., 1981). Attempts to resolve cumulus convection and still have sufficiently large model domains for mesoscale simulations have been restricted by limitations of computing resources that inevitably lead to compromises on resolution and/or three-dimensionality.

Linearized models use a somewhat different approach. They are based on the hypothesis that mesoscale convective features are manifestations of a constructive interaction between motions on the convective and larger scale. This concept was first introduced in connection with hurricane formation by Charney and Eliassen (1964) and Ooyama (1964). The positive feedback mechanism was labeled CISK (Conditional Instability of the Second Kind). In these studies, cumulus convection was assumed to be driven by frictional boundary layer convergence of the hurricane depression, and the latent heat release associated with the convection then led to a deepening of the cyclone, with correspondingly increased boundary layer convergence.

Wave-CISK models differ from traditional CISK in that the convergence fields of inviscid wave motions are used as a forcing mechanism for cumulus convection. As in traditional CISK, cumulus convection is incorporated as a heat source, the vertical distribution of which is specified a priori. Motions on the larger scale are resolved explicitly with a set of linearized equations of motion, and normal mode solutions are then substituted. Growth rates and phase speeds of these modes are obtained as the eigenvalues of the problem.

Most wave-CISK models were developed to account for the easterly waves in the tropics, as described by Reed and Recker (1971). A review of these studies, which generally use the equatorial beta-plane approximation, can be found in Davies (1979). Growing modes are found that correspond to the free modes of the tropical atmosphere described by Matsuno (1966). The main problem of these wave-CISK results is the fact that growth rates are predicted to increase monotonically with wavenumber, implying that the fastest growing disturbance is that with the shortest possible wavelength. This is in contradiction to the implicit assumption

that there is a clear scale separation between the resolved motions on the larger scale and the parameterized convective motions. Another problem is the relatively small value of the growth rates at observed wavenumbers, and the strong sensitivity of the results to the details of the convective parameterization.

A number of modifications to the basic wave-CISK model have been proposed. To introduce a scale selection mechanism a frequency dependent heating formulation was introduced by Hayashi (1971); other authors placed additional constraints on the system, such as time lags in the response of the cumulus heating to forcing (Lindzen,1974; Kuo,1975; Davies,1979). Uncertainties in the choice of values for these additional parameters prevented these approaches from completely resolving the problem, however.

Since squall line environments are characterized by strong wind shear, any theory of squall line formation and maintenance should consider this effect. The wind shear of the basic state was included in a wave-CISK model by Raymond (1975,1976), in which the rotation of the earth was neglected. In his model, midlatitude thunderstorms were represented as wave packets of internal gravity waves, and their movement was predicted from group velocity calculations for a given wind profile. Comparisons between computed and observed movement of thunderstorms showed poor agreement for multicell storms, while the range of possible velocities was correctly predicted for continuously propagating thunderstorms.

In a modified wave-CISK model, Raymond (1983) resolved the motions of the cloud free air explicitly, and parameterized the effects of convection as mass sources and sinks (rather than heat sources). He identified modes

that propagated against the shear direction, and faster growing modes that advected with the wind at some level. The advective modes were found to exist only when strong convective downdrafts were included in the parameterization scheme. In a more recent paper, Raymond (1984) implemented the wave-CISK model in an initial value problem in a two-dimensional model. He found that the advective mode serves to initiate the squall-line; after its decay due to the depletion of the moisture supply, the storm split into two propagating modes that moved in opposite directions. The downshear propagating mode had a steering level in the upper part of the domain, and its features agreed roughly with those observed by Ogura and Liou (1980). The upshear propagating mode was regarded as a spurious mode which does not occur in nature because it would be subject to strong storm-relative midlevel flow, which would ventilate the storm with low θ_e air.

Mak (1982) and Moorthi (1983) included the effects of the earth's rotation in their wave-CISK models, but they assumed quasi-geostrophic conditions. Thus their models are limited to larger scale applications, such as rapidly intensifying extratropical cyclones or monsoon depressions.

A mesoscale wave-CISK model that included the effects of a basic state wind shear and the earth's rotation was developed by Emanuel (1982). He considered motions on an f-plane, linearized about a basic state with a constant vertical shear of the horizontal wind. He restricted his attention to the special case of a two-dimensional disturbance whose axis is aligned with the basic state wind shear. It should be noted that although the mesoscale circulations were assumed to be two-dimensional, the parameterization of cumulus convection implies

mass exchanges between streamlines, and thus three-dimensional air motions. His model domain consisted of a "troposphere" with a linear wind profile and constant static stability, and a "stratosphere" with zero wind shear and a different static stability. The cumulus heating was confined to the lower layer. He found growing solutions for heating amplitudes that are subcritical with respect to wave-CISK in a barotropic basic state. For nonzero static stability differences between stratosphere and troposphere, his model showed two growth rate peaks at finite wavenumbers, one at long wavelengths and one at mesoscale wavelengths. The long wave mode was very sensitive to the symmetric stability of the basic state, but was not greatly influenced by differing static stability increases at the tropopause. The mesoscale mode, on the other hand, was less sensitive to the symmetric stability, but it depended on a partial wave-reflecting region for its growth. Both modes propagated toward the warm air, the mesoscale mode at a speed typical of a gravity wave that is confined to the lower half of the domain. Their growth rates were fairly insensitive to the form of the vertical heating profile. They were too small to account for the rapid development of squall lines, however.

The existing wave-CISK models appropriate for mesoscale phenomena thus either do not incorporate the earth's rotation, or they do not allow for cross-line shear. Emanuel's (1982) results indicate that the baroclinicity of the basic flow provides an important destabilizing mechanism that leads to a finite wavelength of fastest growth, suggesting that the Coriolis force has a nonnegligible effect on the dynamics of the perturbations. Since observations of squall lines show cross-line as well as along-line shear of the environmental flow, the effects of cross-line

shear on the symmetric wave-CISK modes of Emanuel (1982) are investigated in the following. A generalized version of Emanuel's model is developed by allowing for arbitrary orientation angles of the disturbance, and more general heating profiles. This model is also used to calculate adiabatic and convectively amplified baroclinic instability modes.

3. Model Description

3.1 Governing Equations

I assume a Boussinesq, inviscid, incompressible and hydrostatic fluid on an f - plane. The governing perturbation equations, linearized about a basic state with constant Brunt - Väisälä frequency and constant shear in the u - component of the wind are given by

$$u'_t + Uu'_x + U_z w' = fv' - p'_x/\rho_o \tag{3.1a}$$

$$v'_t + Uv'_x = -fu' - p'_y/\rho_o \tag{3.1b}$$

$$u'_x + v'_y + w'_z = 0 \tag{3.1c}$$

$$b' = p'_z/\rho_o \tag{3.1d}$$

$$b'_t - fU_z v' + Ub'_x + N^2 w' = Q' \quad , \tag{3.1e}$$

where subscripts denote partial derivatives, primes denote perturbation quantities, capital letters the basic state variables, $b'=-g\rho'/\rho_o$ is the perturbation buoyancy, Q' the heating, and ρ_o the mean value of the basic state density $\bar{\rho}$. Here I made use of the following relations governing the basic state:

$$U_z = \frac{g}{f}\frac{\partial \ln\bar{\rho}}{\partial y} \quad ; \quad N^2 = -\frac{g}{\rho_o}\frac{\partial \bar{\rho}}{\partial z} \quad . \tag{3.2}$$

For a two-dimensional disturbance we can obtain a more convenient form of the equations by rotating the coordinate system counterclockwise by an

angle α such that its x-axis is aligned with the axis of the disturbance. The new coordinates are related to the old ones (denoted by stars) by

$$\begin{aligned} x &= x^*\cos\alpha + y^*\sin\alpha \\ y &= -x^*\sin\alpha + y^*\cos\alpha \\ z &= z^* \\ t &= t^* \end{aligned} \qquad , \tag{3.3}$$

and the equations now take the form

$$u'_t - U\sin\alpha u'_y + U_z\cos\alpha w' = fv' \tag{3.4a}$$

$$v'_t - U\cos\alpha v'_y - U_z\sin\alpha w' = -fu' - p'_y/\rho_o \tag{3.4b}$$

$$v' = -\psi'_z \quad ; \quad w' = \psi'_y \tag{3.4c}$$

$$b' = p'_z/\rho_o \tag{3.4d}$$

$$b'_t - U\sin\alpha b'_y - fU_z\sin\alpha u' - fU_z\cos\alpha v' + N^2w' = Q' \quad . \tag{3.4e}$$

Fig. 3.1 shows a sketch of the new coordinate system in relation to the baroclinic and symmetric axis. Note that, by definition, the x derivative of a perturbation quantity vanishes; correspondingly an angle of $0°$ denotes a symmetric and an angle of $\mp 90°$ a baroclinic disturbance.

The model domain is infinite in horizontal extent and consists of two regions in the vertical: a lower layer ($0<z<H$), the model troposphere, with constant wind shear and static stability, and an upper layer ($H<z<\infty$), the model stratosphere, with a different static stability and zero wind shear. The cumulus heating is confined to the model troposphere. After assuming normal mode solutions of the form

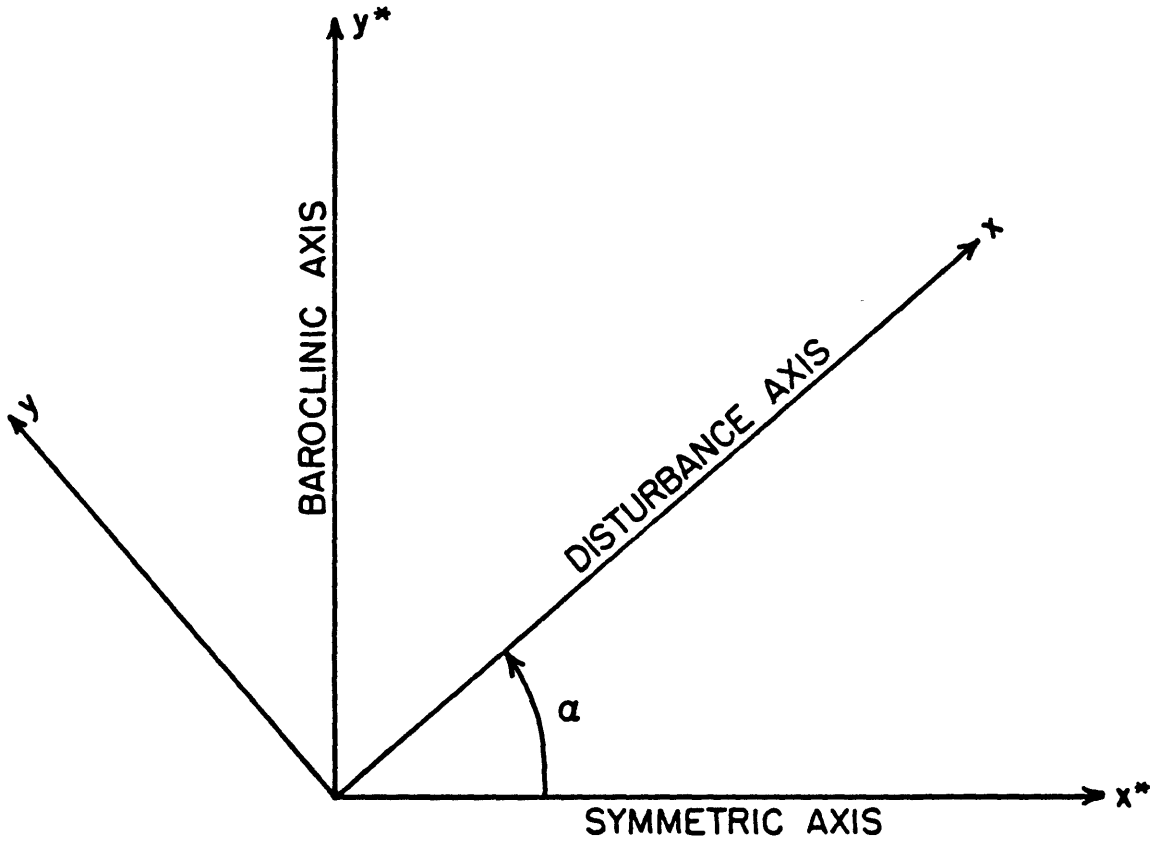

Fig. 3.1: The coordinate system in relation to the symmetric and baroclinic axis.

$$\psi'(y,z,t) = \mathrm{Re}\{\psi(z)e^{i(\ell y + \sigma t)}\} \tag{3.5}$$

for all perturbation quantities, we can form a single equation in the streamfunction amplitude $\psi(z)$ for the two layers:

$$\{(\sigma - U_z\sin\alpha\ell z)^2 - f^2\}\psi_{zz} + \{\frac{-2\ell f^2 U_z\sin\alpha}{\sigma - U_z\sin\alpha\ell z} - 2i\ell f U_z\cos\alpha\}\psi_z$$
$$+ \{N_t^2\ell^2 - \frac{2i\ell^2 f U_z^2\sin\alpha\cos\alpha}{\sigma - U_z\sin\alpha\ell z}\}\psi = -i\ell Q \qquad \text{for } 0<z<H \tag{3.6}$$

and

$$\{(\sigma - U_z\sin\alpha\ell)^2 - f^2\}\psi + N_s^2\ell^2\psi = 0 \qquad \text{for } H<z. \tag{3.7}$$

It should be noted here that (3.6) and (3.7) could have been derived without performing the coordinate transformation (3.3). In that case the exponent in (3.5) would take the form $(kx^* + \lambda y^*)$, where $k=-\ell\sin\alpha$ and $\lambda=\ell\cos\alpha$. Correspondingly, $-k$ and λ would take the place of $\ell\sin\alpha$ and $\ell\cos\alpha$ in (3.6) and (3.7). As discussed in more detail in section 3.3, the equations are closed by parameterizing the cumulus heating as

$$Q' = N_t^2 Q_0 G(z) w'(z_0) \quad , \text{ or } \quad i\ell Q = -N_t^2\ell^2 Q_0 G(z)\psi(z_0) \quad . \tag{3.8}$$

Finally, the quantities are nondimensionalized, as in Emanuel(1982), by:

$$z^* = Hz$$
$$y^* = HRi^{1/2}N_t f^{-1}\pi^{-1}y \qquad (3.9)$$
$$t^* = Ri^{1/2}f^{-1}t \quad ,$$

where stars denote dimensional quantities, and $Ri=N_t^2/U_z^2$ is the Richardson number of the model troposphere. The nondimensional equations now take the form

$$\{Ri - (\sigma - b\sin\alpha\ell z)^2\}\psi_{zz} + \{\frac{2Rib\sin\alpha\ell}{\sigma - b\sin\alpha\ell z} + 2\pi i\ell\cos\alpha\}\psi_z$$
$$- \{\pi^2\ell^2 - \frac{2\pi ib\ell^2\sin\alpha\cos\alpha}{\sigma - b\sin\alpha\ell z}\}\psi = -\pi^2\ell^2 Q_0 G(z)\psi(z_0) \qquad \text{for } 0<z<1 \qquad (3.10)$$

and

$$\{Ri - (\sigma - b\sin\alpha\ell)^2\}\psi_{zz} - (N_s/N_t)^2\pi^2\ell^2\psi = 0 \qquad \text{for } 1<z \qquad (3.11)$$

where $b\equiv\pi Ri^{-1/2}$ (not to be confused with the perturbation buoyancy).

Equation (3.10) has singularities where the dimensional (nondimensional) Doppler-shifted frequency is equal to 0, and $\mp f$ ($Ri^{1/2}$). Jones(1967) considered the propagation of neutral waves (real σ) through these critical levels. In the case of growing modes with complex frequencies there are no singularities in the domain, but for small enough growth rates the coefficients of the differential equation may exhibit near singular behavior at levels where the real part of the Doppler-shifted frequency is equal to 0 or $\mp f$. At these levels

$$c = \sigma_r/\ell = S/\ell + b\sin\alpha z \quad ,$$

where $S=0$ or $\mp Ri^{1/2}$. For the critical level to be within the domain, the phase velocity has to lie between the limits

$$S/\ell < c < S/\ell + b\sin\alpha \quad ,$$

where the direction of the inequality has to be reversed for negative α.

3.2 Boundary Conditions and Method of Solution

As boundary conditions we impose

$$\psi = 0 \quad \text{at } z = 0 \tag{3.12}$$

and a radiation condition at $z=\infty$. Solutions for the lower and upper layer are matched at the layer interface by requiring the vertical displacement and the perturbation pressure to be continuous across $z=1$. Since the horizontal basic state velocity is continuous, the condition of a continuous vertical displacement is equivalent to requiring the perturbation streamfunction to be continuous. Thus

$$\psi(1-) = \psi(1+) \quad . \tag{3.13}$$

The perturbation pressure can be expressed in terms of the streamfunction and its vertical derivative, as shown in (3.21). This results in the condition

$$-\frac{1}{X}\left\{\frac{Ri - X^2}{\pi\ell}\psi_z\right\}_{z=1+} = -\frac{1}{X}\left\{\frac{Ri - X^2}{\pi\ell}\psi_z + (i\cos\alpha - \frac{b\sin\alpha X}{\pi})\psi\right\}_{z=1-} ,$$

where $X=\sigma-b\sin\alpha z$. After a rearrangement of terms, this can be written as

$$\psi_z(1-) = \psi_z(1+) - (\frac{i\cos\alpha - b\sin\alpha X/\pi}{Ri - X^2})\pi\ell\psi(1) \quad . \tag{3.14}$$

The fact that the vertical wind shear, and thus the horizontal density gradient, is discontinuous at the layer interface places another restriction on the solution. The magnitude of the density discontinuity across the tropopause may be estimated as follows. Consider two parcels of fluid, at initially equal densities, just above and below the tropopause. If these parcels are displaced horizontally, their densities will differ by

$$\delta\rho_T^* = \frac{\partial\bar{\rho}}{\partial y^*}\delta y^* + \frac{\partial\bar{\rho}}{\partial x^*}\delta x^*$$

where δx^* and δy^* are the (dimensional) displacements in the x- and y-direction, respectively. Since in the current model this density discontinuity is not taken into account, the parcels are implicitly assumed to undergo a density change of this magnitude when crossing the tropopause. This assumption is only justifiable if this change in density due to the infinitesimal vertical displacement across the layer interface is small compared to the density changes due to the finite vertical displacements within the layers, which are given by

$$\delta\rho_I^* = \frac{\partial\bar{\rho}}{\partial z^*}\delta z^* \quad .$$

This will be true if both contributions to $\delta\rho_T^*$ are small compared to $\delta\rho_I^*$:

$$\frac{\delta z^*}{\delta y^*} \gg \left(\frac{\partial\bar{\rho}}{\partial y^*}\right)\left(\frac{\partial\bar{\rho}}{\partial z^*}\right)^{-1} \quad ; \quad \frac{\delta z^*}{\delta x^*} \gg \left(\frac{\partial\bar{\rho}}{\partial x^*}\right)\left(\frac{\partial\bar{\rho}}{\partial z^*}\right)^{-1} . \tag{3.15}$$

This is equivalent to requiring that parcel trajectories be steep compared to isentropes. We can further express the displacements in normal mode form:

$$\{\delta x^*, \delta y^*, \delta z^*\} = -i(\sigma^* + U\sin\alpha\ell^*)^{-1} \{u^*, v^*, w^*\} e^{i(\ell^* y^* + \sigma^* t^*)} .$$

Finally, by making use of (3.2) and the nondimensionalizations (3.9), (3.23) and (3.24), the conditions (3.15) can be expressed as follows:

$$\ell \gg \cos\alpha \tag{3.16a}$$

$$\ell \gg \frac{|u|}{|\psi|}\frac{\sin^\alpha}{\pi} \quad . \tag{3.16b}$$

It has to be verified ex posteriori if these conditions are satisfied for a particular solution.

Solutions to the governing equation (3.11) in the stratosphere can be obtained analytically. The solution for the upper layer, taking into account the radiation condition at $z=\infty$, can be written as

$$\psi = A_s e^{ir_s(z-1)} \quad , \tag{3.17}$$

where

$$r_s = (N_s/N_t)\pi\ell(-S_s)^{-1/2}\,\mathrm{sign}\left[\mathrm{Im}(-S_s)^{-1/2}\right]$$

and

$$S_s = Ri - (\sigma - b\sin\alpha\ell)^2 \quad .$$

With this solution the matching conditions at z=1 can be combined to form one upper boundary condition for (3.10):

$$\psi_z(1-) = \{ir_s - \pi\ell(\frac{i\cos\alpha - b\sin\alpha(\sigma - b\sin\alpha\ell)/\pi}{S_s})\}\psi(1-) \quad . \qquad (3.18)$$

The system of equations (3.10) and (3.11) with the boundary conditions (3.12) and (3.18) has some useful symmetry properties. If σ is an eigenvalue for the problem for a certain wavenumber ℓ and angle α, so is $-\sigma$ for the same wavenumber and angle $-\alpha$. Futhermore, for $\alpha = \mp 90°$, the complex conjugate of an eigenvalue is also an eigenvalue of the problem. This implies that an eigenvalue σ at an angle of 90° corresponds to the eigenvalue $-\sigma^c$ at an angle of -90°,as it must, since it has the same growth rate and the same phase speed with respect to the environmental flow.

There is no analytical solution to (3.10), so that I need to integrate the equation numerically. When written in finite difference form, (3.10) with boundary conditions (3.12) and (3.18) form a matrix equation. To find the eigenvalue σ a generalized matrix eigenvalue problem is solved. The details of the numerical integration and iteration schemes are described in Appendix A.

3.3 Heating Formulation

The form of the cumulus heating chosen here (see (3.8)) follows from the basic CISK concept that the amount of convection is directly controlled by the low level (moisture) convergence of the larger scale circulations. An implicit assumption is that the space and time scales of resolved and convective motions are clearly separated so that the convective heating can be considered to respond immediately and in situ to the larger scale forcing. Furthermore, a spatially uniform conditional instability of the environment, represented by the heating amplitude Q_o, is necessary for the low level forcing to be effective in triggering convection.

There are several weaknesses of this kind of heating parameterization. A very obvious one is the existence of "negative clouds", i.e. regions of negative heating in regions of low level subsidence. This is not a very serious problem, however, since we can always add an arbitrary constant to the heating without affecting the result. Fig. 3.2 shows a comparison between the currently used, unconditional heating after the addition of the constant $Q_o(Q_1)$, and a conditional heating formulation with amplitude $2Q_o(Q_2)$. There are only minor differences between the two.

Some investigators have modified the heating formulation by introducing a high frequency filter (Hayashi, 1971, Davies, 1979) or by directly relating the heating only to the slowly varying part of the large scale forcing (Mak,1982). Although both these approaches yielded the desired result, namely a short wave cutoff, I did not use them in this model because they are hard to justify physically.

Finally, the sensitivity of the results of some wave-CISK studies to the form of the specified vertical profile of the heating has raised the

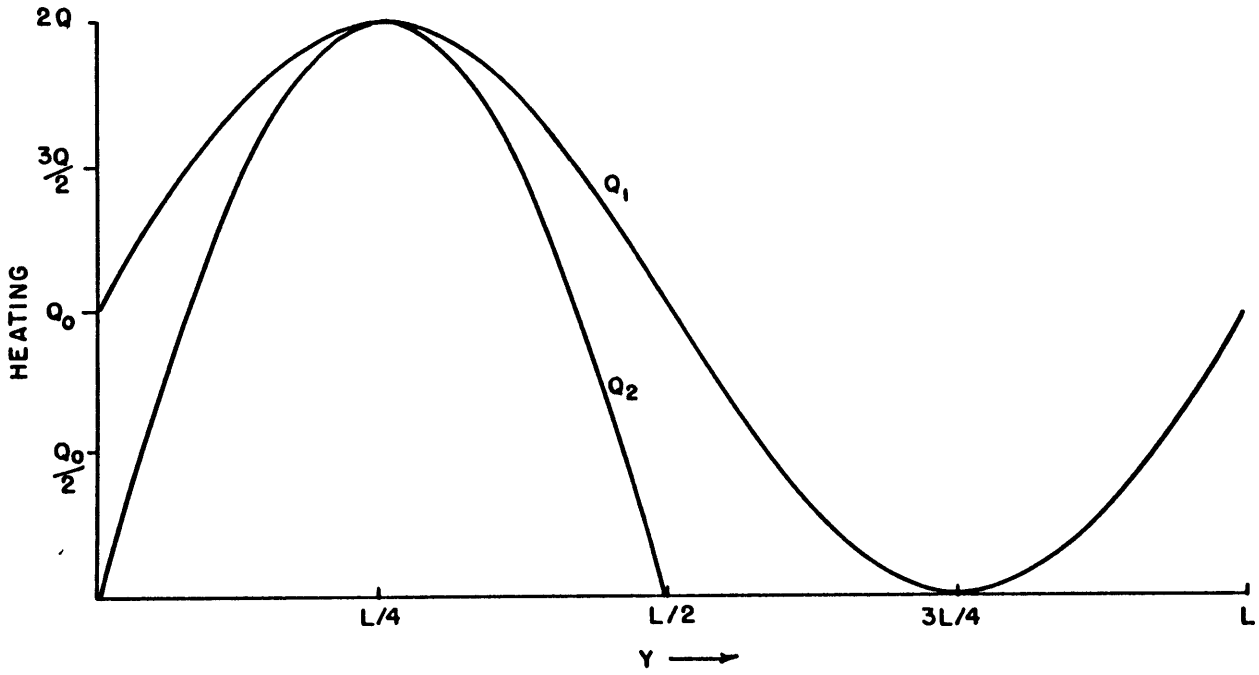

Fig. 3.2: Convective heating over one wavelength, for the case of unconditional (Q_1) and conditional (Q_2) heating.

question what kind of profile should be used, or if it should be specified at all. A cumulus parameterization that does not require such a specification is the scheme developed by Arakawa and Schubert (1974, hereafter referred to as A-S). It differs in more than one aspect from the simple CISK parameterization: the large scale forcing is not represented by the vertical velocity at a single level, but by the destabilization of the environment at all levels. Calculations for the GATE dataset by Lord (1982) showed that the large scale destabilization is mainly in the form of upper level cooling. The vertical profile of the heating is obtained as a result of a spectral cloud model, which classifies the different cloud types according to their fractional entrainment rates, together with a closure assumption that the large scale destabilization for each cloud type is balanced by the stabilizing effects of all other cloud types. Cumulus clouds are thus assumed to be in a quasi-equilibrium such that any large scale destabilization is counteracted by convective scale overturning, and the conditional instability for each cloud type remains constant on the short time scale.

Results from this parameterization show a tendency to overpredict warming at low levels and underpredict it at high levels (Lord,1982). A linearized version of the A-S scheme was used by Stark (1976) and Moorthi (1983). Stark could not obtain any growing wave-CISK modes without increasing the heating amplitude to unrealistic values. As was shown by Moorthi, the convective heating tends to be nearly in phase with the vertical velocity at all levels with the A-S parameterization, a situation not conducive to growing, propagating modes (Bolton,1980). This may explain Stark's result, but it does not provide a valid basis for adopting or rejecting the A-S parameterization. This has to be sought in the

underlying physical concept, namely the assumption that convection is controlled by the rate of large scale destabilization. This is not an appropiate assumption for the case of intense convection in midlatitude squall lines, which is characterized by a rapid consumption of buoyant energy that has been built up over a much longer time scale (see Fritsch et al.,1976). The forcing by low level vertical motions, which is instrumental in overcoming the potential barriers in the form of low level inversions or stable layers, is likely to exert more of a control on convective activity than any destabilization at upper levels, which will only add to an already large amount of buoyant energy available to parcels that reach the level of free convection. For this reason I will not adopt the A-S scheme and instead determine the sensitivity of my results to the specified vertical heating profile. I choose

$$G(z) = \frac{1}{Q_n} e^{az} \sin \pi z \quad , \tag{3.19}$$

where the normalization factor Q_n is chosen such that the area under the curve is the same for all a:

$$Q_n = \frac{1 + e^a}{2(1 + a^2/\pi^2)} \quad .$$

For different choices of the parameter a, the level of maximum heating will be at different levels between 0 and 1. Fig. 3.3 shows heating profiles for maximum heating levels between 0.5 and 0.8. In Emanuel (1982) a sinusoidal profile, i.e. a=0, was used.

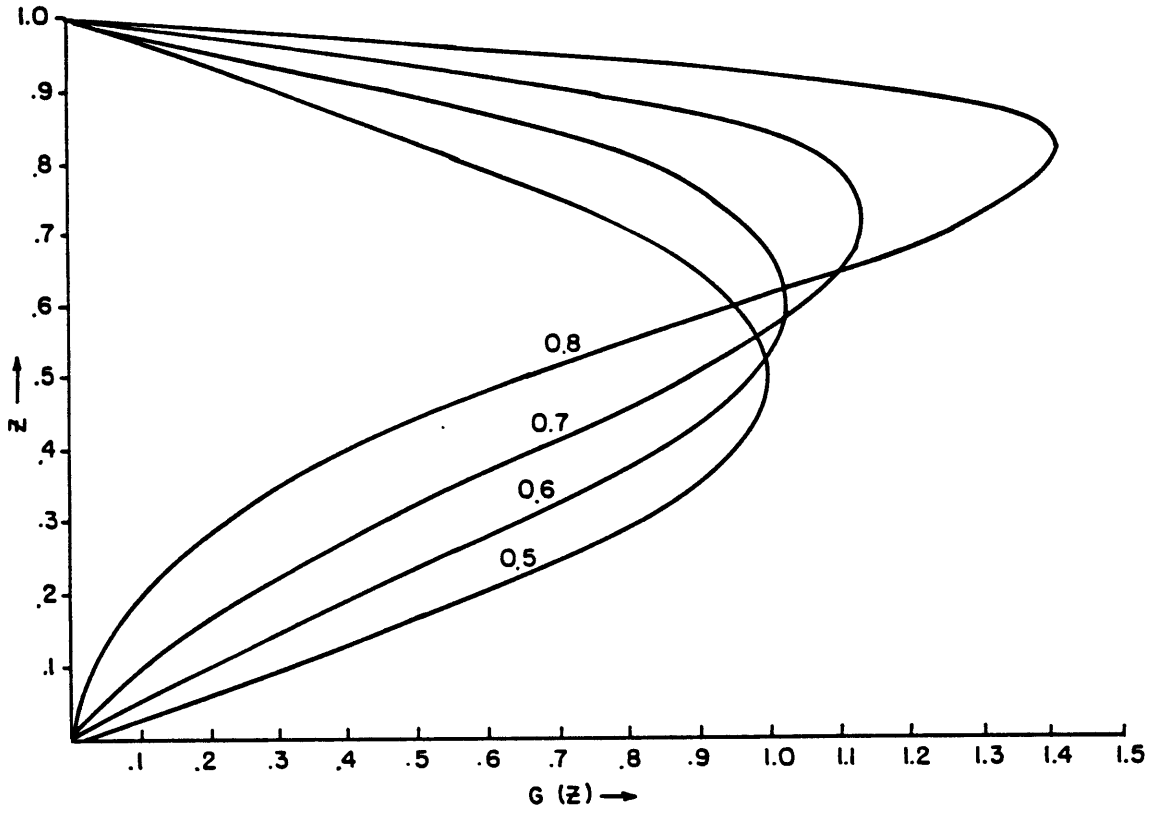

Fig. 3.3: Vertical heating profile G(z) from eq.(3.19) for different values of a. Curves are labeled with the level of maximum heating, z_m.

To obtain an estimate for the value of the heating amplitude Q_o, Emanuel used observed values for the maximum heating rate and the large scale vertical velocity at low levels, and solved for Q_o from (3.8). As Fig. 3.2 shows, the maximum heating corresponds to an amplitude of $2Q_o$ in the case of unconditional cumulus heating. Using values obtained by Reed and Recker (1971) for waves in the equatorial western Pacific, and taking into account the aforementioned factor of 2, Emanuel suggested a value of Q_o=0.971.

An alternative estimate may be obtained by considering the moisture budget of the squall line. The dimensional heating Q' in (3.8) is due to the release of latent heat of condensation:

$$Q' = (c-e)gL_v/(T_o c_p) \quad ,$$

where c and e are the rate of condensation and evaporation per unit mass, respectively. Assuming no horizontal divergence of water substance, the total heating, integrated vertically over a column of air, is related to the rate of precipitation out of that column:

$$\int_0^H Q'dz = \frac{gL_v}{T_o c_p}\int_0^H (c-e)dz = \frac{gL_v}{T_o c_p} P \quad .$$

If one further assumes that the supply of moisture comes from the mesoscale convergence below the level z_o, one can define a precipitation efficiency E as the ratio of precipitation rate to moisture supply rate as follows:

$$E = \frac{P}{(wq)_{z_o}} \quad .$$

Note that the precipitation rate and the vapor flux are mesoscale quantities and thus represent an average over a mesoscale area containing several individual precipitation cells. The resulting precipitation efficiency is related to the precipitation efficiency of the invidual cells by a factor which is the fraction of the total net moisture flux that ascends in the cells. Thus, the mesoscale precipitation efficiency will be equal to the convective efficiency if there is no net moisture flux in the cloud free region, it will be greater if there is net downward flux, and smaller if there is net upward flux in the cloud free region.

To relate the mesoscale precipitation effiency to the heating amplitude we substitute for P:

$$\int_0^H Q'dz = \frac{gL_v}{T_o c_p} (w'q')_{z_o} E \quad .$$

Further substituting for Q' from (3.8), where again the factor 2 is taken into account, yields

$$2N_t^2 w'(z_o) Q_o \int_0^H G(z)dz = \frac{gL_v}{T_o c_p} (w'q')_{z_o} E \quad ,$$

or finally, after substituting for G(z),

$$Q_o = E\ h/2 \quad ,$$

where

$$h = \frac{\pi g L_v q(z_o)}{2 c_p T_o N_t^2 H} \quad .$$

Choosing representative midlatitude values of H=10 km, $N_t = .96 \times 10^{-2}$ s^{-1}, and a water vapor mixing ratio at 1 km of 12 g/kg, yields h=1.942. For this value of h, a Q_o of 0.971 corresponds to a mesoscale precipitation effiency of 100%. While the exact value of h may vary depending on actual values of water vapor mixing ratios and static stability, I will use the above value of h in the calculation of Q_o throughout this thesis. Different environmental conditions may then be taken into account by corresponding changes in the precipitation efficiency.

3.4 Eigenfunctions and Energetics

Once a solution for the eigenvalue σ and the corresponding eigenfunction ψ has been found, the other perturbation quantities are determined as well. By combining equations (3.4a) - (3.4d) we can express u', b', and p' in terms of ψ; making use of the normal mode approach (3.5) and the nondimensionalization (3.9) allows us to express the nondimensional normal mode amplitudes u, p, b as follows

$$u = (iRi^{1/2}\psi_z - \pi Ri^{-1/2}\cos\alpha\ell\psi)/X \qquad \text{for } 0<z<1$$

$$u = iRi^{1/2}\psi_z/X \qquad \text{for } 1<z \tag{3.20}$$

$$p = -\left\{\frac{Ri - X^2}{\pi\ell}\psi_z + (i\cos\alpha - \frac{b\sin\alpha X}{\pi})\psi\right\}/X \qquad \text{for } 0<z<1 \tag{3.21}$$

$$
\begin{aligned}
p &= -\left\{\frac{Ri - X}{\pi \ell X}\psi_z\right\} && \text{for } 1<z \\
b &= \left\{\pi \ell Q_o G(z)\psi(z_o) + \left[-\pi\ell + ib\sin\alpha\cos\alpha\ell/X\right]\psi\right. \\
&\quad \left. + \left[i\cos\alpha + Ri^{1/2}\sin\alpha/X\right]\psi_z\right\}/X && \text{for } 0<z<1 \\
b &= -\left\{\pi\ell(N_s/N_t)^2/X\right\}\psi && \text{for } 1<z \quad .
\end{aligned}
\tag{3.22}
$$

Here X is the Doppler shifted frequency, defined as

$$
X = \begin{cases} \sigma - b\sin\alpha\ell z & \text{for } 0<z<1 \\ \sigma - b\sin\alpha\ell & \text{for } 1<z \end{cases} \quad .
$$

These nondimensional eigenfunctions are related to their dimensional counterparts through

$$
\begin{aligned}
u^* &= HN_t\pi^{-1}u \\
p &= H^2N_t^2\rho_o\pi^{-1}p \\
b &= HN_t^2\pi^{-1}b \quad .
\end{aligned}
\tag{3.23}
$$

Also note that, from (3.4c) and (3.5), v^* and w^* are given by

$$
\begin{aligned}
v^* &= HN_t\pi^{-1}v = HN_t\pi^{-1}(-\psi_z) \\
w^* &= Ri^{-1/2}Hfw = Ri^{-1/2}Hf(i\ell\psi) \quad .
\end{aligned}
\tag{3.24}
$$

We can derive equations for the perturbation kinetic and available potential energy from (3.4). For the model troposphere one can write the energy equations as

$$\frac{dK}{dt} = KBK + PK - WP$$
$$\frac{dP}{dt} = PBP - PK + QB \quad , \tag{3.25}$$

where the kinetic and available potential energy are defined as

$$K^* = \frac{1}{2}(\overline{u'^2} + \overline{v'^2})^* \quad ; \quad P^* = \frac{1}{2}\frac{(\overline{b'^2})^*}{N_t^2} \tag{3.26}$$

and the conversion terms are given by

$$KBK^* = -U_z\cos\alpha(\overline{u'w'})^* + U_z\sin\alpha(\overline{v'w'})^*$$
$$PK^* = (\overline{w'b'})^*$$
$$WP^* = \frac{1}{\rho_0}(\overline{w'p'})^*_{z^*} \tag{3.27}$$
$$PBP^* = fU_z\left(\sin\alpha\frac{(\overline{u'b'})^*}{N_t^2} + \cos\alpha\frac{(\overline{v'b'})^*}{N_t^2}\right)$$
$$QB^* = \frac{(\overline{Q'b'})^*}{N_t^2} \quad .$$

An overbar denotes an average over one wavelength, and the stars indicate dimensional variables. Term KBK is the conversion of mean to eddy kinetic energy due to vertical momentum fluxes; term PK is the conversion of eddy available potential energy to kinetic energy due to vertical heat fluxes; term WP is the divergence of the vertical flux of wave energy; term PBP is the conversion of mean to eddy available potential energy due to horizontal heat fluxes; and term QB is the generation of eddy available

potential energy by cumulus heating. We can rewrite (3.27) by making use of the nondimensionalizations (3.9),(3.23),(3.24). If we further substitute from (3.5), we can make use of the following formula for the correlation of any two perturbation variables:

$$\overline{(u'v')} = \frac{1}{2}e^{-2\sigma_i t}\,\mathrm{Re}\{uv^c\} \quad ,$$

where the superscript c denotes the complex conjugate of a quantity. Since the factor $0.5\times\exp(-2\sigma_i t)$ appears on both sides of (3.25), we can simply omit it. Now we can rewrite (3.27) as

$$\begin{aligned}
KBK &= Ri^{-1/2}\mathrm{Re}\{-\cos\alpha i\ell\psi u^c - \sin\alpha\psi_z^c i\ell\psi\} \\
PK &= \mathrm{Re}\{i\ell\psi b^c\} \\
WP &= \mathrm{Re}\{i\ell\psi p^c\}_z \\
PBP &= \mathrm{Re}\{\sin\alpha ub^c - \cos\alpha\psi_z b^c\}/\pi \\
QB &= Q_o G(z)\mathrm{Re}\{i\ell\psi(z_o)b^c\} \quad ,
\end{aligned} \tag{3.28}$$

where the nondimensional terms are related to their dimensional counterparts of (3.27) through

$$(KBK,PK,WP,PBP,QB)^* = Ri^{-1/2}H^2N_t^2f\pi^{-1}(KBK,PK,WP,PBP,QB) \quad .$$

Finally, we can average (3.25) in the vertical:

$$\frac{d\tilde{K}}{dt} = \widetilde{KBK} + \widetilde{PK} - \widetilde{WP}$$
$$\frac{d\tilde{P}}{dt} = \widetilde{PBP} - \widetilde{PK} + \widetilde{QB} \quad , \tag{3.29}$$

where the tilde denotes the vertical average defined by

$$\widetilde{(\ )} = \int_0^1 (\ )dz \quad . \tag{3.30}$$

The term $\widetilde{WP}$ simplifies to

$$\widetilde{WP} = (\overline{w'p'})_{z=1} = Re\{i\ell\psi p^c\}_{z=1} \quad . \tag{3.31}$$

It is simply the flux of wave energy from the troposphere to the stratosphere.

Since this is a linear problem, the eigenfunctions can be multiplied by any constant and still be a solution, so that their absolute magnitude is arbitrary; their relative magnitude is not, however. In the calculations of the eigenfunctions and the energy budget, the magnitude of ψ was chosen and resulting magnitudes of u,p,b were determined from (3.20) - (3.22). The magnitude of ψ was chosen such that the total perturbation energy was equal to 1:

$$\frac{d}{dt}(\tilde{K} + \tilde{P}) = 1.$$

Quantitative comparisons between the energy budgets and eigenfunctions of different calculations and a reference calculation are possible after the energy conversion terms are renormalized by multiplying them with the ratio of actual to reference growth rate, and the eigenfunctions are multiplied by the square root of that number. This renormalization is equivalent to expressing the energy terms as a fraction of the total energy tendency of the reference calculation, rather than the actual calculation, assuming both perturbations have the same total perturbation energy.

4. Results

Growth rates and phase speeds have been computed for different cumulus heating profiles, and various model parameter values. In the first section of this chapter results for a particular set of parameters, and for four different heating profiles, are discussed. These results will be used as a reference for the subsequent sections, which contain the sensitivity tests with respect to the heating amplitude, the stratospheric static stability, and the bulk Richardson number. The fourth section contains an evaluation of the effects of low-level evaporational cooling in convective downdrafts. The results are summarized in the final section of this chapter.

4.1 Reference run

As a basis for comparison with sensitivity test, the following set of parameters was chosen as a reference run:

$$z_o=0.1$$

$$E=90\%$$

$$Ri=10$$

$$N_s/N_t=3.$$

Although the precipitation efficiency E seems unrealistically large, implying extremely efficient production of precipitation and/or high values of low level water vapor mixing ratio, the resulting heating amplitudes correspond to more realistic precipitation efficiencies if the effects of evaporative cooling in downdrafts are taken into account (see section 4.5). For a tropospheric Brunt-Väisälä frequency of 10^{-2} s^{-1}, the

value of the Richardson number Ri corresponds to a basic state shear of 3.2×10^{-3} s^{-1}, or 32 m/s over a depth of 10 km. Four different heating profiles are used, with levels of maximum heating z_m at 0.5, 0.6, 0.7, and 0.8 (see Fig. 3.3). Growth rates and phase speeds were computed for a set of preselected orientation angles. A summary of these results is shown in Fig. 4.1, which shows the growth rate plotted on a polar diagram of total wavenumber and orientation angle. In the case of multiple solutions, the largest growth rate is plotted. Recall from chapter 3 that an orientation angle of 0° coresponds to a symmetric mode, and one of +90°,-90° to a baroclinic mode. In terms of an unrotated coordinate system (x^*, y^*) with its x^*-axis aligned with the shear vector, the wavenumber in y^* ($\lambda=\ell\cos\alpha$) is plotted along the x-axis of Fig. 4.1, and the wavenumber in x^* ($k=-\ell\sin\alpha$) along the negative y-axis. Two separate modes are present in Fig. 4.1. The Eady mode, with maximum growth at small wavenumbers along the baroclinic axis, propagates in the direction of the wind shear. It thus has positive phase speeds (not shown in Fig. 4.1) for positive angles α, and negative c for negative α. The second mode, with maximum growth rates at larger wavenumbers near the symmetric axis, is the continuation to general orientation angles of the symmetric wave-CISK modes described by Emanuel (1982). In the following, this mode will be referred to loosely as the symmetric, or wave-CISK mode. Its phase speed is positive, implying propagation toward the warm air. For heating profiles with z_m below 0.8, a third mode exists at large positive orientation angles, for small wavenumbers. It is the continuation of the wave-CISK mode through $\alpha=-90°$. Its phase speed is negative, implying propagation against the shear vector and toward the cold air. Its growth rate is small, in most cases smaller than that of

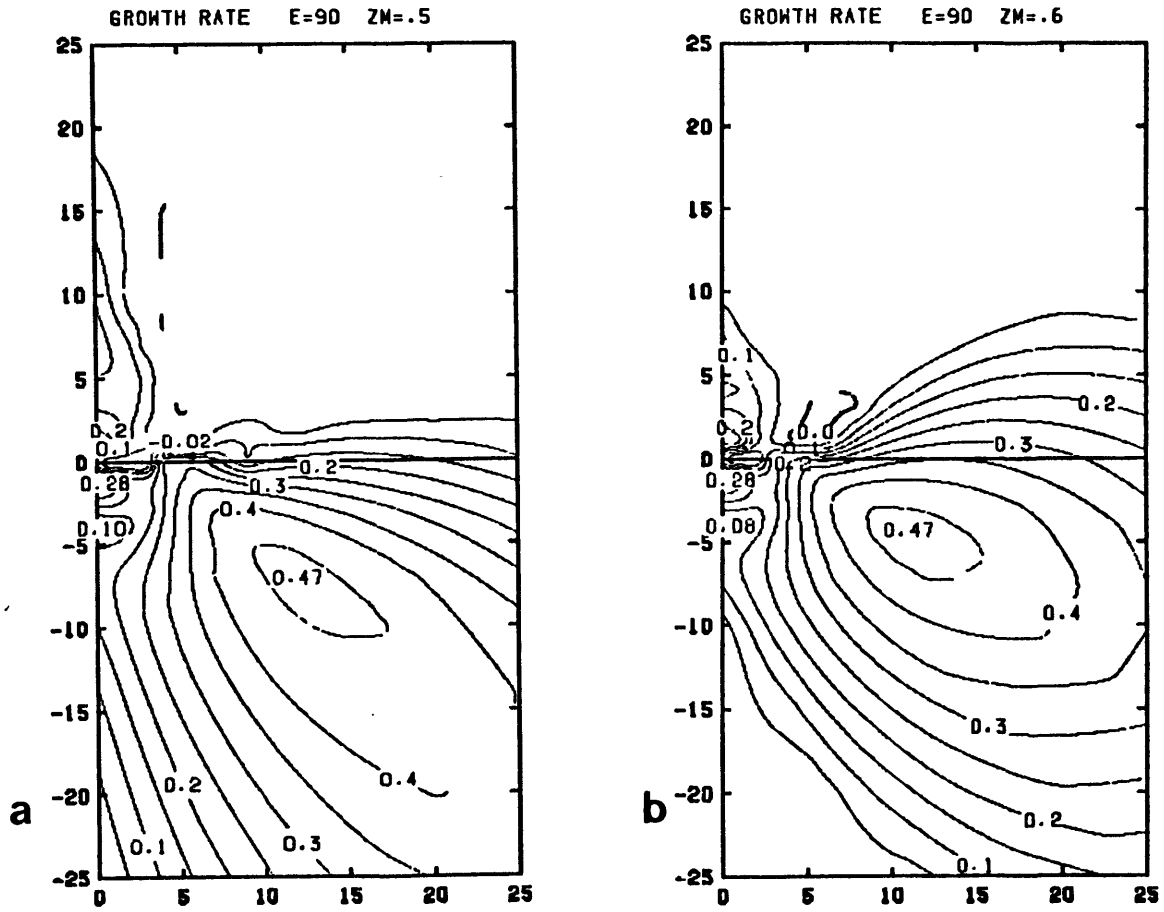

Fig. 4.1: Contour plot of growth rate for the reference run, on a polar diagram of total wavenumber (increasing radially outward from the midpoint of the y-axis) and orientation angle α (measured counterclockwise from the x-axis). The x-axis is drawn in the middle of the plot, but the labels of ℓcosα are given at the bottom. The y-axis is labeled with values of ℓsinα. a): for z_m=0.5, b): for z_m=0.6, c) for z_m=0.7, d): for z_m=0.8.

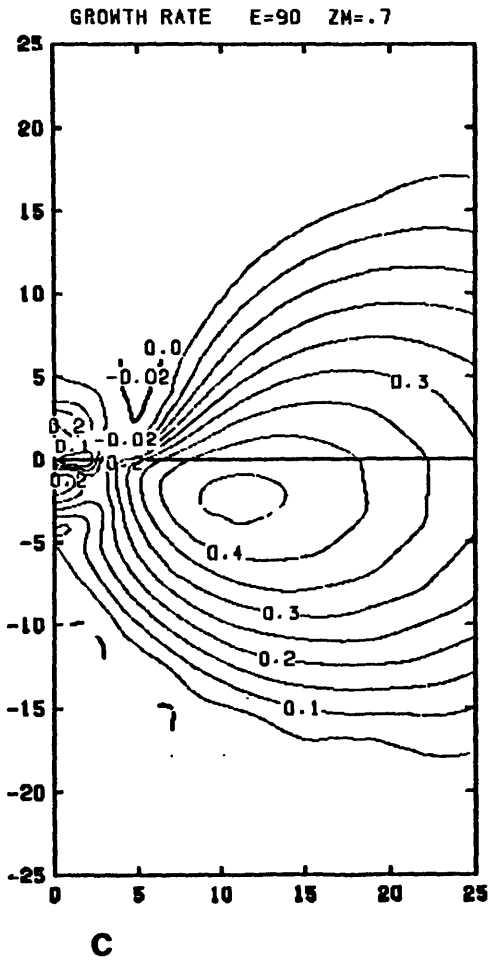

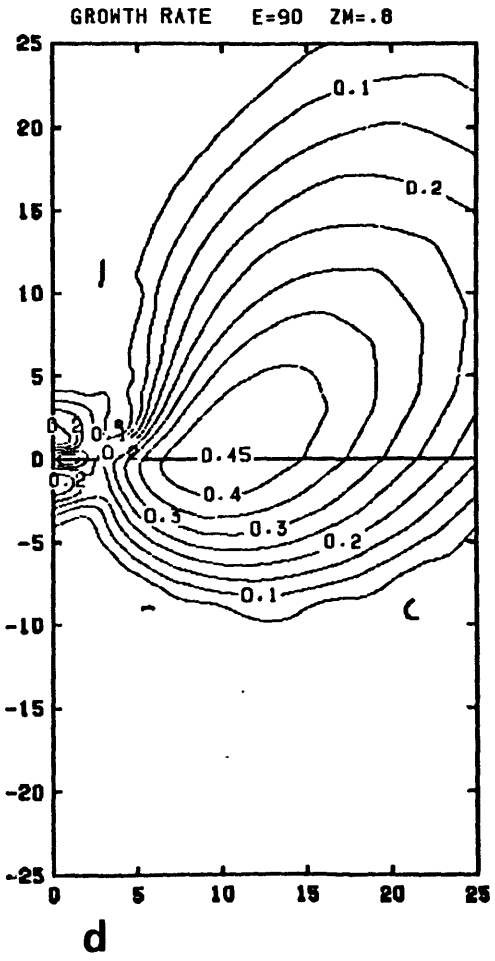

Fig. 4.1 (continued).

the Eady mode and the wave-CISK mode at corresponding values of wavenumber and orientation angle. This mode is therefore not of great interest and will not be discussed any further. A more detailed discussion of the Eady mode and the wave-CISK mode follows.

4.1.1 Eady mode

a) Growth rates and phase speeds

Growing modes exist in the Eady model in the absence of cumulus heating. For Ri<1, the flow is symmetrically unstable and the fastest growing disturbances are oriented parallel to the shear (along the symmetric axis), with growth rates monotonically increasing with wavenumber. Baroclinic instability modes exist at all Ri, with maximum growth rates at a finite wavenumber along the baroclinic axis. For the case of a rigid lid upper boundary condition, the baroclinic instability modes were calculated asymptotically, for Ri >> 1, by Eady (1949). Stone (1966,1970) extended these results to smaller Richardson numbers. This calculation was repeated with the present model by setting the heating amplitude equal to zero, and imposing a rigid lid upper boundary. The result for $\alpha=90°$, shown as the dashed line in Fig. 4.2, is in good agreement with quasi-geostrophic theory and the approximate solution derived by Stone (1966). The phase speed is constant and equal to the mean basic flow.

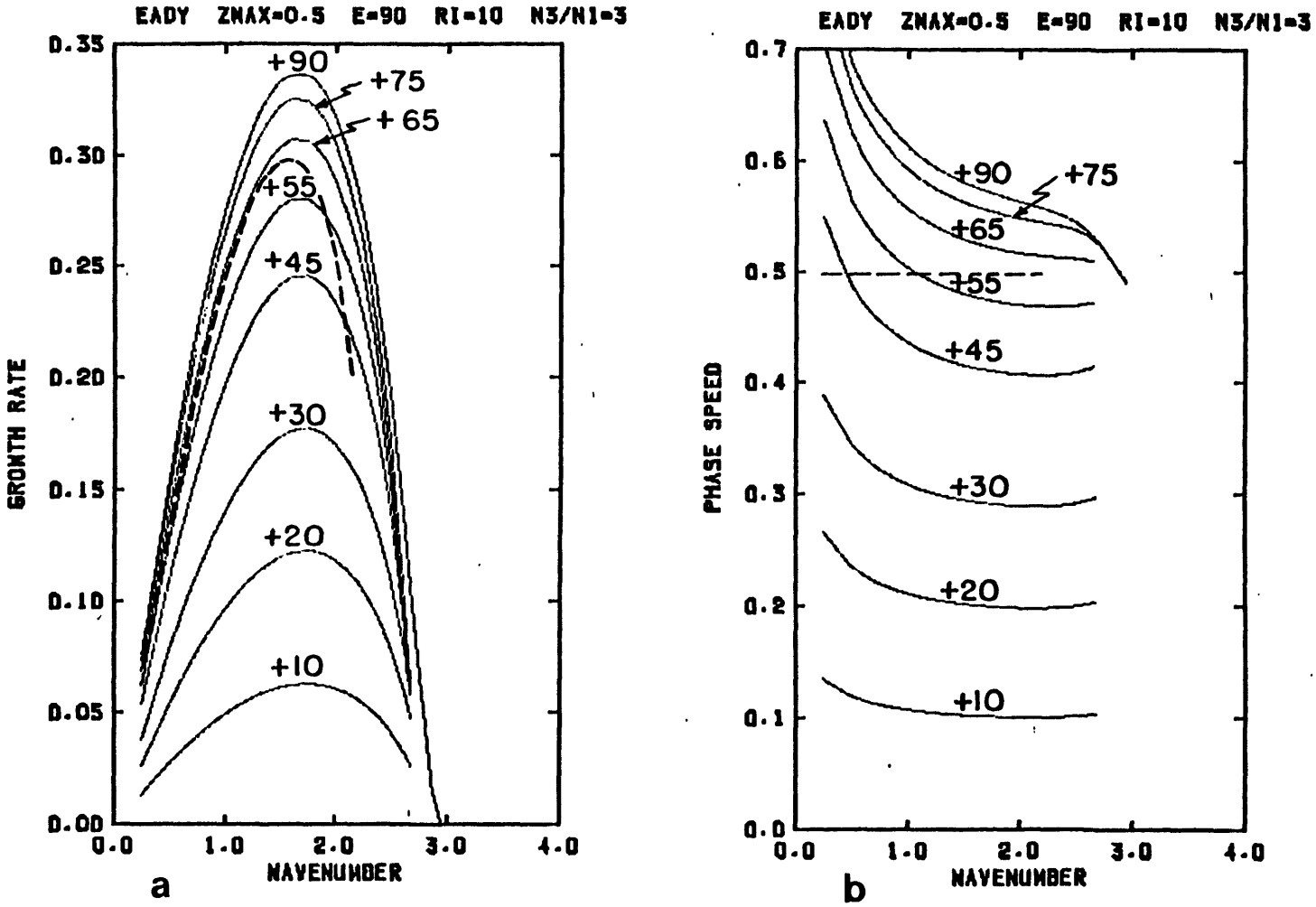

Fig. 4.2: Results for the Eady mode (reference run), with z_m=0.5. The adiabatic, rigid lid result for α=90° is shown dashed. Growth rate (a,c) and phase speed (b,d) are shown as a function of the total wavenumber. Curves are labeled with the value of the orientation angle (in °). a) and b) are for positive, c) and d) are for negative orientation angles.

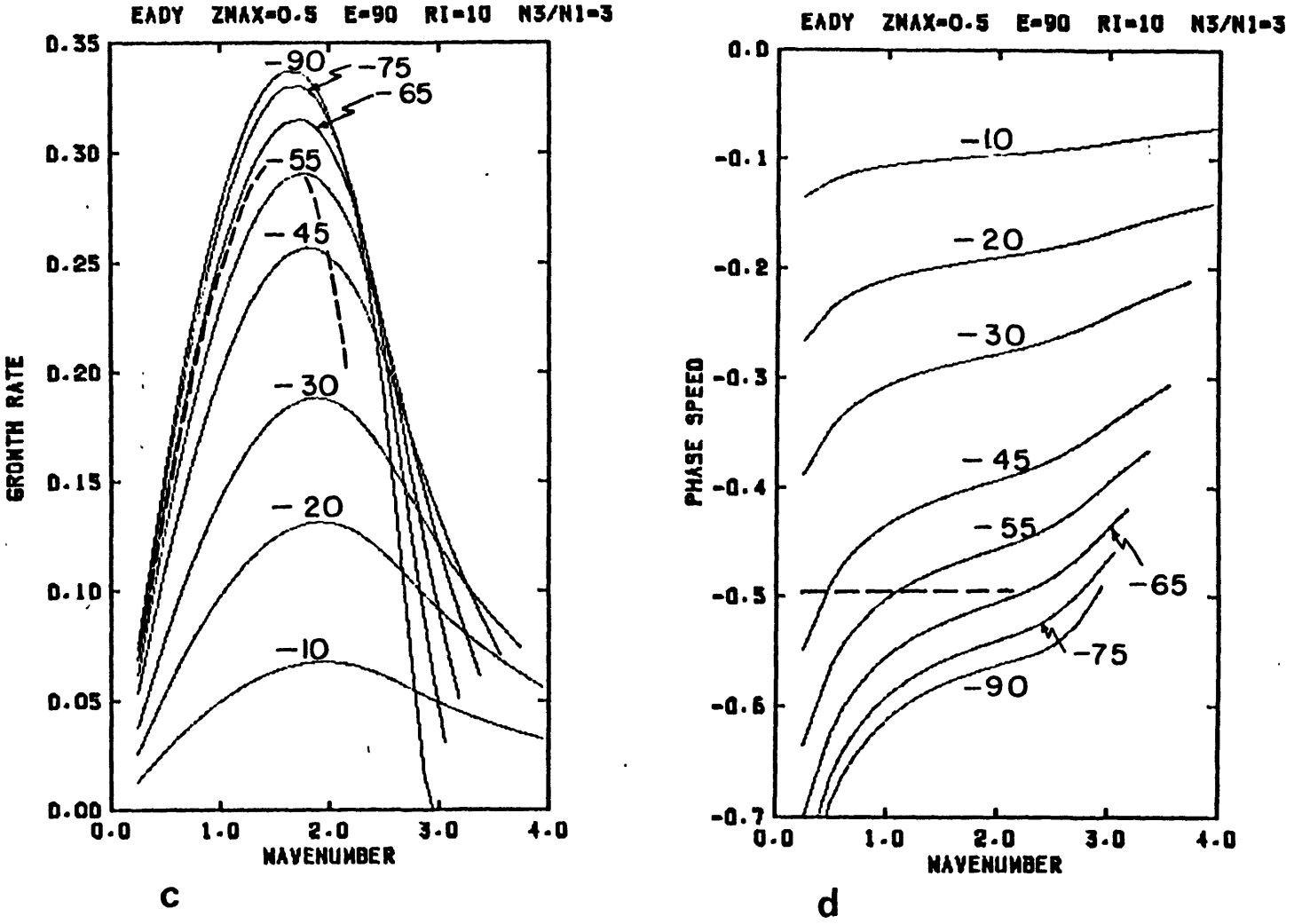

Fig. 4.2 (continued).

Also shown in Fig. 4.2 are the results for nonzero cumulus heating and a radiation upper boundary condition, for a heating profile with z_m=0.5. Curves are shown for different orientation angles. Note that the phase speed is in the direction of the wind shear (c>0 for α>0, c<0 for α<0), and directed toward the warm air for α>0, and toward the cold air for α<0. The growth rate value and the wavenumber of maximum growth of the heated mode at α=+90°,-90° are approximately 15% larger than those of the adiabatic mode. Computations with heating and a rigid lid, and no heating with a radiation boundary condition [1] (not shown here) show that this increase is due to the heating alone, while the radiation boundary condition leads to a slight compensation of this effect. Phase speeds were increased by the increased heating, but only for large wavenumbers; the radiation boundary condition is responsible for the increase in phase speed at lower wavenumbers.

This result may be compared to calculations by Mak (1982) for quasi-geostrophic disturbances aligned with the baroclinic axis in an Eady model. He used a rigid lid upper boundary condition, and related the heating to the dynamically forced part of the large scale vertical velocity. For a comparable heating amplitude, the wavenumber and growth rate of the most unstable mode were increased by approximately 20%; the phase speed was virtually unchanged. This is in good agreement with the rigid lid calculations with the present model.

---

1) The Charney-Stern criterion for quasi-geostrophic baroclinic instability is satisfied in the case of a radiation boundary condition because the discontinuity in the wind shear (and static stability) at the tropopause imply a positive potential vorticity gradient there.

The growth rate curves for different orientation angles show that the largest growth rates of the Eady modes are along the baroclinic axis, in accordance with the quasi-geostrophic results for adiabatic disturbances. The growth rates at orientation angles away from the baroclinic axis are slightly larger at negative α than at the corresponding positive α. This difference is largest for large wavenumbers and small orientation angles. Phase speeds decrease with decreasing values of α, reflecting the smaller across-line component of the mean flow. At all angles, the steering level is in the upper half of the model troposphere, and the +f and -f levels are absent. The Doppler-shift throughout the domain is less than 2f for wavenumbers below the cutoff wavenumber predicted by quasi-geostrophic theory for Ri>1.3, thus precluding any $\mp$f singularities for the Eady mode for Ri>1.3. For smaller Ri this still holds, because the actual cutoff wavenumber is smaller than that predicted by quasi-geostrophic theory or by Stone's asymptotic result. At wavenumbers above the wavenumber of fastest growth, the phase speed increases in magnitude for positive α below 55°, while it continually decreases for negative α.

The effect of the heating is quite similar for the different heating profiles. Fig. 4.3 through Fig. 4.5 show the growth rate and phase speed curves for z_m=0.6, 0.7, and 0.8. The growth rate and the wavenumber of the fastest growing mode decrease slightly as the level of maximum heating is raised. At larger wavenumbers, the growth rates are increased for larger z_m at positive α, while at negative α they are largest for intermediate z_m. Phase speeds at large wavenumbers consistently increase in magnitude as z_m is increased. As a result, at z_m=0.8 the phase speeds for negative α are alomost a mirror image of the phase speeds for positive α. Most of these differences between the different heating

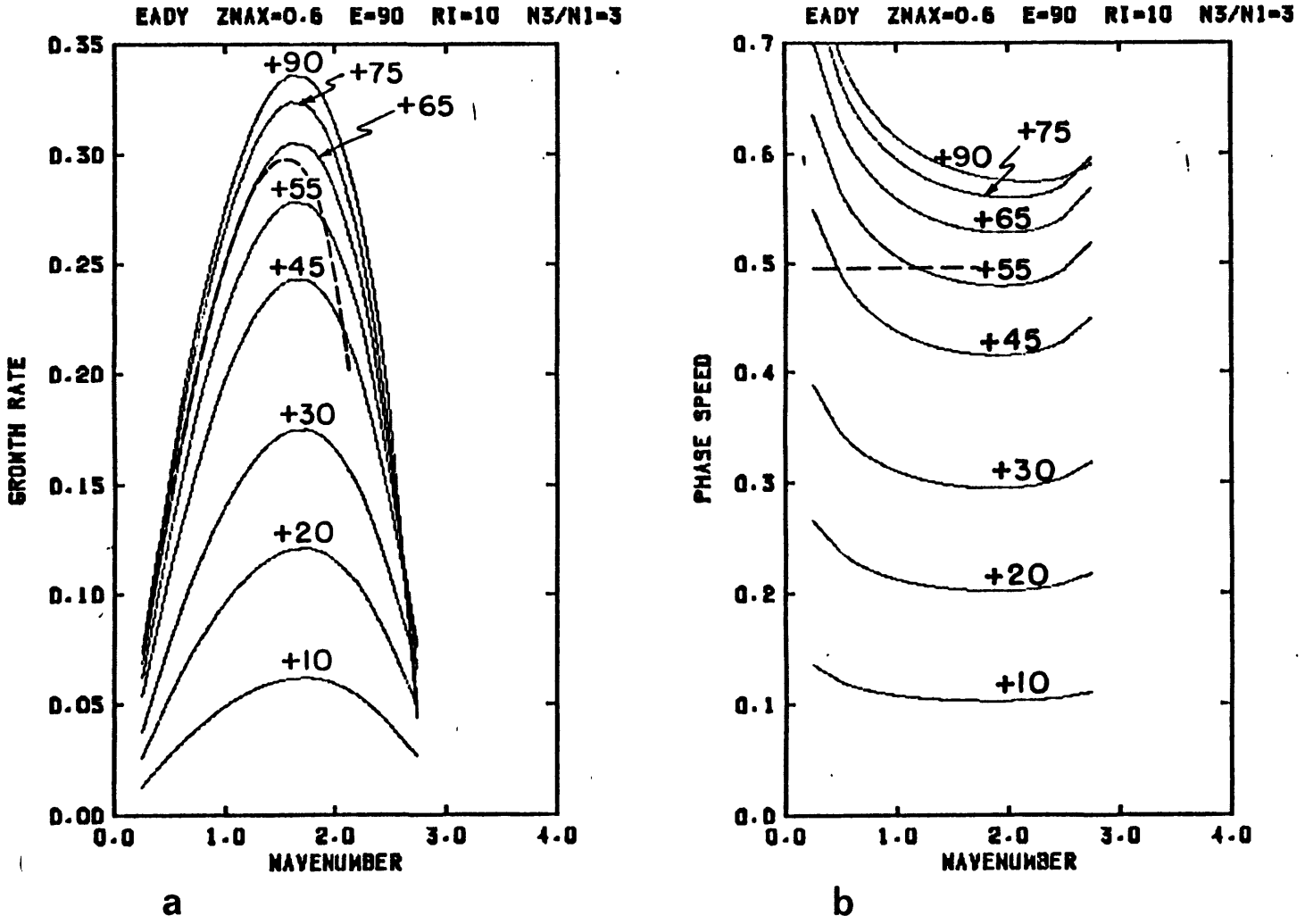

Fig. 4.3: As Fig. 4.2, but for z_m=0.6.

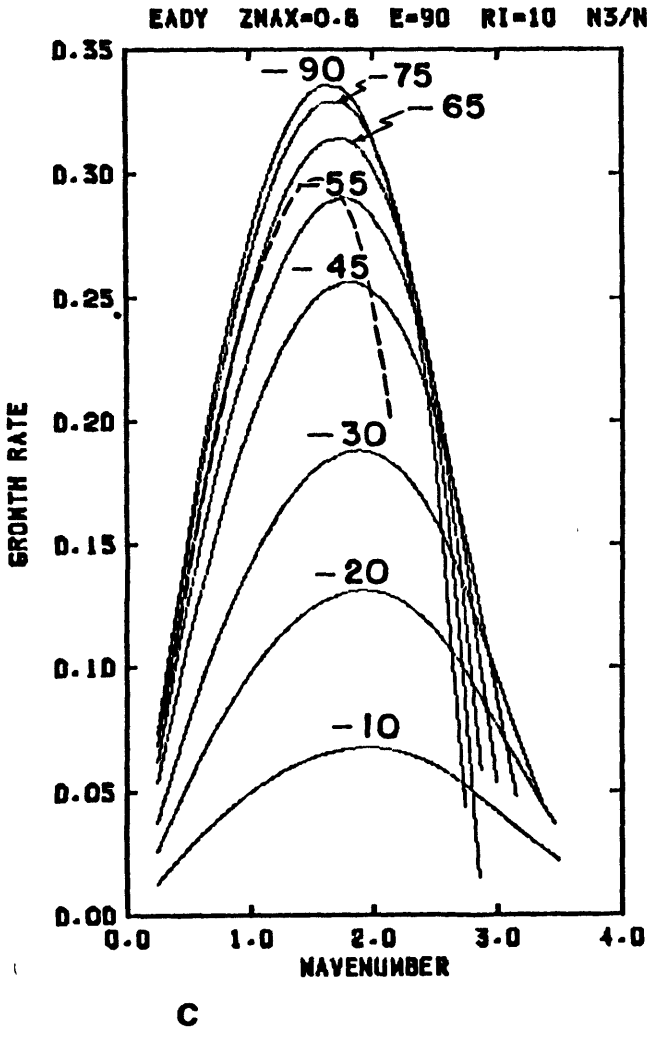

c

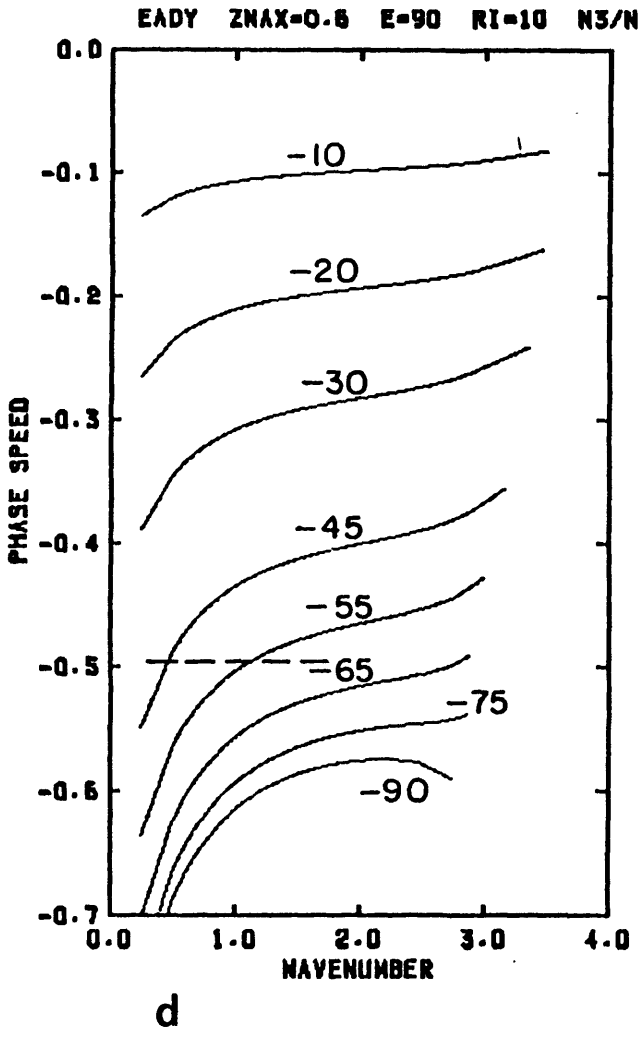

d

Fig. 4.3 (continued).

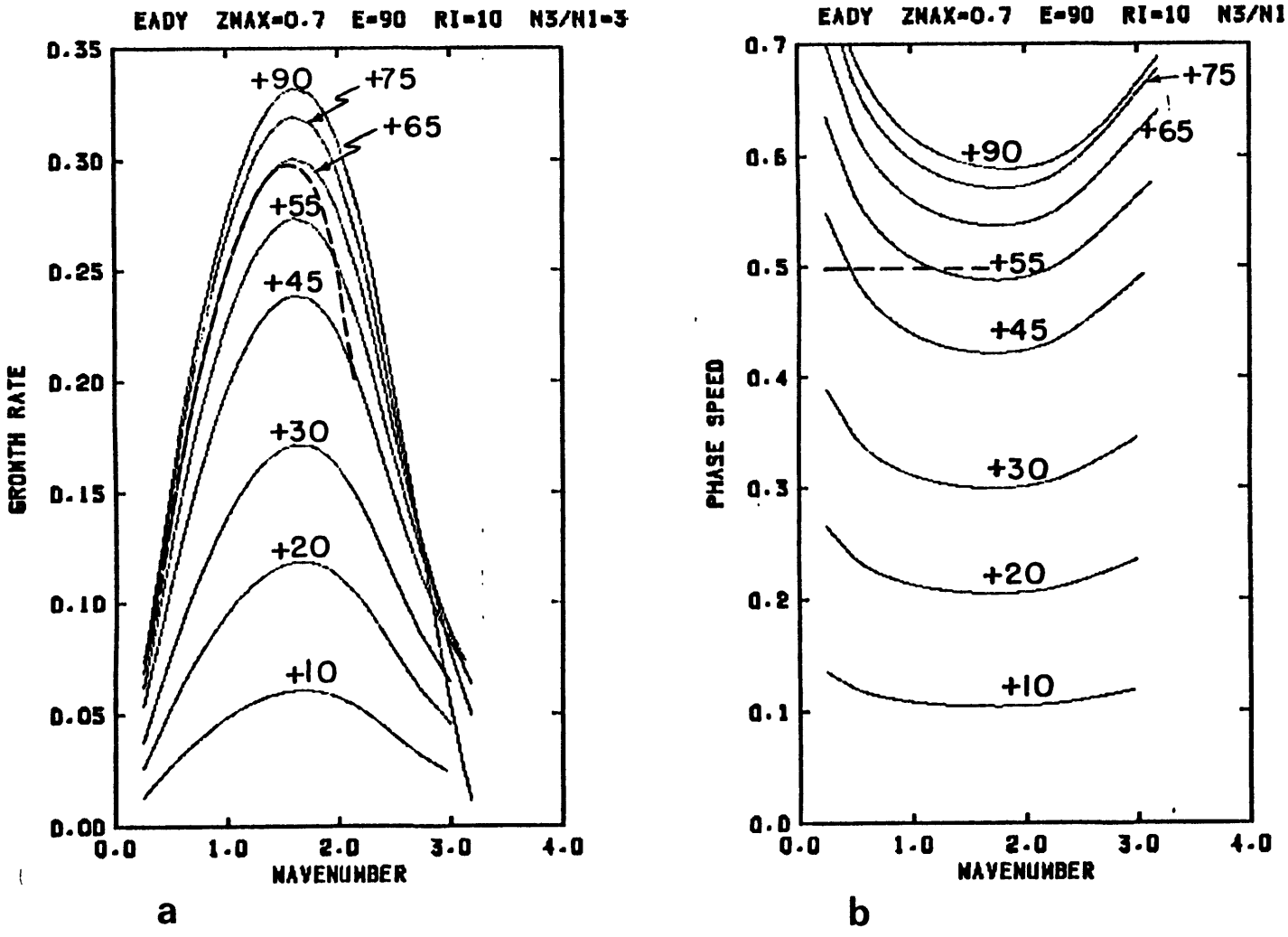

Fig. 4.4: As Fig. 4.2, but for z_m=0.7.

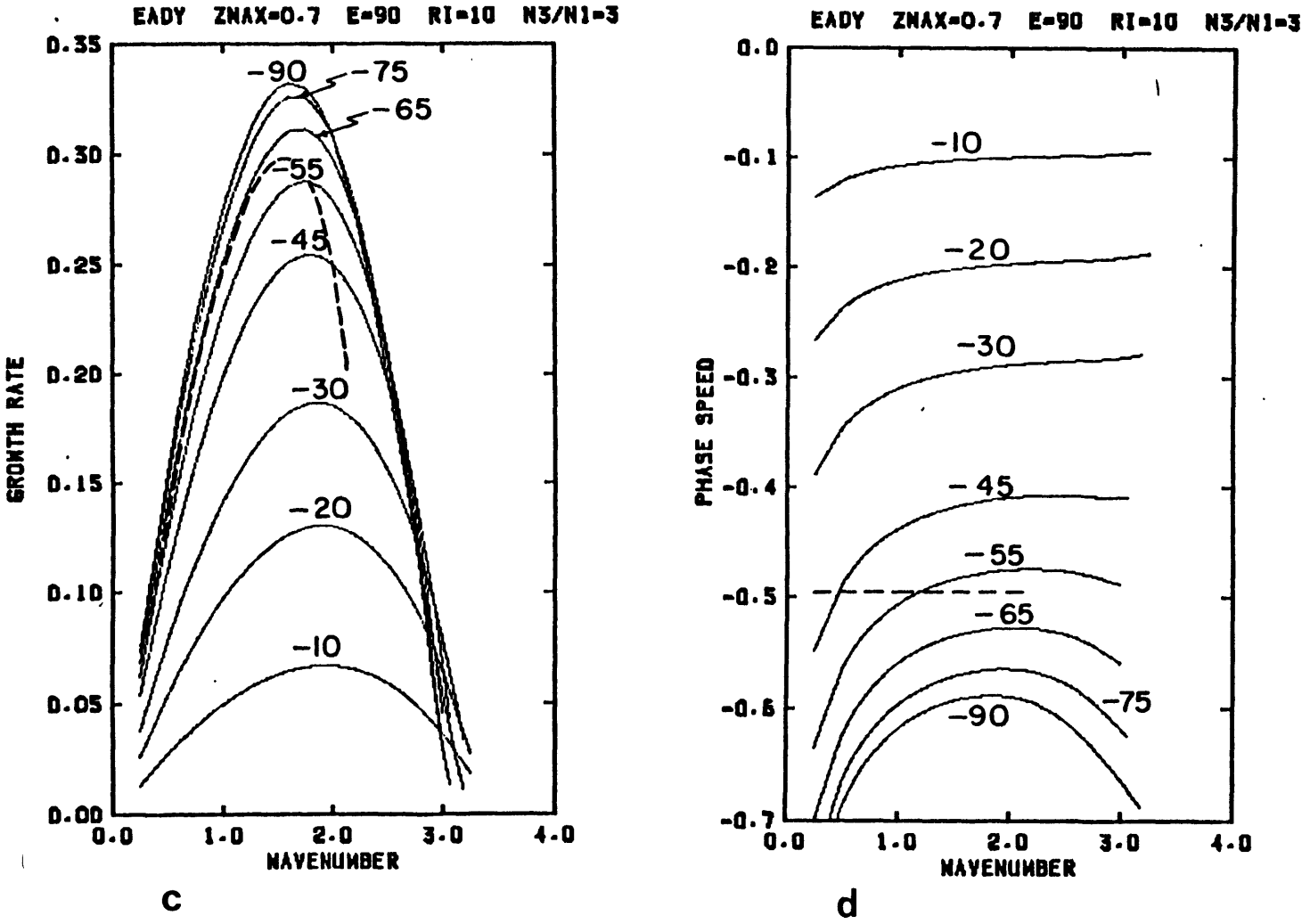

Fig. 4.4 (continued).

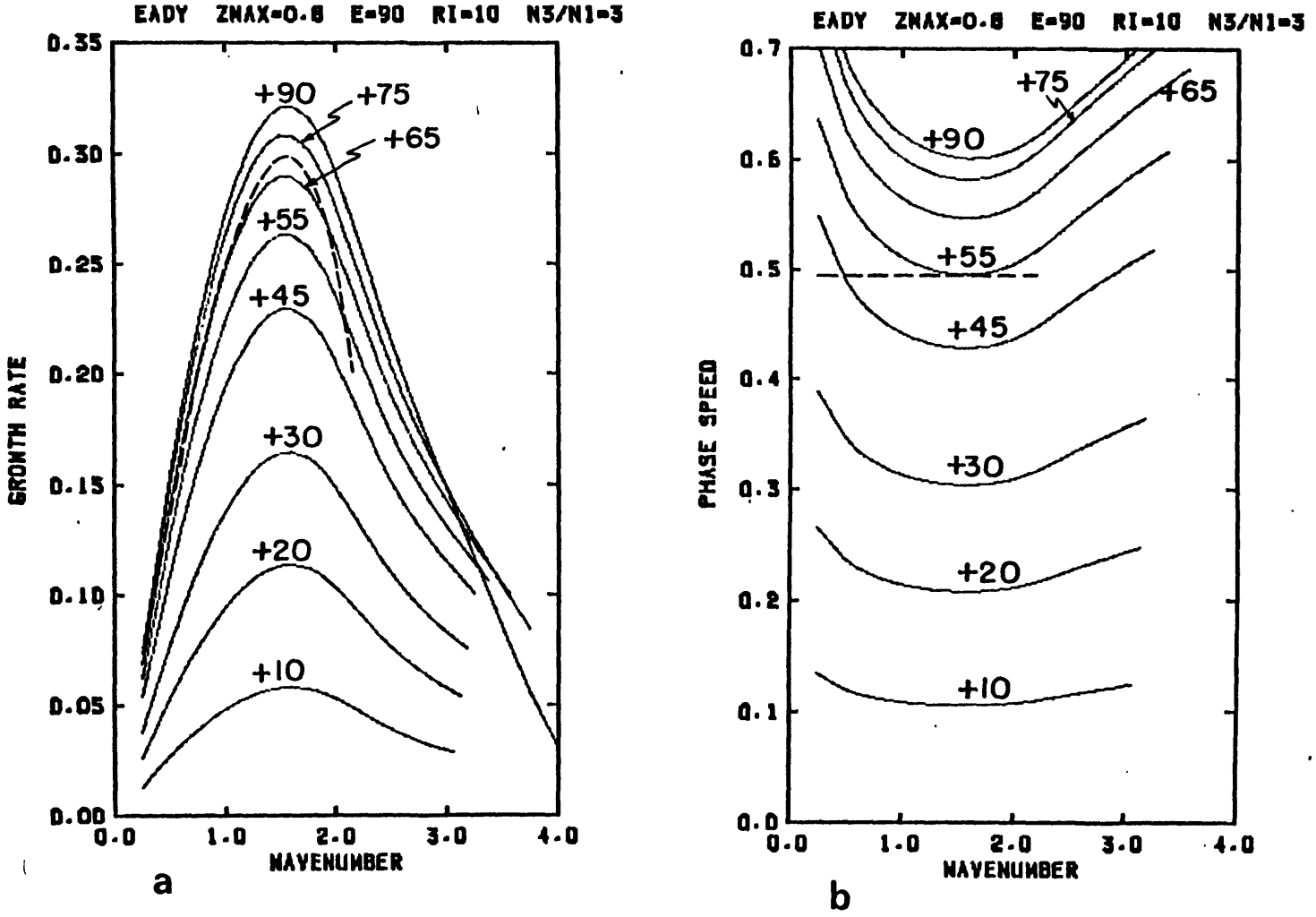

Fig. 4.5: As Fig. 4.2, but for z_m=0.8.

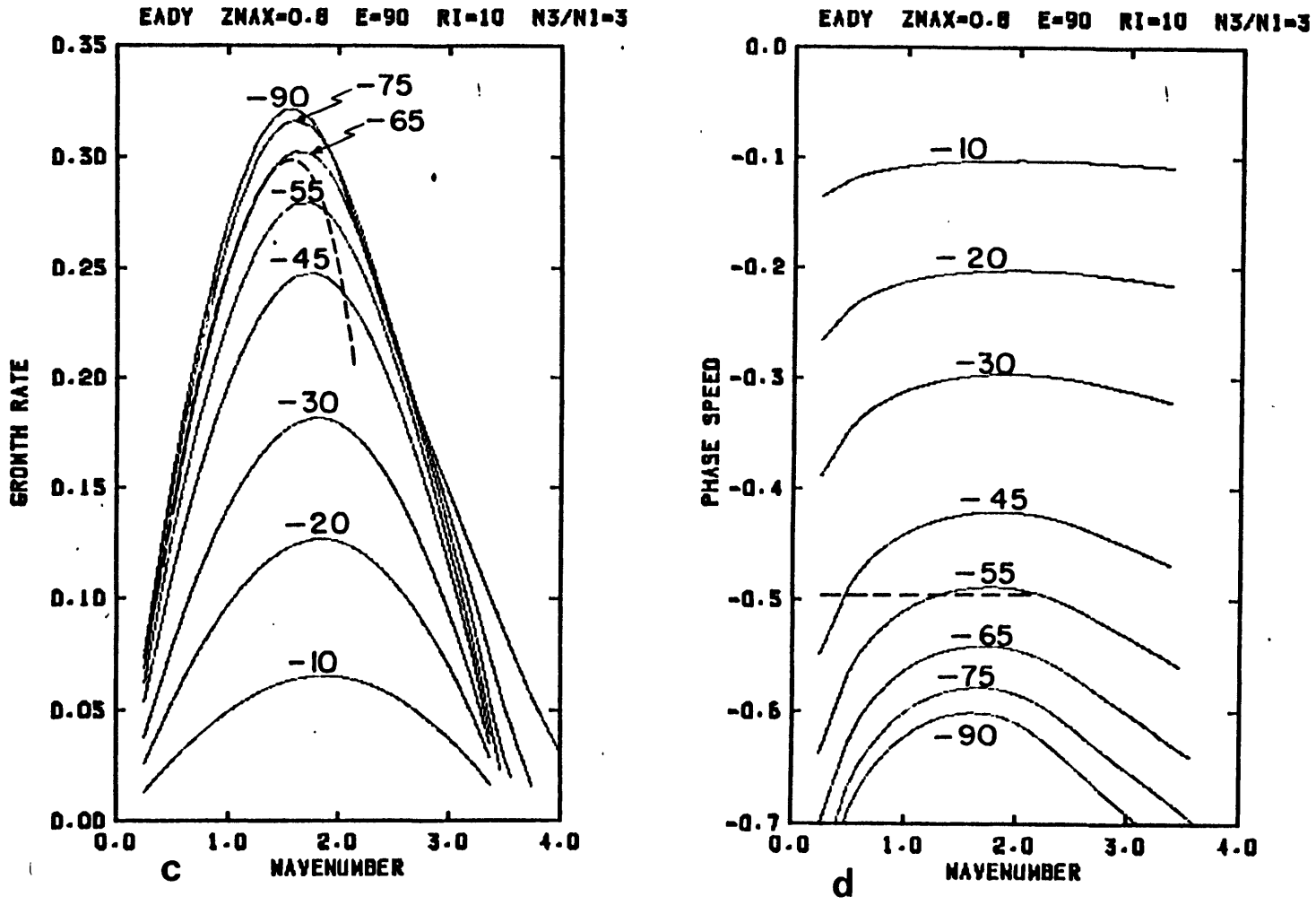

Fig. 4.5 (continued).

profiles become noticeable only for wavenumbers above the wavenumber of maximum growth, and thus do not appreciably alter the qualitative effects of cumulus heating on the Eady mode.

The wavenumber and the growth rate values for the fastest growing mode may be related to dimensional values of the wavelength and e-folding time by equation (3.9). For typical values of H=10km, $N_t=10^{-2}$ s^{-1}, $f=10^{-4}$ s^{-1}, the wavelength L and the e-folding time T for the Eady mode at $\alpha=90°$, E=90%, and $z_m=0.5$ are given by

L=3600 km

T=26 hours.

b) Vertical structure and energetics

The vertical structure of the Eady mode at $\alpha=90°$ is shown in Fig.4.6,for the case of zero heating and a rigid lid upper boundary condition. All quantities plotted are normalized by the maximum amplitude in the domain, which is given in the lower left hand corner of each panel. The amplitudes of the eigenfunctions are chosen such that the time rate of change of the total perturbation energy is unity. The steering level is indicated by the symbol 0 in the energy budget graph of Fig. 4.6. The wave is moving to the left in the diagram. The cross-line streamfunction slopes back with height, i.e. upshear, and the perturbation buoyancy slopes downshear, as predicted by quasi-geostrophic theory. The energy budget shows a nearly constant conversion of mean to eddy available potential energy (PBP) as virtually the only source of energy, again in agreement with quasi-geostrophic theory.

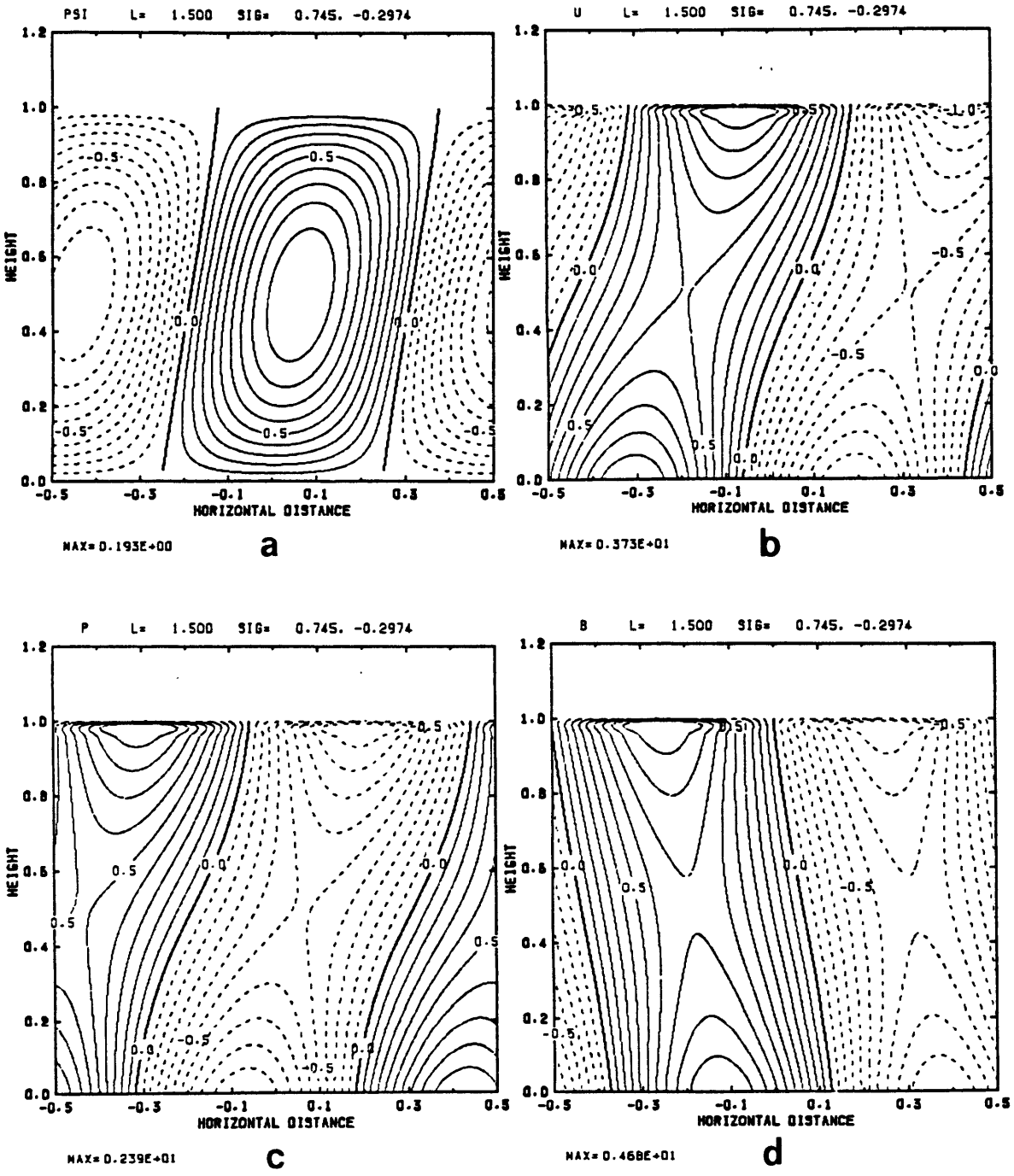

Fig. 4.6: Vertical structure and energetics for the adiabatic Eady mode without heating, for the case of a rigid lid boundary condition, at ℓ=1.5 and α=90°. Contour plots of the nondimensional ψ'(a), u'(b), p'(c), and b'(d), normalized by their maximum value in the domain (given at the bottom of each panel). e): energy conversion terms as a function of height, normalized by the maximum value. f): vertically integrated energy budget.

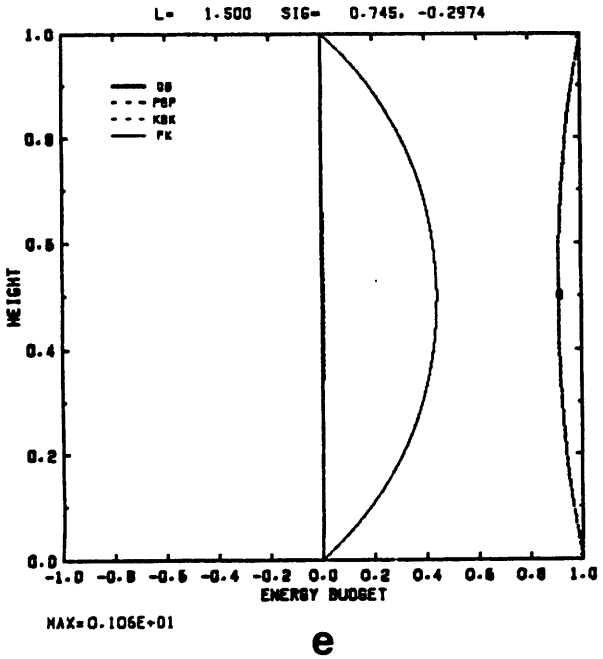

e

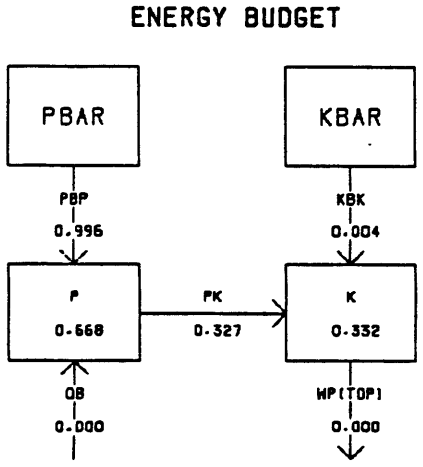

f

Fig. 4.6 (continued).

Fig.4.7 shows the vertical structure of the heated Eady mode at $\alpha=90°$, for the case of a sinusoidal heating profile ($z_m=0.5$) and a radiation boundary condition. Again, the wave is moving to the left in the diagram. Compared to the adiabatic mode the steering level is higher in the domain, and the slope of the perturbation streamlines is smaller. As was mentioned in the previous section, the larger phase speeds (higher steering levels) at this wavenumber is a result of the radiation boundary condition. The relative amplitudes of perturbation along-line velocity, pressure and buoyancy are all smaller in the upper troposphere. Most noticeable, however, is the decreased slope of the perturbation buoyancy and the nearly constant amplitude in the troposphere. This different thermal structure is also reflected in the energetics of the disturbance.

For the discussion of the energy budget it is more convenient to look at the pressure, rather than buoyancy, distribution. Since the adiabatic result agrees closely with quasi-geostrophic theory, it may be useful to consider the geostrophic part of the conversion term PBP, which is given by

$$PBP_g = \sin\alpha(\overline{u_g' b'})/\pi = -Ri^{-1/2}\sin\alpha(\overline{\frac{\partial p'}{\partial y}\frac{\partial p'}{\partial z}}) \quad ,$$

where the subscript g denotes geostrophic components. If we substitute the normal mode solutions for p' into the above formula, and express the complex p-amplitude as

$$p(z) = \left|p(z)\right| e^{i\gamma(z)} \quad ,$$

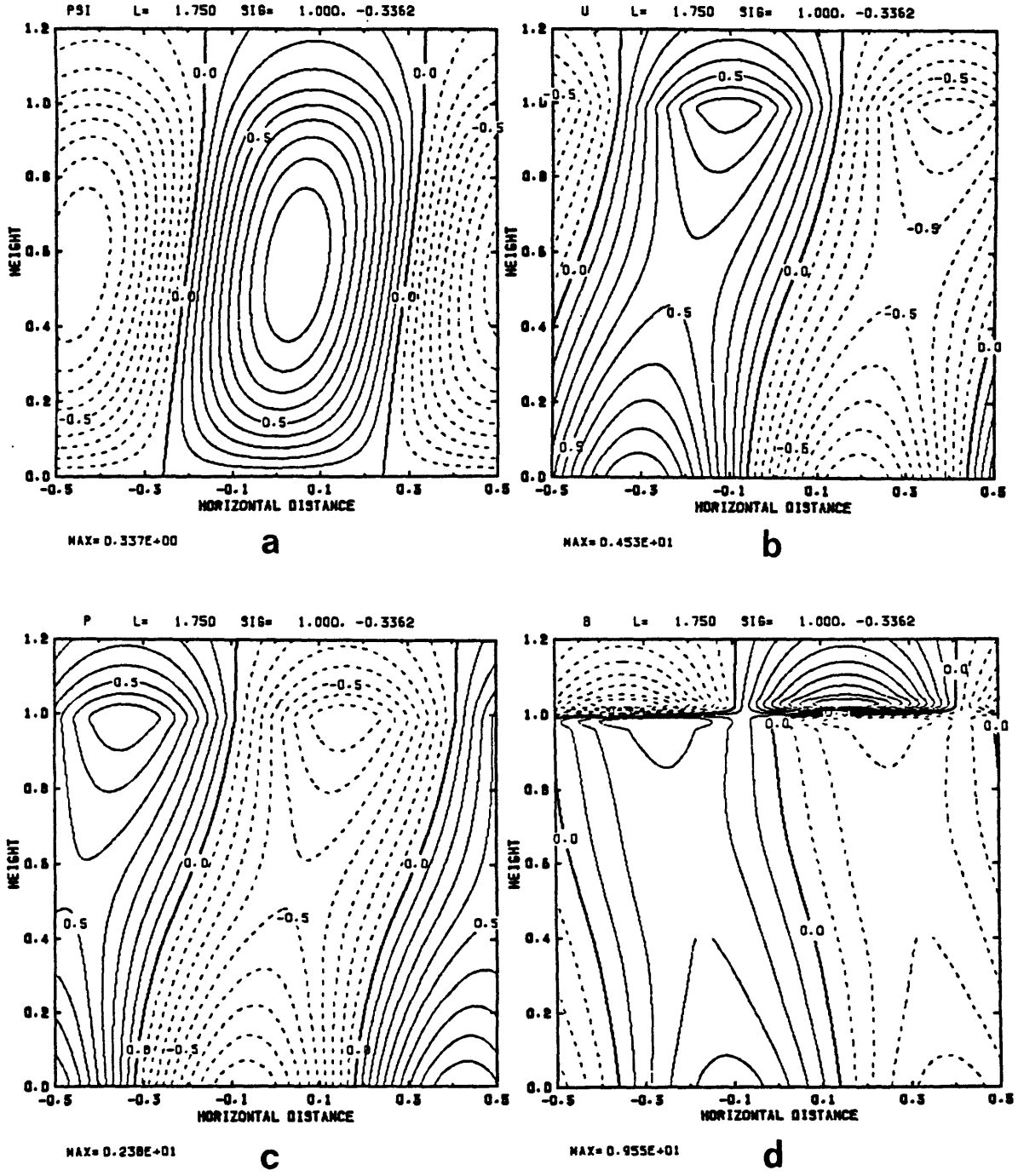

Fig. 4.7: As Fig. 4.6, but for the reference run Eady mode with z_m=0.5, at ℓ=1.75 and α=90°.

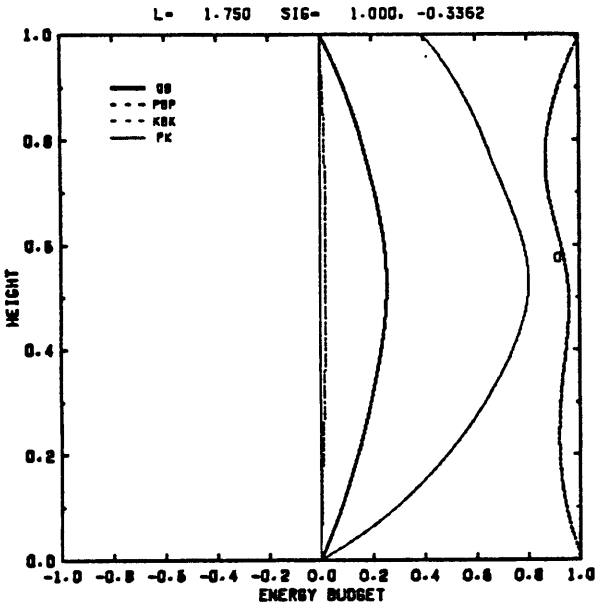

e

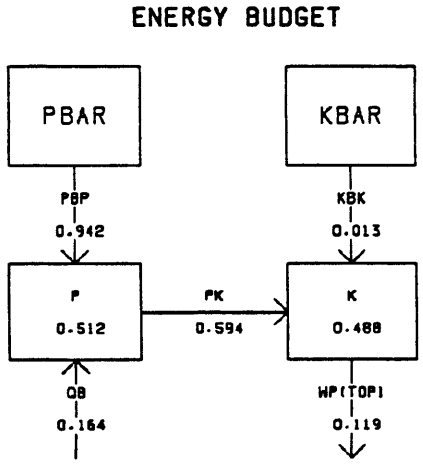

f

Fig. 4.7 (continued).

then we can write

$$PBP_g = -\frac{1}{2}Ri^{-1/2}\sin\alpha\left|p(z)\right|^2 \frac{d\gamma}{dz} e^{-2\sigma_i t} \quad .$$

This just exemplifies the well-known role of the upshear slope of the perturbation pressure field in the baroclinic instability mechanism. For a direct comparison between the adiabatic and the heated Eady mode, the amplitude of the adiabatic Eady mode is renormalized so that its total perturbation energy is equal to that of the heated Eady mode. This is accomplished by multiplying the energy conversion terms by the ratio of the growth rates, and the eigenfunction amplitudes by the square root of that number. This renormalization shows an increase in the amplitude of the perturbation pressure, which, together with the increase of the wavenumber of maximum growth, leads to a 7% increase in PBP for the heated Eady mode,despite the decreased slope of the perturbation streamlines.

Most of the increase in the growth rate is accounted for by the generation of eddy available potential energy (QB), although it only constitutes 16% of the total energy budget. This result may be compared qualitatively with calculations by Mak (1982). He computed the energy budget for an Eady mode, using a heating amplitude almost four times as large as the one used here. He found that the heating generation of eddy available potential energy exceeded the baroclinic conversion, which was nevertheless a nonnegligible contribution. Since at his wavelength of maximum growth an adiabatic disturbance would have been stable, the cumulus heating destabilized the perturbation both directly (QB) and indirectly (PBP). Both these destabilizing effects of heating are found in this model, too, although with a much smaller magnitude.

The dimensional values of the eigenfunction amplitudes can be obtained from eq.(3.9) and typical values of H=10 km, $N_t=10^{-2}$ s^{-1}, and $f=10^{-4}$ s^{-1}, and a mean potential temperature of 300 K. If we assume a maximum vertical velocity of 1 cm/s in Fig.4.7, the along-line (zonal) velocity perturbation has a magnitude of 7.7 m/s at the surface, and the pressure perturbation has a magnitude of 4.1 mb. The maximum potential temperature perturbation is then 5 K.

The slope of the Eady mode streamlines is, by the very nature of baroclinic instability, shallower than that of the isentropes. The Eady mode thus does not satisfy the restrictions resulting from the basic state density discontinuity at the tropopause (see section 3.2). This results in large amplitude buoyancy perturbations above the tropopause, evident in Fig.4.7, which have to be regarded as at least partially artificial. The small differences between rigid lid and radiation boundary condition calculations suggest, however, that the tropospheric structure and dynamics are not strongly influenced by this. For a disturbance rotated away from the baroclinic axis, the upshear component of the tilt of the pressure field will be decreased for an equal tilt across the disturbance axis. Fig.4.8, which shows the Eady mode at $\alpha=30°$, shows a partial compensation of this effect by a larger tilt across the disturbance axis. Nevertheless, the geostrophic part of PBP is reduced by approximately 20%; nongeostrophic effects lead a further reduction of about the same magnitude. The increased importance of nongeostrophic effects is also evident in the larger magnitude of the conversion of mean to eddy kinetic energy (KBK), which is negative at $\alpha=30°$. The change in KBK, together with a decrease in QB, contribute to a decrease in growth rate, the largest part of which is due to the decrease in PBP.

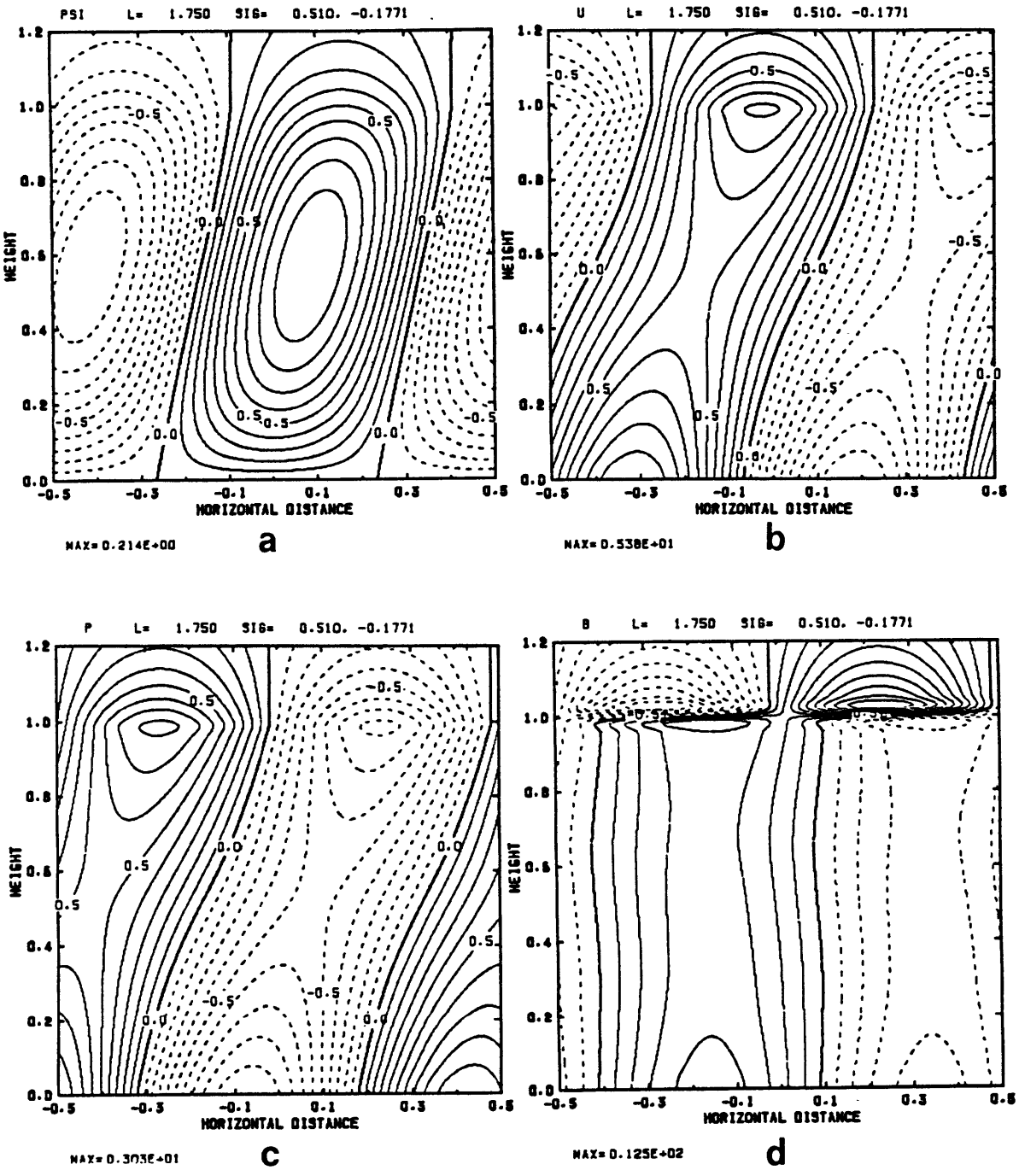

Fig. 4.8: As Fig. 4.6, but for the reference run Eady mode with z_m=0.5, at ℓ=1.75 and α=30°.

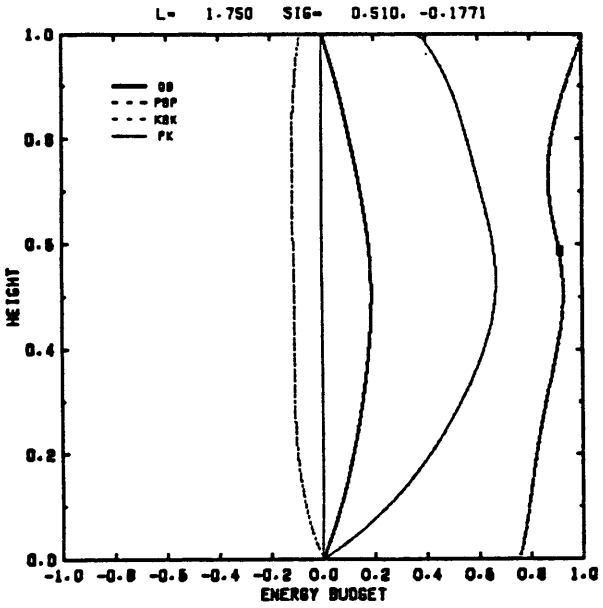

e

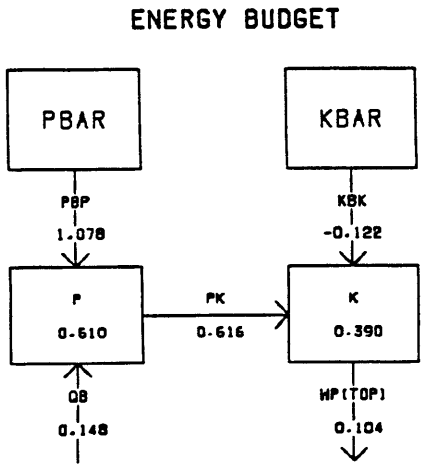

f

Fig. 4.8 (continued).

At α=-30° (see Fig.4.9) the streamline contours show very little tilt, and the pressure lines are also tilted less than for α=+30°. Note that the wave is moving to the right in this diagram. The baroclinic potential energy conversion (PBP) is smaller than for α=+30°, but the disturbance is growing more rapidly, due to a reversal in the sign of the kinetic energy conversion (KBK). The difference in growth rate between α=-30° and α=+30° is small compared to the difference in PBP and KBK, indicating a large amount of cancellation of these two effects.

The sensitivity of the above results to the form of the heating profile may be assessed by comparing Fig.4.7 and Fig.4.10, which show the vertical structure of the heated Eady mode at α=90°, for z_m=0.5 and 0.8, respectively. There is very little difference in any of the eigenfunctions, aside from a slightly higher circulation center and a stronger buoyancy perturbation at upper levels for z_m=0.8. This larger buoyancy perturbation below the tropopause is also reflected in larger values of related energy conversion terms (QB and PBP) at that level. The integrated value of the heating generation QB is increased as a result but this is offset by an overall decrease in PBP and an increased loss of energy through the tropopause (WP). Thus, in spite of a more efficient generation of eddy available potential energy by convective heating in the case of z_m=0.8, secondary changes in the energy budget lead to a 6% decrease in the growth rate compared to the sinusoidal heating profile. The growth rate is still larger than that of the adiabatic mode, however.

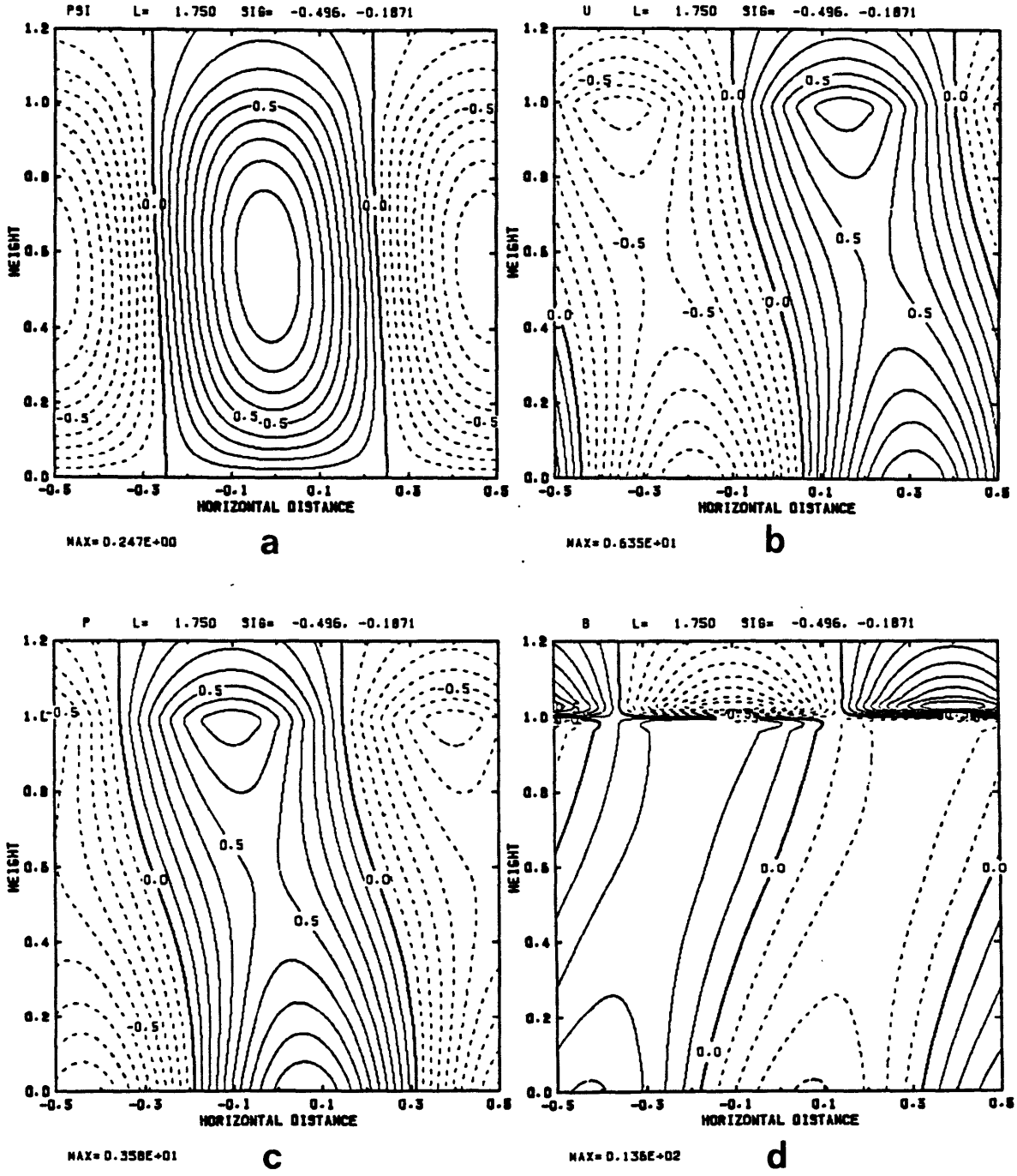

Fig. 4.9: As Fig. 4.6, but for the reference run Eady mode with z_m=0.5, at ℓ=1.75 and α=-30°.

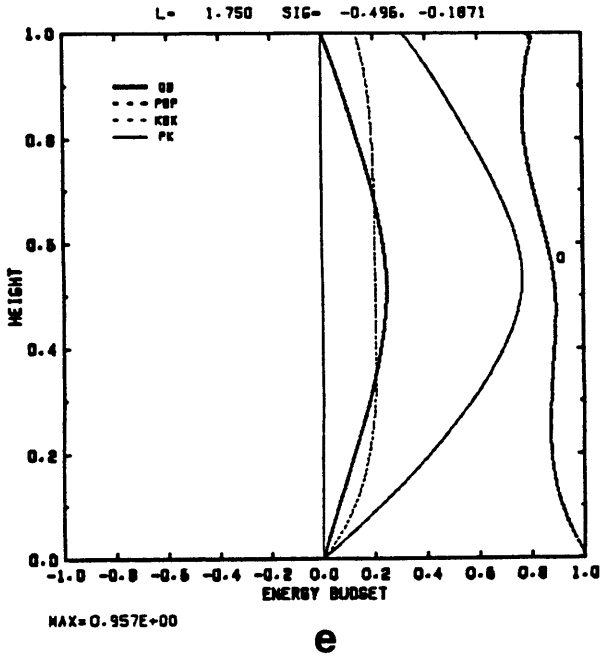

e

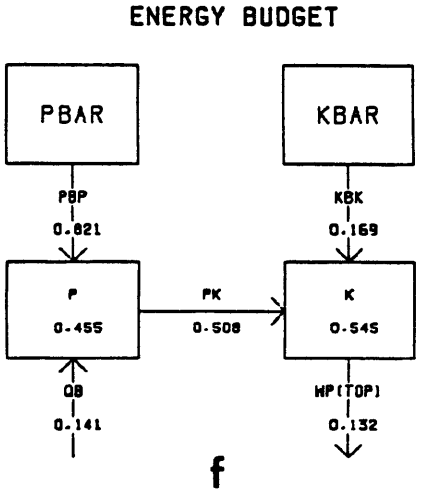

f

Fig. 4.9 (continued).

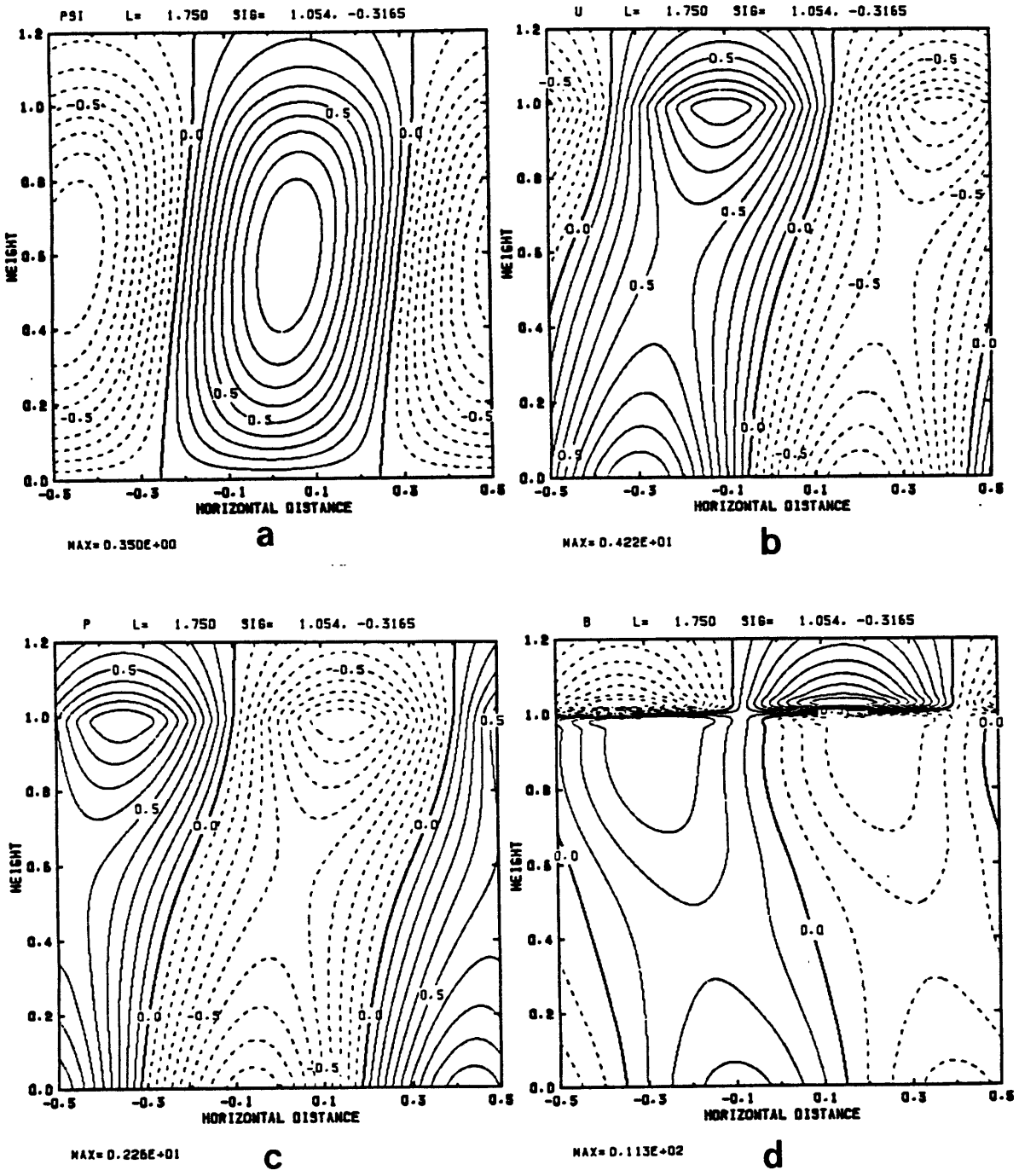

Fig. 4.10: As Fig. 4.6, but for the reference run Eady mode with z_m=0.8, at ℓ=1.75 and α=90°.

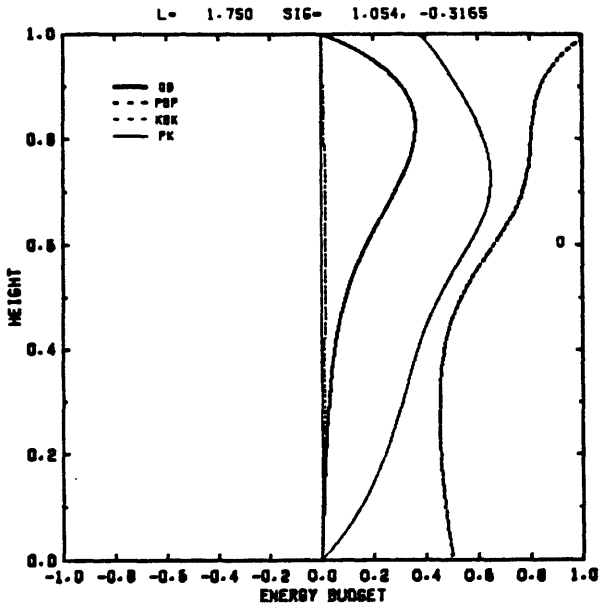

e

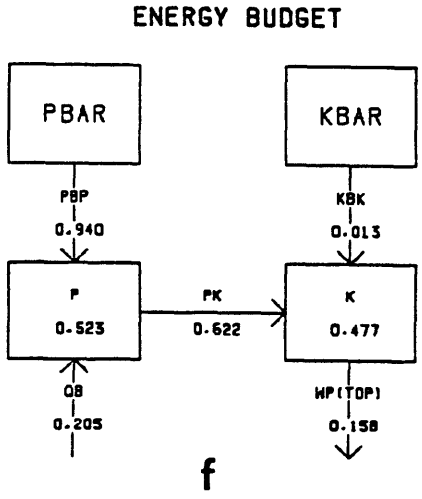

f

Fig. 4.10 (continued).

4.1.2 Symmetric mode

The symmetric mode is of greater interest than the Eady mode for the purposes of a squall line theory, for several reasons: the wavelength of the Eady mode is clearly on the synoptic scale, and its growth rate is influenced only to a small degree by convective heating. For this reason, the remainder of this thesis will concentrate solely on the symmetric mode, which is a true wave-CISK disturbance in the sense that its growth ceases in the absence of convective heating.

a) Growth rates and phase speeds

The most important properties of the symmetric mode are apparent from Fig. 4.1, which shows a contour plot of growth rate versus wavenumber and orientation angle. The maximum growth rates, the values of which do not change much with z_m, occur at a finite wavenumber, which decreases from ℓ=14 to ℓ=10 as the level of maximum heating is raised from 0.5 to 0.8. The angle of orientation is also sensitive to the heating profile: the angle of the fastest growing mode changes from α=-30° for z_m=0.5 to α=0° for z_m=0.8, and while there are virtually no growing wave-CISK modes at positive α for the sinusoidal heating profile, positive angles are favored over negative angles for z_m=0.8.

Fig. 4.11 shows curves of growth rate and phase speed as a function of total wavenumber, for z_m=0.5 and for different values of the orientation angle. Not all curves that were used for Fig. 4.1 are reproduced in Fig. 4.11. For α=0, and for α=+10°, two separate modes exist with distinct growth rate maxima. These correspond to the short wave and long wave modes discussed by Emanuel (1982). As was noted by

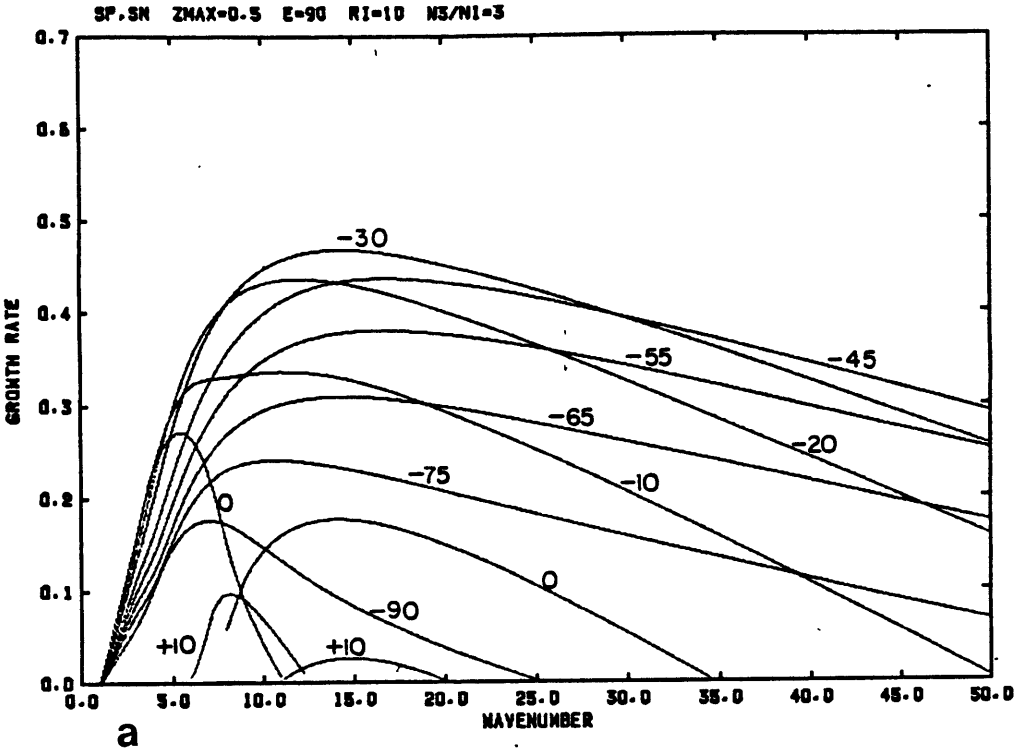

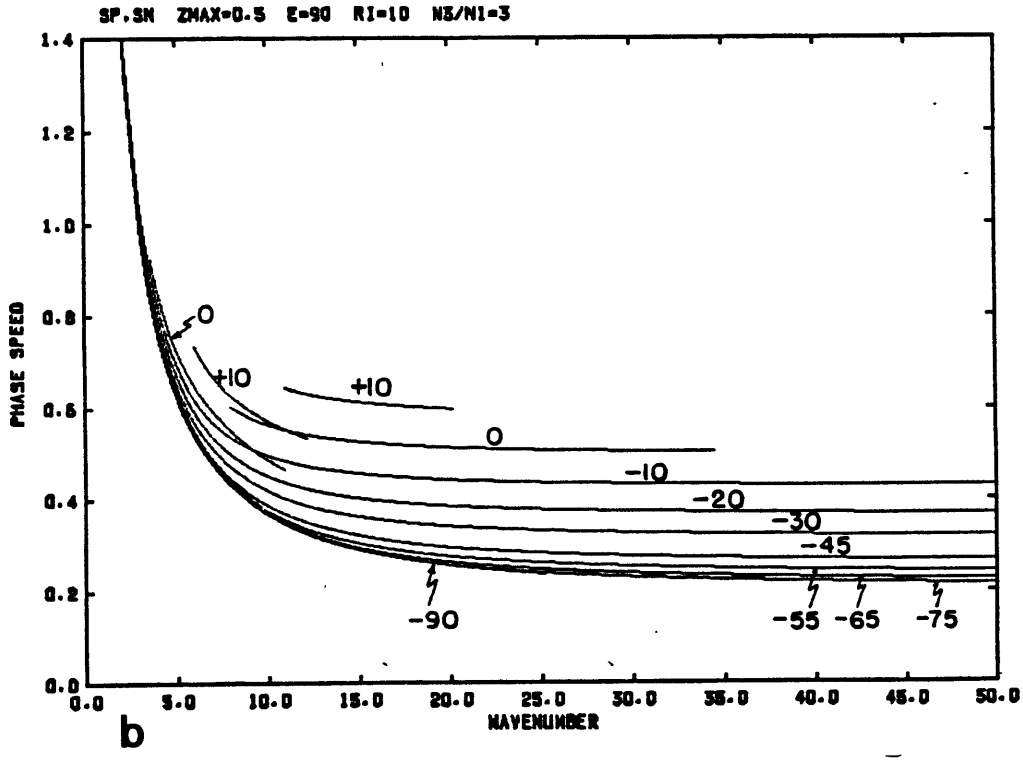

Fig. 4.11: Results for the wave-CISK mode, for the reference run with z_m=0.5. Growth rate (a) and phase speed (b) are shown as a function of total wavenumber. Curves are labeled with the value of the angle α.

Emanuel, their phase speeds are similar, but not equal, where the two modes overlap. For negative orientation angles, as well as for different heating profiles, these two modes merge and form a single mode. In this case the short wave and long wave part of the spectrum have similar characteristics as the short wave and long wave modes in the case of two modes. For this reason, and since the largest growth rate occurs at negative orientation angles for z_m=0.5, the existence of two distinct growth rate peaks at α=0 and α=+10° is of little practical consequence. Another difference between growth rate curves at different angles is the tendency for a more gradual short wave cutoff for neagtive orientation angles, as long as they are larger than -90°.

The phase speed curves reveal the physical nature of the wave-CISK modes, since their propagation will largely be governed by the dynamics of the corresponding free modes of the atmosphere. At small ℓ we notice a sharp decrease of the phase speed with wavenumber, for large ℓ an asymptotic approach to a constant value. For α=0, the (dimensional) frequency approaches the inertial frequency f at small wavenumbers, while the asymptotic phase speed value at large ℓ corresponds to that of a gravity wave that is confined to the lower half of the domain. The wave-CISK modes are inertial gravity waves, modified by and growing because of convective heating. At small wavenumbers they are dominated by Coriolis forces, at large wavenumbers by pure gravity wave dynamics. The maximum growth occurs at an intermediate wavenumber, indicating the importance of both effects for the wave-CISK mode. The dependence of the phase speed on the orientation angle reflects the influence of the Doppler-shift by the cross-line component of the basic state wind: it is increased for positive angles and decreased for negative angles. The difference in phase speed

between different angles is typically less than half the Doppler-shift at the top of the domain. This fraction becomes small for small wavenumbers, and it increases with the orientation angle. For example, the difference in the phase speed at ℓ=15 between α=0 and α=+10° is larger than that between α=0 and α=-10°. There are no "critical levels", at which the real part of the Doppler-shifted frequency becomes equal to +f, -f, or 0, at any wavenumber or orientation angle.

Fig. 4.12, 4.13, and 4.14 show the growth rate and phase speed curves for z_m=0.6, 0.7, and 0.8. Note that a different set of orientation angles is displayed for z_m=0.8. Aside from the aforementioned shift of growth rate maxima to larger orientation angles and smaller wavenumbers, we note a much sharper short wave cutoff for heating profiles with higher levels of maximum heating. In contrast to z_m=0.5, growth rates decrease less rapidly with wavenumber for positive than for negative orientation angles. The phase speeds show a general increase for larger z_m, at all orientation angles. The reason for this increase will become apparent in the next section. The difference in phase speed between different orientation angles increases with z_m, as well, although by too little to be visible on the figures. There are again no critical levels for these wave-CISK modes.

Several questions arise from the results of this section. The dependence of the growth rate on the orientation angle makes it important to understand the role of the cross-line component of the mean wind shear in the growth of the disturbance. A related question is how different vertical profiles of the convective heating affect the interaction of the perturbation with the basic state, and the dependence of growth rate on wavenumber. These questions will be addressed in the next section with an analysis of the eigenfunctions and the energetics.

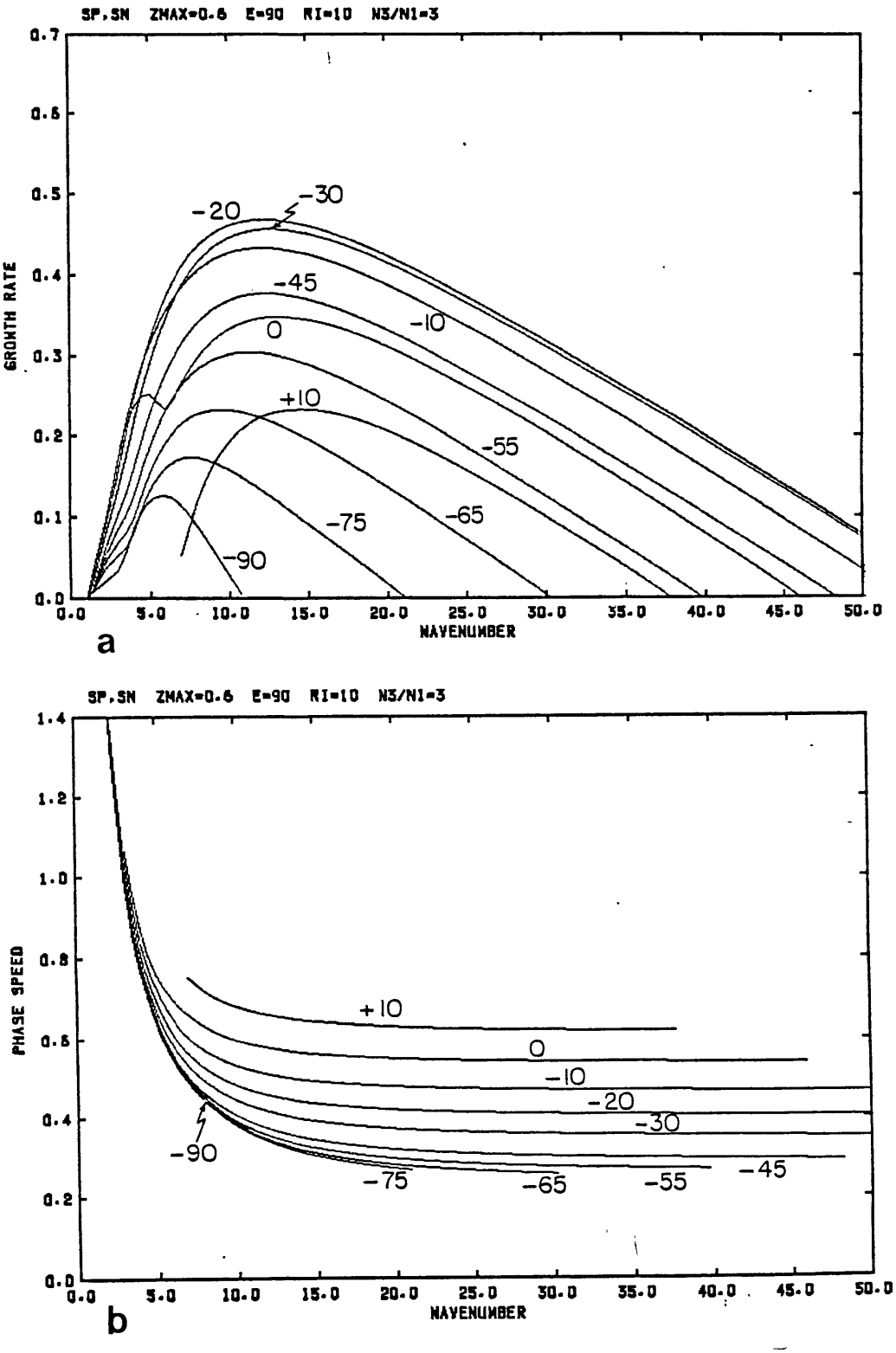

Fig. 4.12: As Fig. 4.11, but for z_m=0.6.

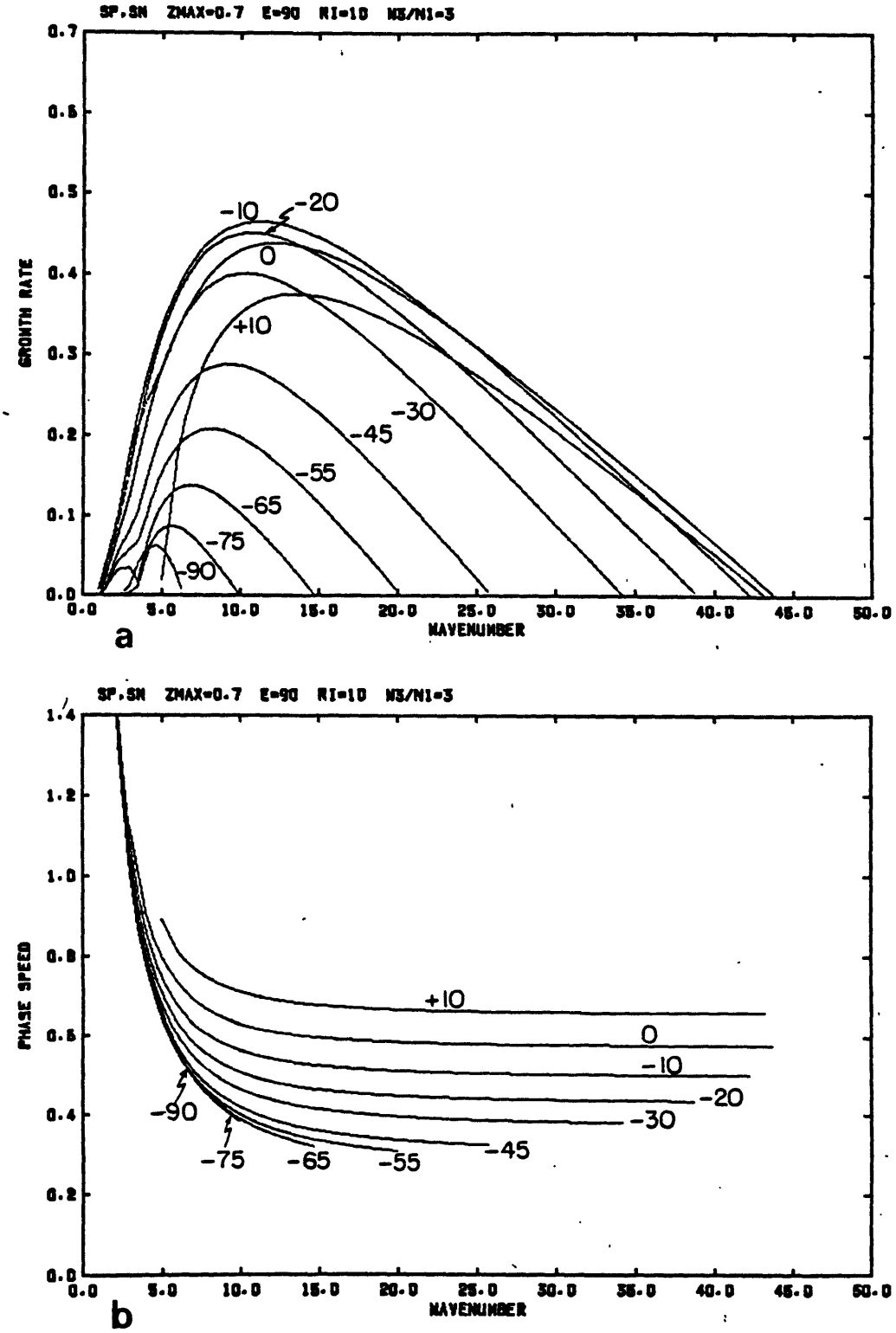

Fig. 4.13: As Fig. 4.11, but for z_m=0.7.

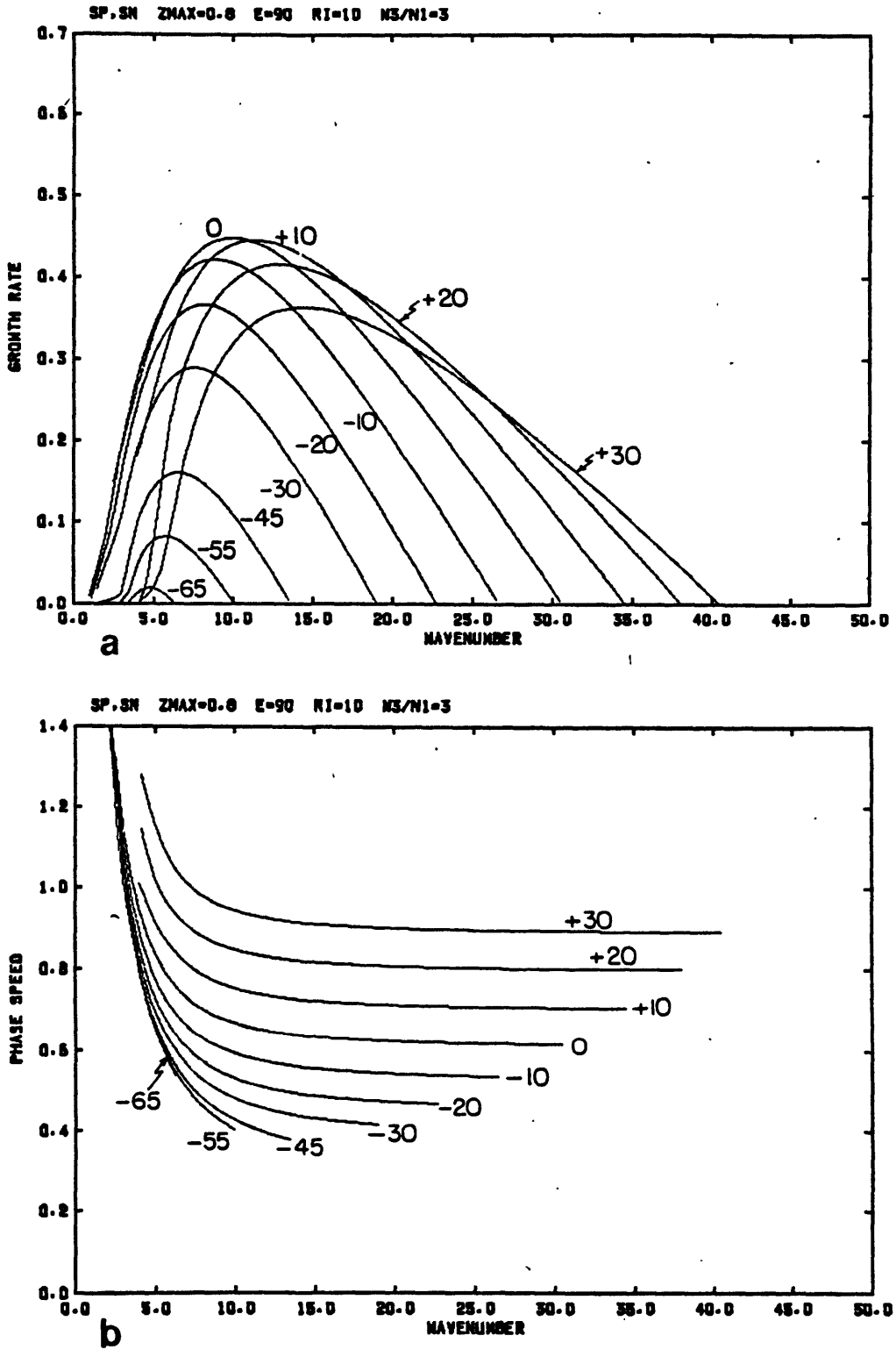

Fig. 4.14: As Fig. 4.11, but for z_m=0.8.

b) Vertical structure and energetics

In order to separate effects of wavenumber, cross-line shear and heating profile on the structure and energetics of the perturbations, solutions along the symmetric axis are considered first. The fastest growing mode for z_m=0.8, at α=0 and ℓ=10, is analyzed and compared to a solution at a smaller wavenumber to assess the influence of the wavenumber. Different values of z_m, and finally α, are then chosen to demonstrate the effects of the heating profile and the cross-line shear.

Fig.4.15 shows the vertical structure at ℓ=10 and α=0, for z_m=0.8. The wave is propagating to the left in this and all following diagrams in this section. This wavenumber and orientation angle correspond to the fastest growing mode for z_m=0.8. The streamfunction has a very different structure in the upper and lower halves of the domain. In the lower half it resembles a trapped, neutral gravity wave: there is little tilt of the streamlines in the vertical, and the buoyancy field leads the vertical velocity by approximately 1/4 wavelength. In the upper half of the domain, streamlines are sloping back toward the cold air, at a slope somewhat shallower than that of an angular momentum surface (indicated by the heavy dashed line). The buoyancy field tilts slightly in the direction of propagation. It is characterized by a couplet of positive and negative buoyancy. The along-line velocity and the perturbation pressure reach their maximum amplitudes at the surface. The energy budget shows the generation of eddy available potential energy by convective heating (QB) as by far the most important energy source, with conversions of mean to

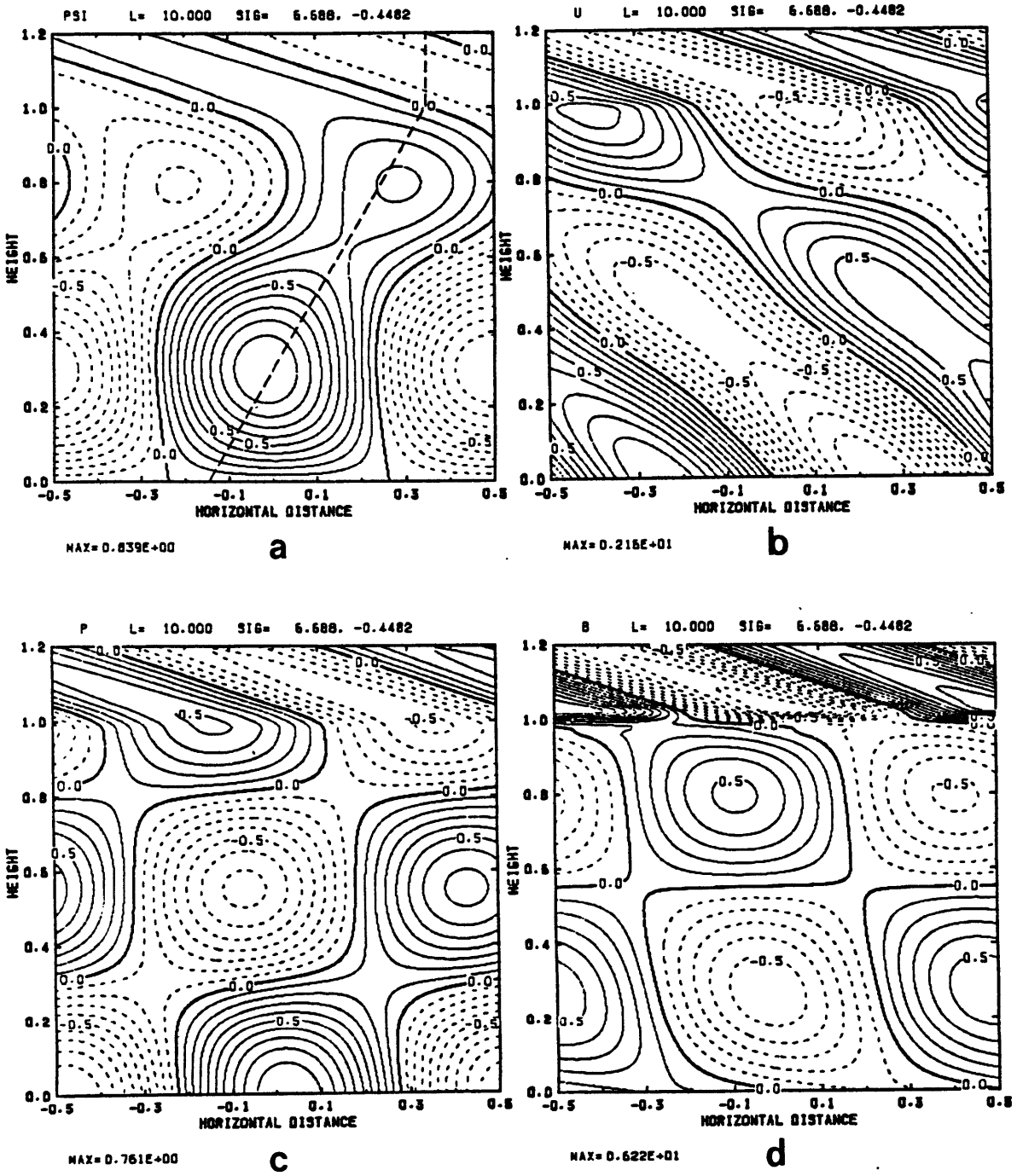

Fig. 4.15: Vertical structure and energetics for the wave-CISK mode, for the reference run with z_m=0.8, at ℓ=10 and α=0°. Contour plots of the nondimensional ψ'(a),u'(b), p'(c), and b'(d), normalized by their maximum value in the domain (given at the bottom of each panel). The dashed line in a) indicates an angular momentum surface. e): energy conversion terms as a function of height, normalized by the maximum value. f): vertically integrated energy budget.

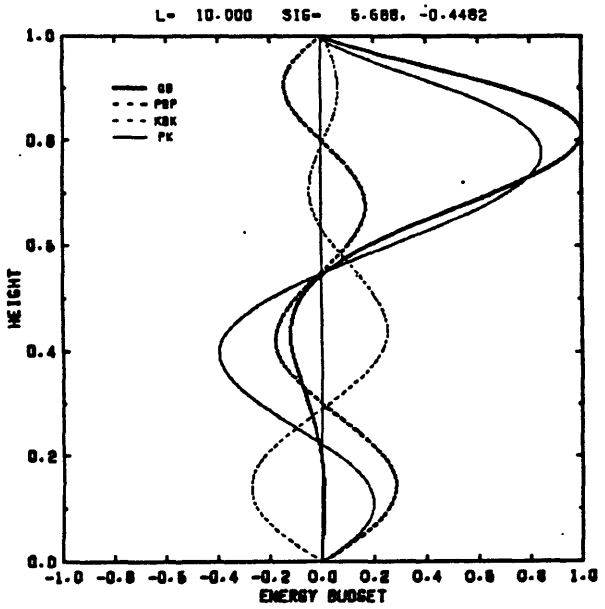

e

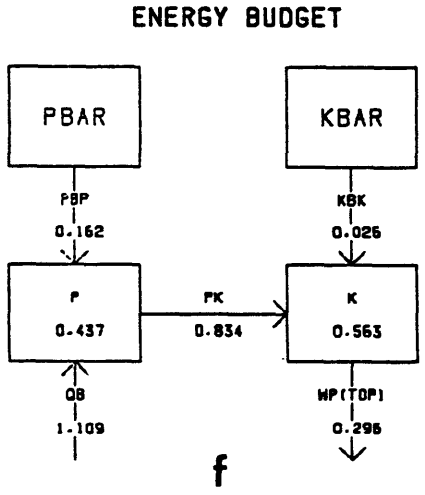

f

Fig. 4.15 (continued).

eddy potential and kinetic energy (PBP and KBK) contributing smaller amounts. The loss of energy through the tropopause represents an important energy sink for the disturbance. The vertical distribution of the terms of the energy budget shows relatively small values of PK in the lower half of the domain, indicating that the vertical velocity and the buoyancy are nearly out of phase there. The heating energy generation QB is insignificant in that region, and strongly positive above. The crucial energy source of the disturbance is thus concentrated in the upper part of the domain.

Dimensional values for this fastest growing mode are obtained in the same manner as for the Eady mode. The wavelength is 630 km, and the e-folding time is 20 hours. The eigenfunction amplitudes correspond to, assuming a maximum vertical velocity of 20 cm/s, 5.2 m/s for u*, 1.8 mb for p*, and 4.6 K for the potential temperature perturbation.

The effects of a smaller wavenumber can be seen by comparison with Fig. 4.16, which shows the solution at ℓ=6 and α=0 for z_m=0.8. There are some minor differences in the streamfunction profile, most notably a lowering of the circulation center and of the onset of the backward slope of the streamlines for the case of ℓ=6. The slope is again shallower than that of an angular momentum surface. The buoyancy profile shows a more tilted structure in the lower half of the cold-warm couplet, and a weaker amplitude in the upper half. Comparisons of amplitudes and energy terms are based on a renormalization that assumes equal total perturbation energies of the two disturbances; this is the same procedure that was followed in the discussion of the Eady modes. The p and u fields are quite similar for the two wavenumbers. The energy budget shows a smaller energy generation QB for ℓ=6, which is linked to the smaller amplitude of

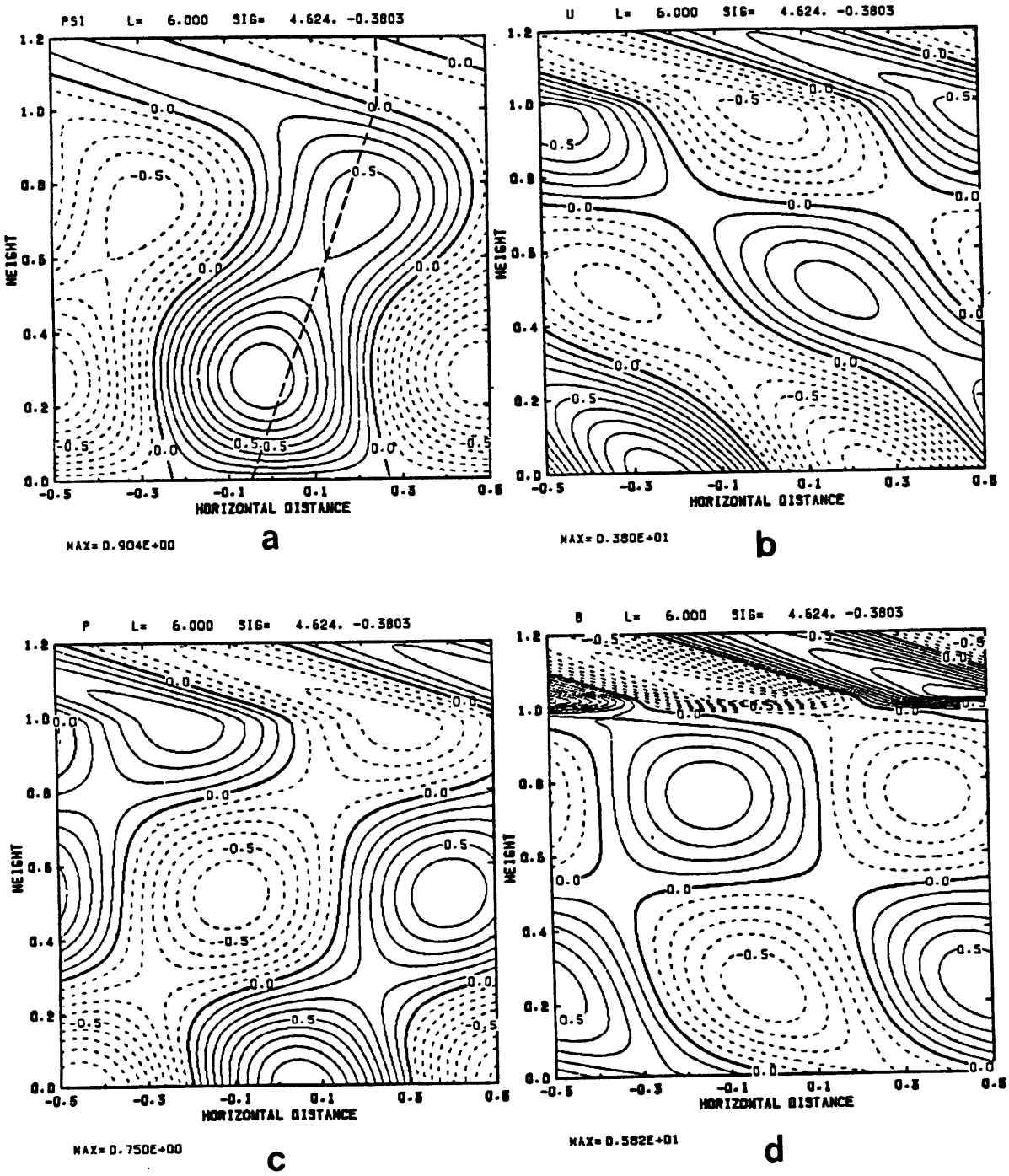

Fig. 4.16: As Fig. 4.15, but for ℓ=6.

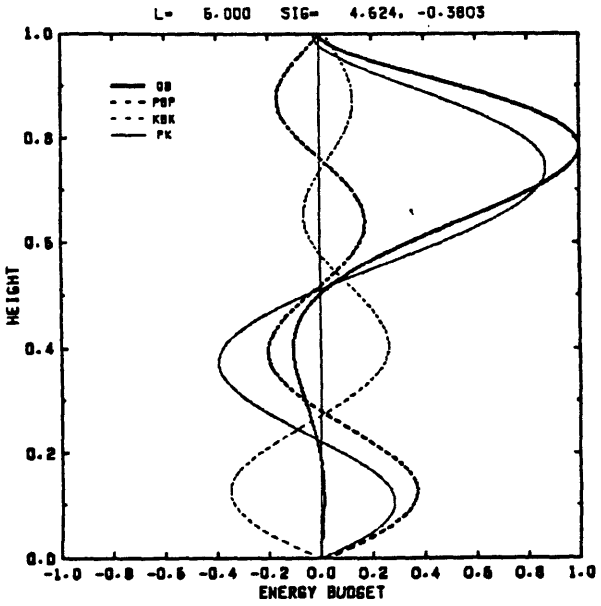

e

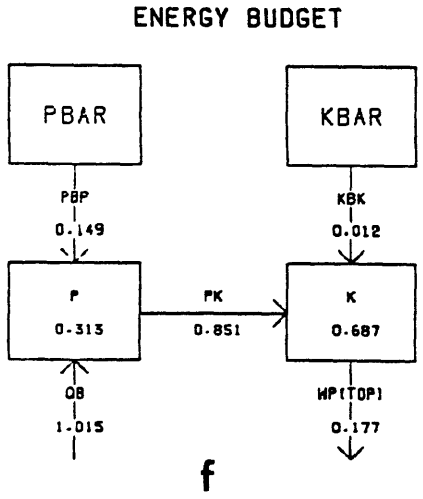

f

Fig. 4.16 (continued).

b in the upper troposphere. PBP and KBK are decreased as well, but this does not affect the energy budget significantly since they contribute only a small part of the total energy. A more important difference is the smaller energy loss to the stratosphere, which partially compensates for the decrease in QB. Similar comparisons between small and large ℓ at $\alpha=0$ for $z_m=0.6$ and $z_m=0.7$ show qualitatively equal differences in the energy budgets. In the case of a sinusoidal heating profile, the heating generation is slightly larger at the long wave peak than at the short wave peak; the remaining terms in the energy budget, in particular WP, still show the same behavior as for the other heating profiles.

A different heating profile by itself leads to some changes in the vertical structure, as can be seen from Fig. 4.17, which shows the same solution as Fig. 4.16, except for $z_m=0.5$. The circulation center is further lowered for $z_m=0.5$, and the backward slope of the streamfunction aloft is less shallow, such that it is close to the slope of an angular momentum surface there. The corresponding profiles of u, p, and b all show a similar concentration of wave energy in the lower half of the domain. The buoyancy field, as well as the along-line velocity field, also show a stronger tilt toward the warm air below z=0.6. This altered buoyancy profile is less favorable for the generation of eddy available potential energy, as evidenced by the increased negative area of QB, which leads to a drastic reduction in the integrated value of QB. A beneficial effect of the shallower structure of the disturbance is a reduction of the energy loss to the stratosphere, which becomes insignificant as an energy sink for $z_m=0.5$. Energy conversions from the mean state are both slightly increased, but they do not play a large role in the energy budget.

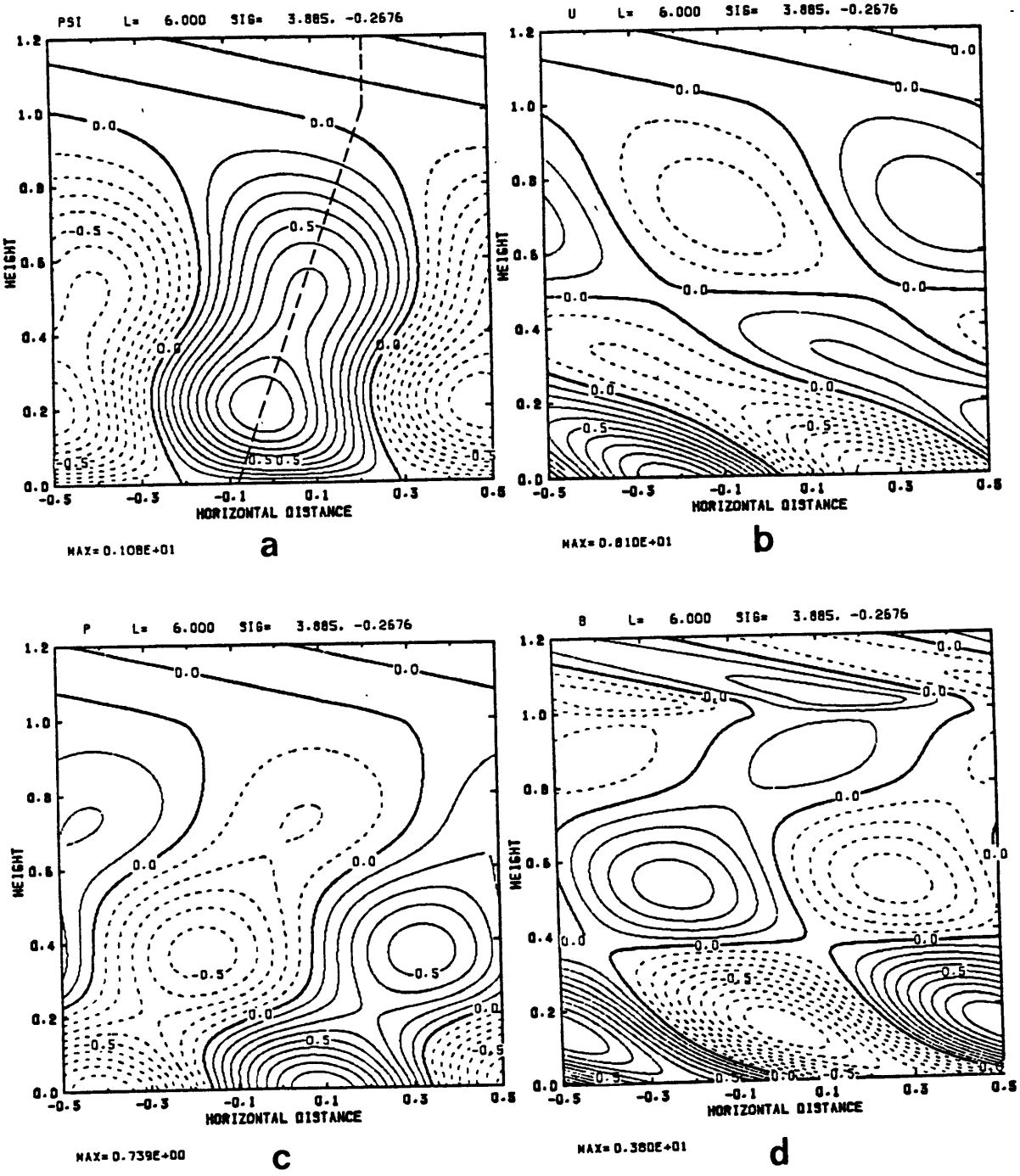

Fig. 4.17: As Fig. 4.15, but for z_m=0.5.

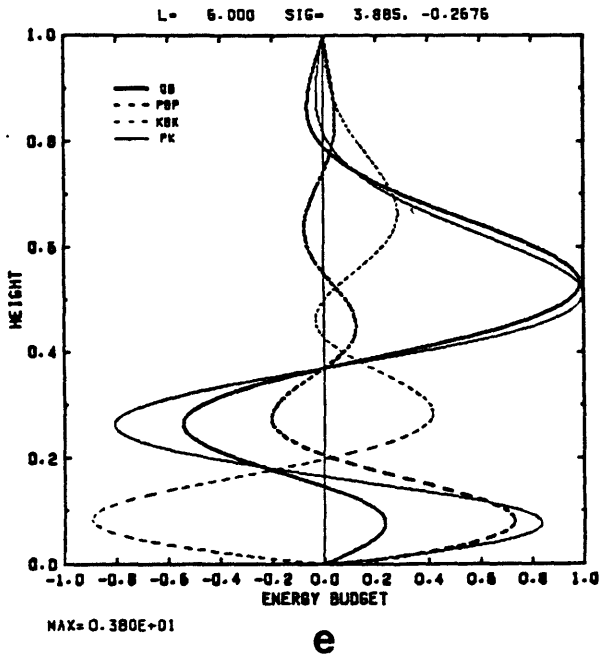

e

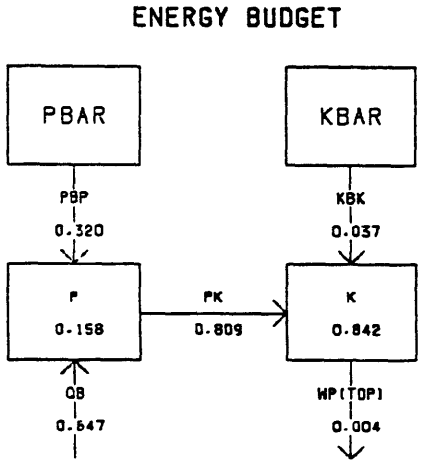

f

Fig. 4.17 (continued).

Similar comparisons between different heating profiles at equal wavenumbers (ℓ=6 and ℓ=14, not shown here) establish the generality of the most important changes described above. In particular, a higher level of maximum heating leads to a deeper disturbance, evident in all of the perturbation fields. This is accompanied by larger values for the heating generation of energy, which has its positive values in the upper half of the domain, and by larger energy losses through the tropopause. Smaller changes in the energy budget, related to the basic state energy conversions, depend on the particular wavenumber and heating profile. Another manifestation of the deeper disturbance for a larger z_m is an increased phase speed; a deeper disturbance implies that the gravity wave-like portion of the circulation occupies a larger region, and this increase in the vertical extent is reflected by a corresponding increase of the phase speed.

It is interesting to note that an increase in the wavenumber has a similar effect on the vertical structure as a higher level of maximum heating: both lead to a deeper disturbance with corresponding increases in QB and WP. The wavenumber of maximum growth for a given heating profile and orientation angle corresponds to a vertical structure that maximizes QB and minimizes WP. This explains the smaller wavenumbers of maximum growth for heating profiles with higher levels of maximum heating - similar vertical structures occur at smaller wavenumbers for larger z_m.

Cross-line shear of the environmental wind provides another mechanism for affecting the structure of the wave-CISK modes. Fig. 4.18 and Fig. 4.19 show the eigenfunctions for z_m=0.8 and ℓ=10 at α=+10° and α=-10°, respectively. By comparison with Fig. 4.15 the effects of shear in and against the direction of propagation can be seen. For cross-line shear in

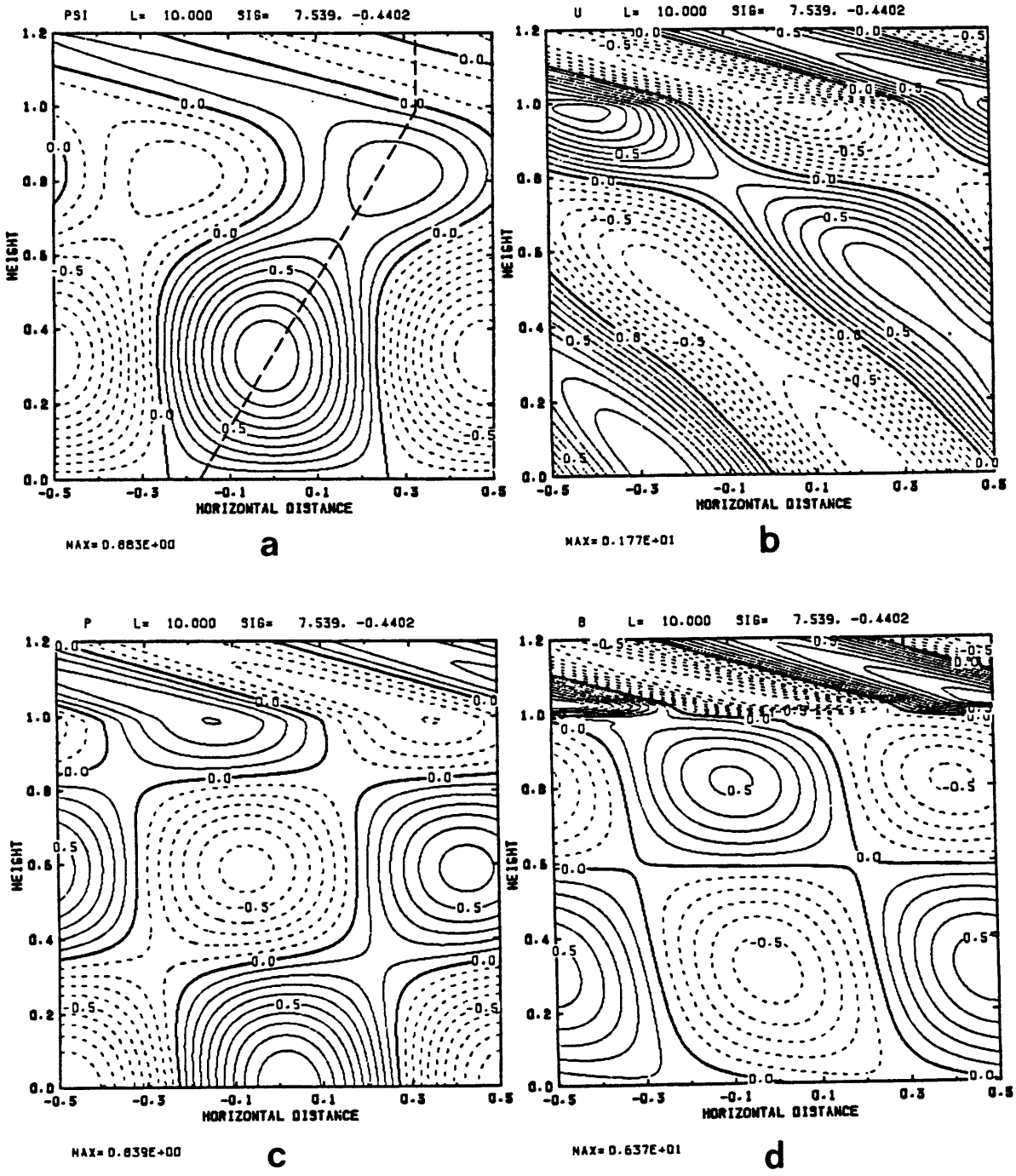

Fig. 4.18: As Fig. 4.15, but for α=+10°.

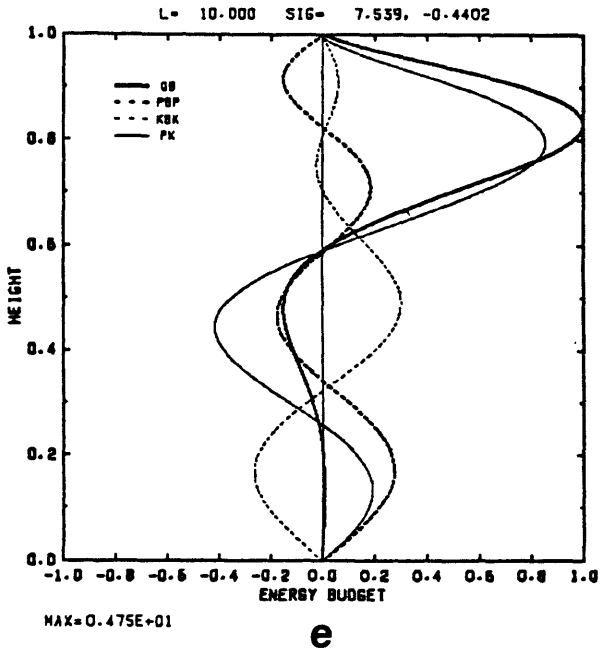

e

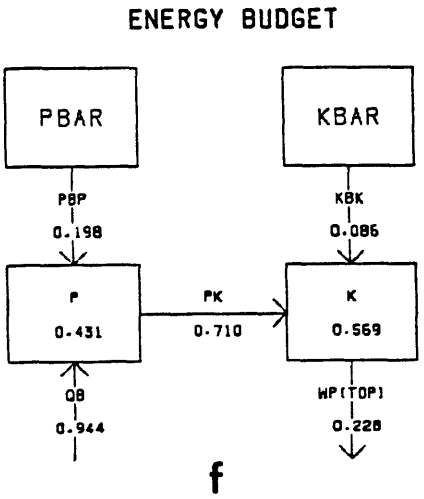

f

Fig. 4.18 (continued).

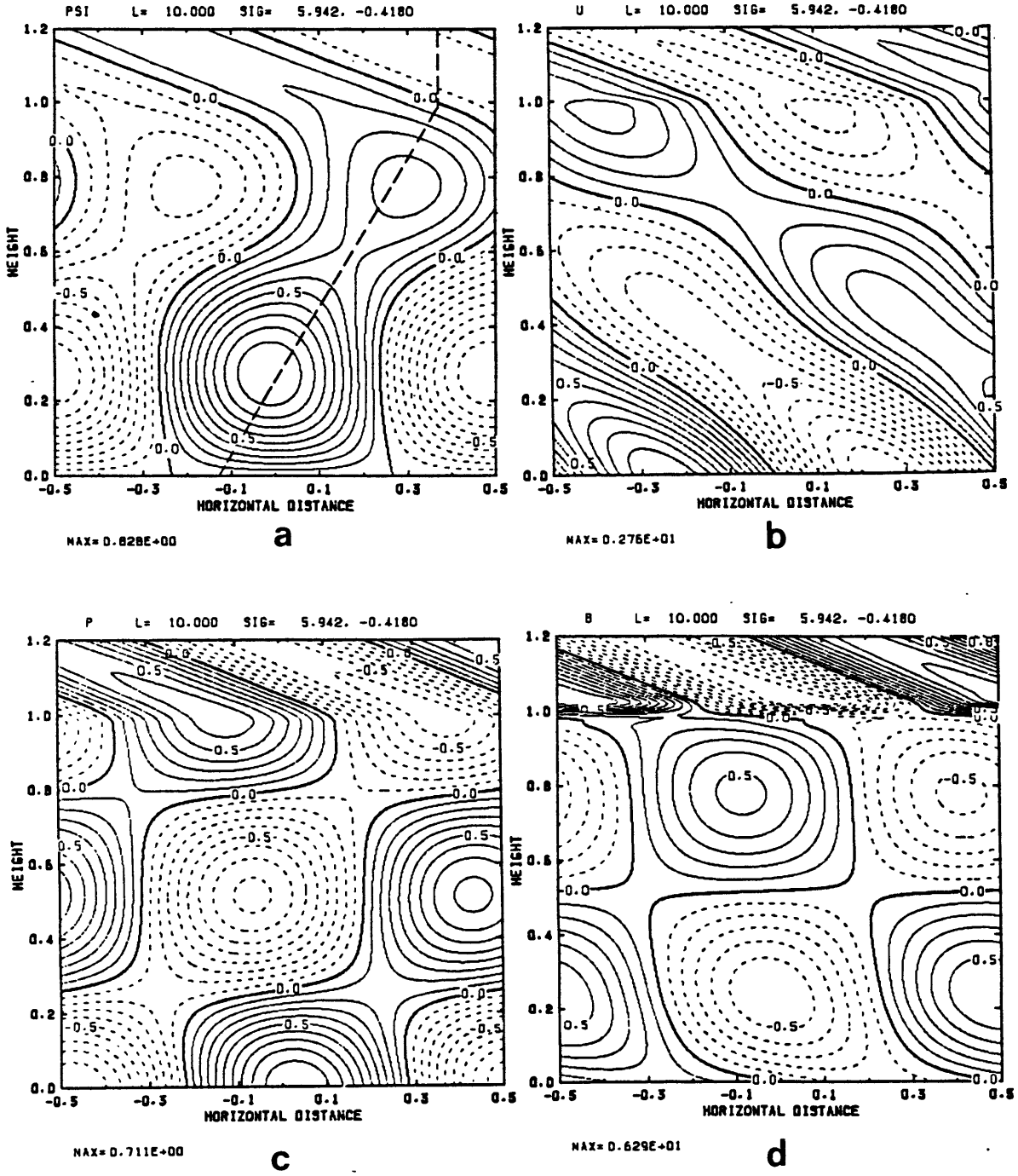

Fig. 4.19: As Fig. 4.15, but for α=-10°.

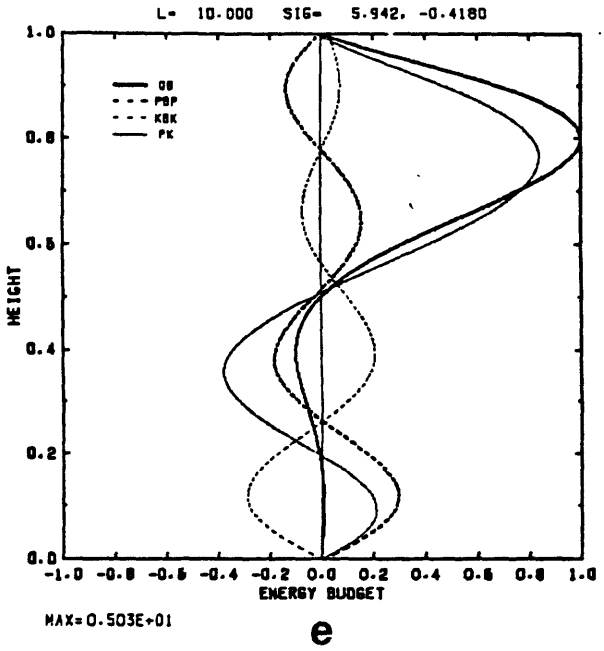

e

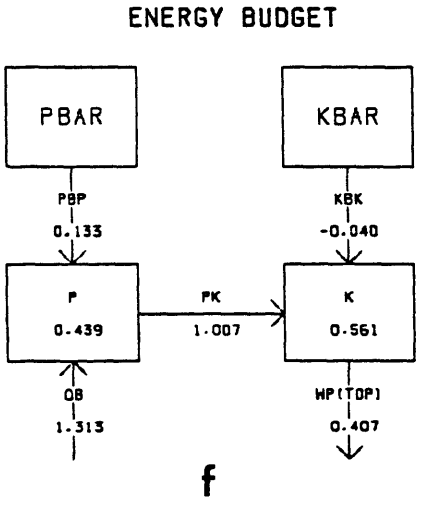

f

Fig. 4.19 (continued).

the direction of propagation (α=+10°) the disturbance is deeper, with a shorter vertical wavelength in the upper half of the domain. The opposite holds true for α=-10°. This tendency may be explained with a simple WKB argument. WKB theory shows that, to a first approximation, the dispersion relation for the local frequency and wavenumber of a wave that is traveling through a slowly varying medium is the dispersion relation for a wave in a homogeneous medium, with the environmental parameters of that location (see Bretherton, 1966, for details). Since in my case the frequency relative to the ground and the horizontal wavenumber are constant, a Doppler-shift that decreases the frequency relative to the fluid has to be compensated for by a corresponding decrease in the vertical wavelength. Although WKB theory is not strictly valid in my case since the environmental flow changes over a scale comparable to the vertical wavelength, it is nevertheless useful in explaining the tendency of the disturbance to respond to cross-line flow in the direction of propagation with smaller vertical wavelengths.

As a result of this change in the vertical structure, the area of positive correlation between heating and buoyancy is smaller and shifted upward for positive orientation angles. The integrated value of QB is thus larger for cross-line shear opposite the direction of propagation. Since for z_m=0.8 most of the heating is concentrated near the tropopause, the growth rate is not as sensitive to the cross-line shear as for the other heating profiles. Another difference from the other heating profiles is the increased WP for α=-10°, which, together with decreased energy conversion from the mean flow, counteracts the increase in QB and leads to a slower growth rate. Other heating profiles show a change of WP of opposite sign, so that the sensitivity to the orientation angle is

increased. The tendency of the kinetic energy source to become negative for negative orientation angles is a persistent feature of all the heating profiles. Near the symmetric axis, it is still a negligible part of the energetics, but this no longer is the case at larger (positive or negative) orientation angles.

The fastest growing mode for a sinusoidal heating profile (z_m=0.5), shown in Fig 4.20, has α=-30° and ℓ=14. It has a structure quite different from the fastest mode for z_m=0.8 (Fig. 4.15). It is much shallower, and streamlines tilt back throughout most of the troposphere. In both cases the single most important energy source of the disturbance is the generation of eddy available potential energy by convective heating. The major difference in the energy budget is the loss of kinetic energy to the mean flow in the case of z_m=0.5, which is a more important energy sink than the energy flux through the tropopause at that value of z_m. The dimensional values of the wavelength L, e-folding time T, and eigenfunction amplitudes for Fig. 4.20 (for basic state parameters as before and w^*_m=20 cm/s) are given by:

L=450 km

T=19 hours

u*=7.8 m/s

p*=1.0 mb

θ*=2.0 K.

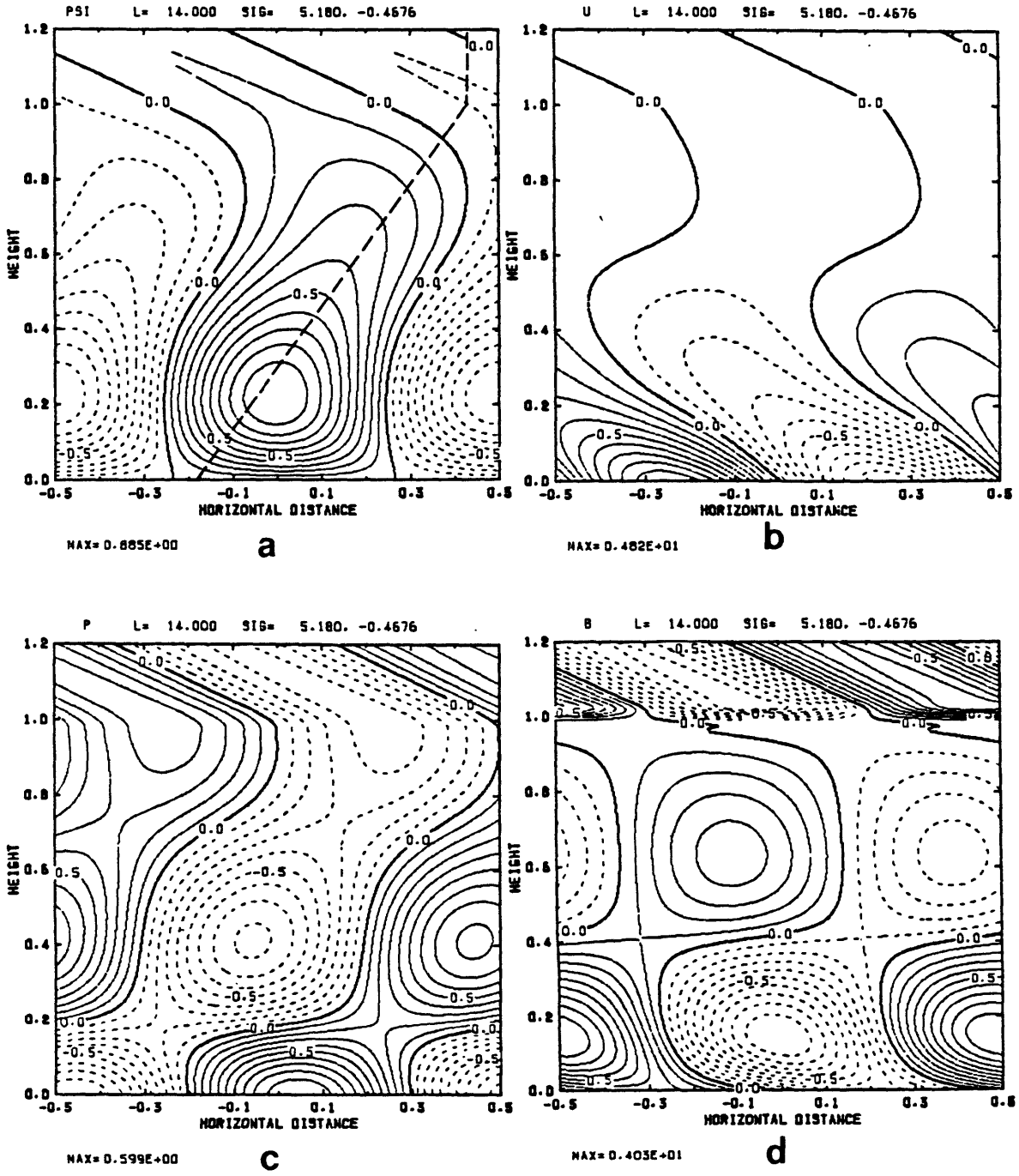

Fig. 4.20: As Fig. 4.15, but for z_m=0.5, at ℓ=14 and α=-30°.

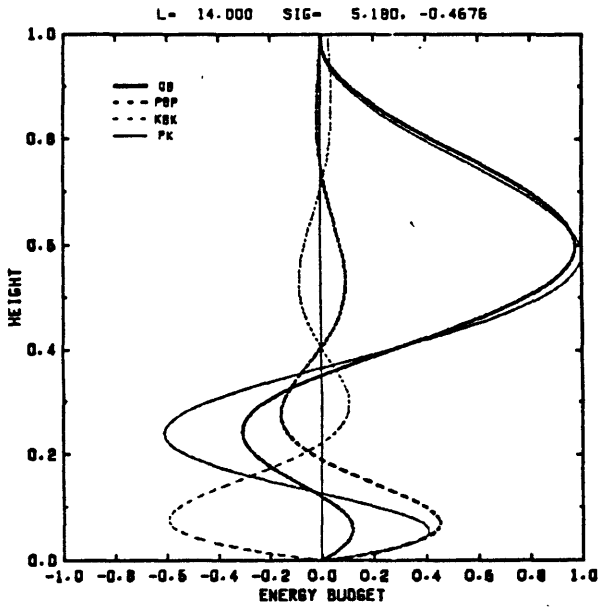

e

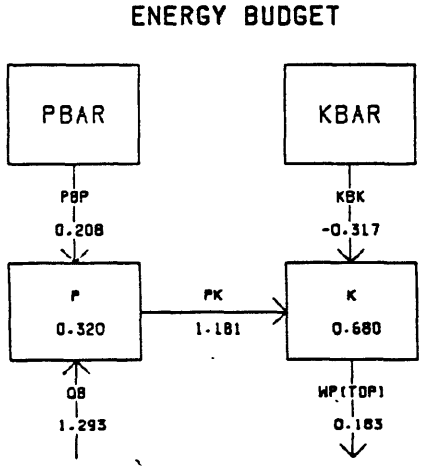

f

Fig. 4.20 (continued).

4.2 Sensitivity to heating rates

The wave-CISK mode depends on the convective heating for its growth and is thus very sensitive to the heating amplitude. Calculations have been carried out for precipitation efficiencies ranging from 30% to 110%. For efficiencies below 30% the growth rates become too small for the numerical method to locate the solution, and for E above 95% (for z_m=0.5) and 105% (for z_m=0.6, 0.7, and 0.8) growth rates increase monotonically with wavenumber. Fig. 4.21, 4.22 show the growth rate and phase speed curves at E=70% for selected orientation angles for z_m=0.5 and z_m=0.8. Compared to the reference run with E=90% (note the different growth rate scales), growth rates are decreased overall, but the largest decrease occurs at large wavenumbers. This is especially pronounced for z_m=0.8. From the preceeding discussion of the wave-CISK energetics this is plausible: the convective heating provides an increasingly large share of the perturbation energy as the wavenumber and the height of the maximum heating are increased. For heating rates at and below the 70% precipitation efficiency value, the growth rate of the fastest growing wave-CISK mode is smaller than that of even the adiabatic Eady mode. The phase speeds are decreased very slightly for decreased heating amplitudes.

The properties of the fastest growing wave-CISK mode, for all four heating profiles and for the whole range of heating amplitudes, are summarized in Table 4.1 and Fig. 4.23. The maximum growth rate increases with the precipitation effiency, until at E=100% (z_m=0.5) and E=110% (z_m=0.6 - 0.8) it no longer occurs at a finite wavenumber. For these heating amplitudes this model reproduces the barotropic wave-CISK result. Emanuel (1982) found this to occur at somewhat larger heating amplitudes for strictly symmetrical disturbances. The differences in growth rates of

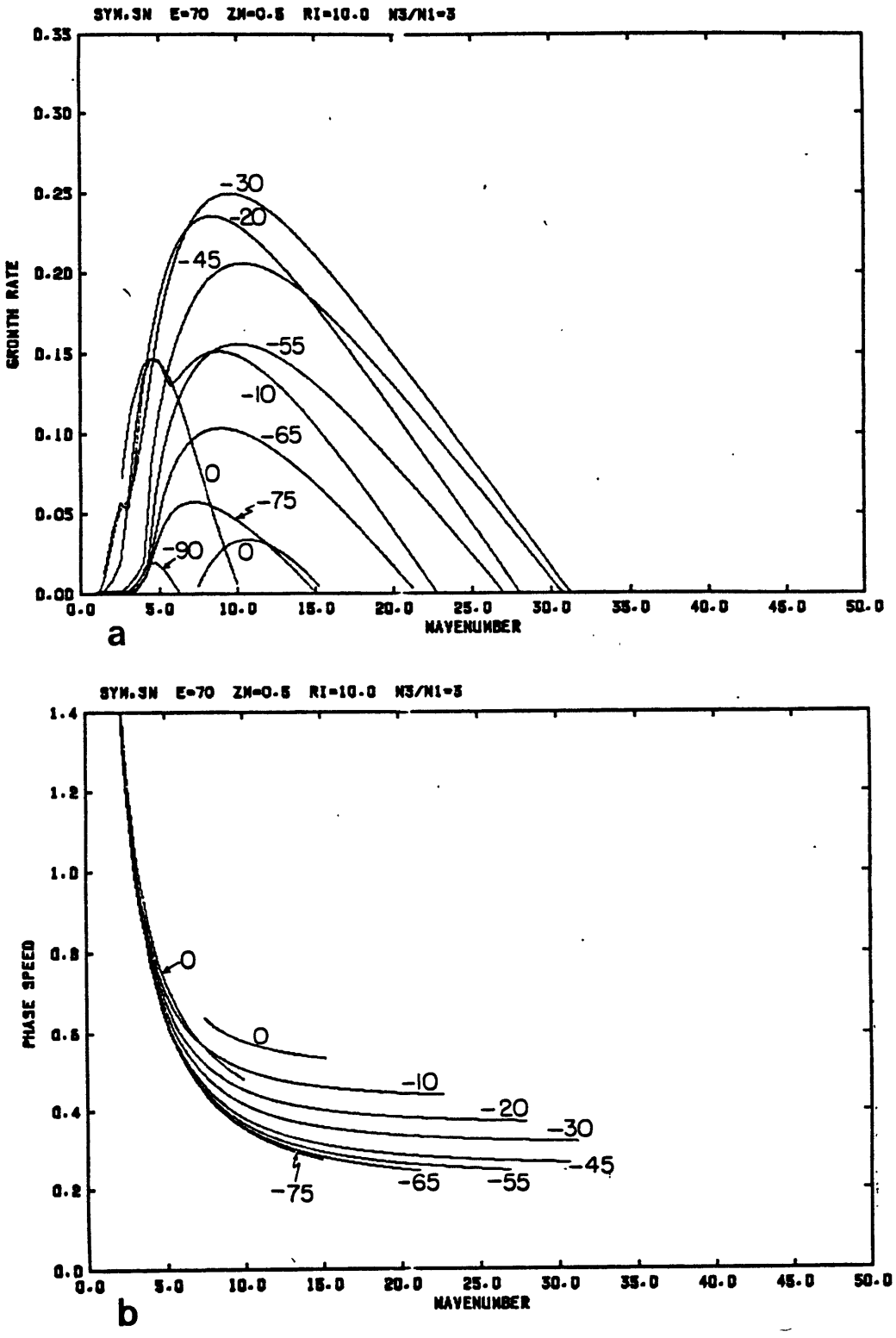

Fig. 4.21: As Fig. 4.11, but for E=70% and z_m=0.5.

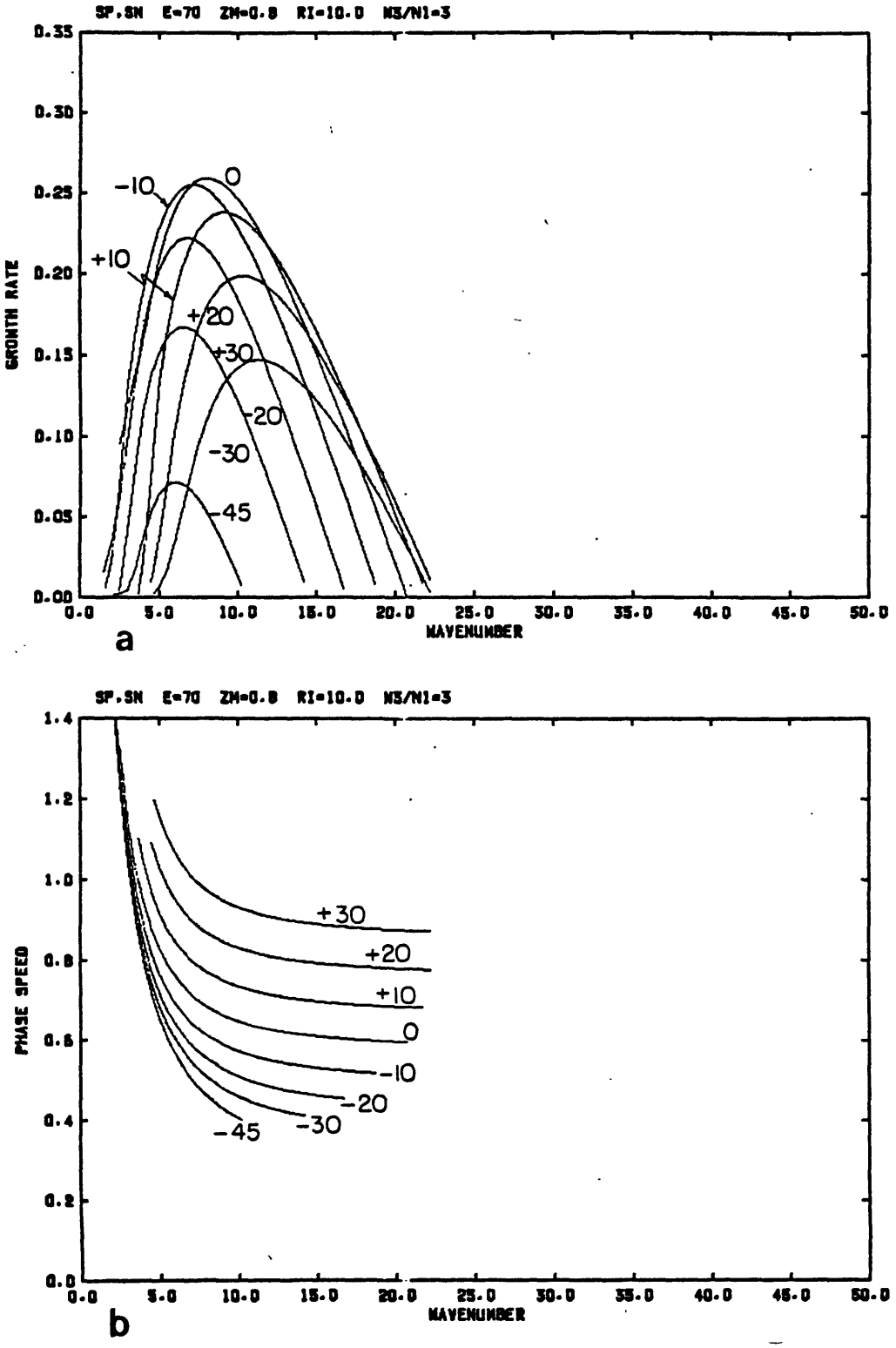

Fig. 4.22: As Fig. 4.11, but for E=70% and z_m=0.8.

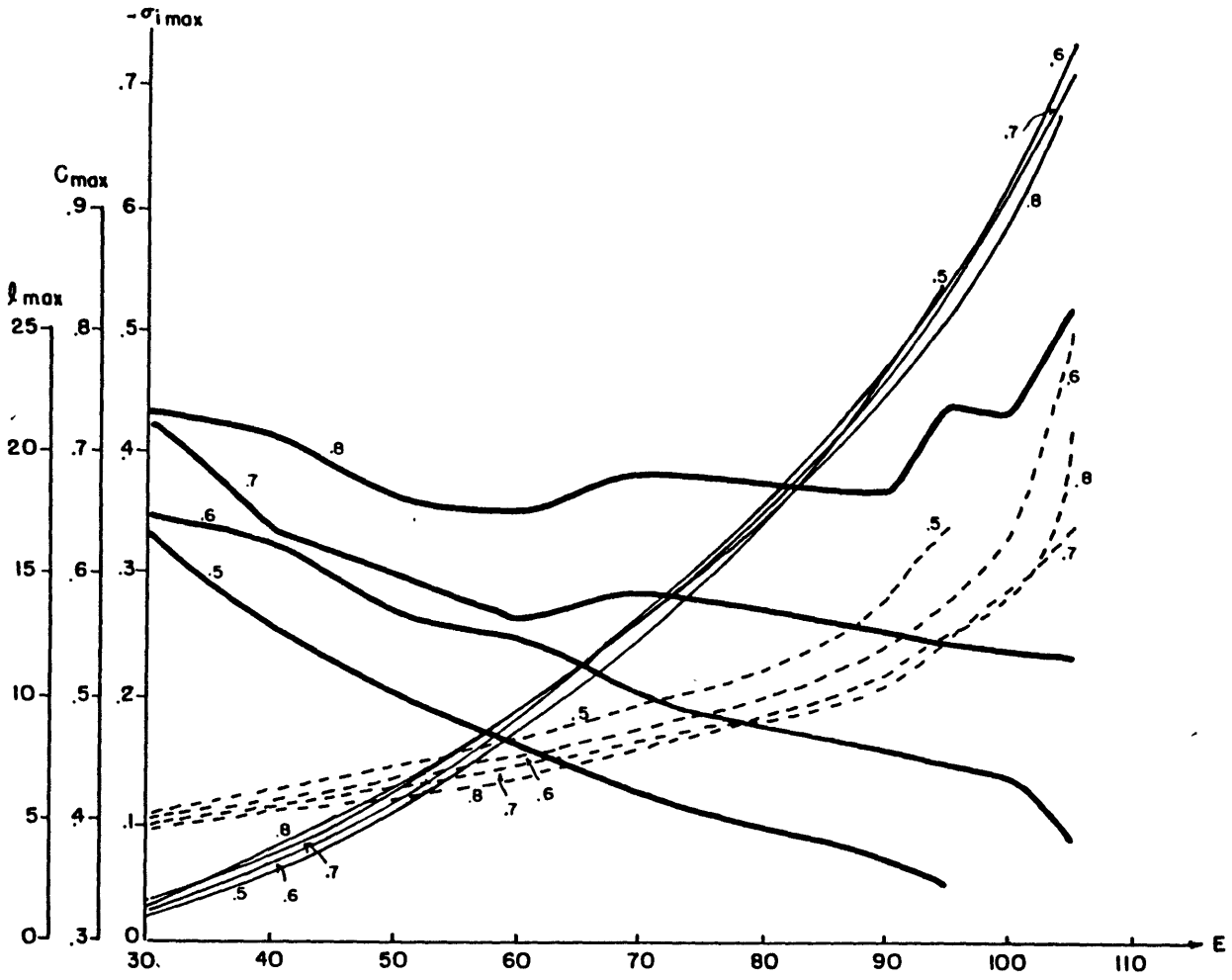

Fig. 4.23: Characteristics of the fastest growing wave-CISK mode as a function of the precipitation efficiency E. Shown are the growth rate $-\sigma_{i,max}$ (thin solid line), the phase speed c_{max} (thick solid line), and the wavelength ℓ_{max} (dashed line). All curves are labeled by the value of z_m.

different heating profiles are too small to be detected on the graph; at small values of E, the largest growth rate corresponds to the smallest value of z_m (0.5), while the situation is reversed at larger E. The wavenumber of the fastest growing mode triples over the whole range of E, but most of this increase occurs at heating rates close to the critical value with respect to the short wave cutoff. The orientation angle of the fastest growing mode is unchanged for z_m=0.5, but it increases with E for higher levels of maximum heating.

Table 4.1: Orientation angle α of the fastest growing wave-CISK mode as a function of precipitation efficiency E.

	E (%)									
z_m	30	40	50	60	70	80	90	95	100	105
0.5	-30°	-30°	-30°	-30°	-30°	-30°	-30°			
0.6	-30°	-20°	-20°	-20°	-20°	-20°	-20°	-20°	-20°	-30°
0.7	-20°	-20°	-20°	-20°	-10°	-10°	-10°	-10°	-10°	-10°
0.8	-20°	-10°	-10°	-10°	0°	0°	0°	+10°	+10°	+10°

As was mentioned above, the phase speeds are in general slightly larger for larger values of z_m and E. However, the phase speeds of the most unstable mode are more strongly influenced by two other factors: the angle of orientation, and the wavenumber of fastest growth. In the case of a constant orientation angle (z_m=0.5) the phase speed decreases monotonically with E, due to the concurrent increase in wavenumber. For

higher levels of maximum heating the observed increase of the orientation angle with E is associated with changes in the Doppler-shift which leads to a less rapid decline of the phase speed with E, or, in the case of z_m=0.8, even to an increase. The nearly stepwise character of the phase speed curves in Fig. 4.23 is an artifact of the crude resolution of the orientation angle (to the nearest 10°). More detailed calculations would result in a smoother variation of c_{max} with E.

4.3 Sensitivity to stratospheric static stability

Emanuel (1982) found that for z_m=0.5 and α=0 the short wave mode was more sensitive to this parameter than the long wave mode. This result is reproduced here, as is apparent from a comparison of the α=0 curves in Fig. 4.24 (N_s/N_t=1), Fig. 4.11 (N_s/N_t=3), and Fig 4.26 (N_s/N_t=10). The same holds true for other orientation angles and other heating profiles (for z_m=0.8 refer to Fig. 4.25 and Fig. 4.27), except that the short wave and the long wave modes are now merged to form a single mode. This further illustrates the fact that the existence of two separate growth rate peaks does not significantly affect the solution at either the short or long wave end of the spectrum. By comparing the growth rate behavior for z_m=0.5 with that of z_m=0.8 one notes a stronger increase of the growth rate with N_s/N_t for higher levels of maximum heating. This is understandable in light of the fact that the higher levels of maximum heating are associated with deeper disturbances and accordingly larger losses of energy through the tropopause. If the ratio N_s/N_t is increased to 1000, thus essentially corresponding to a

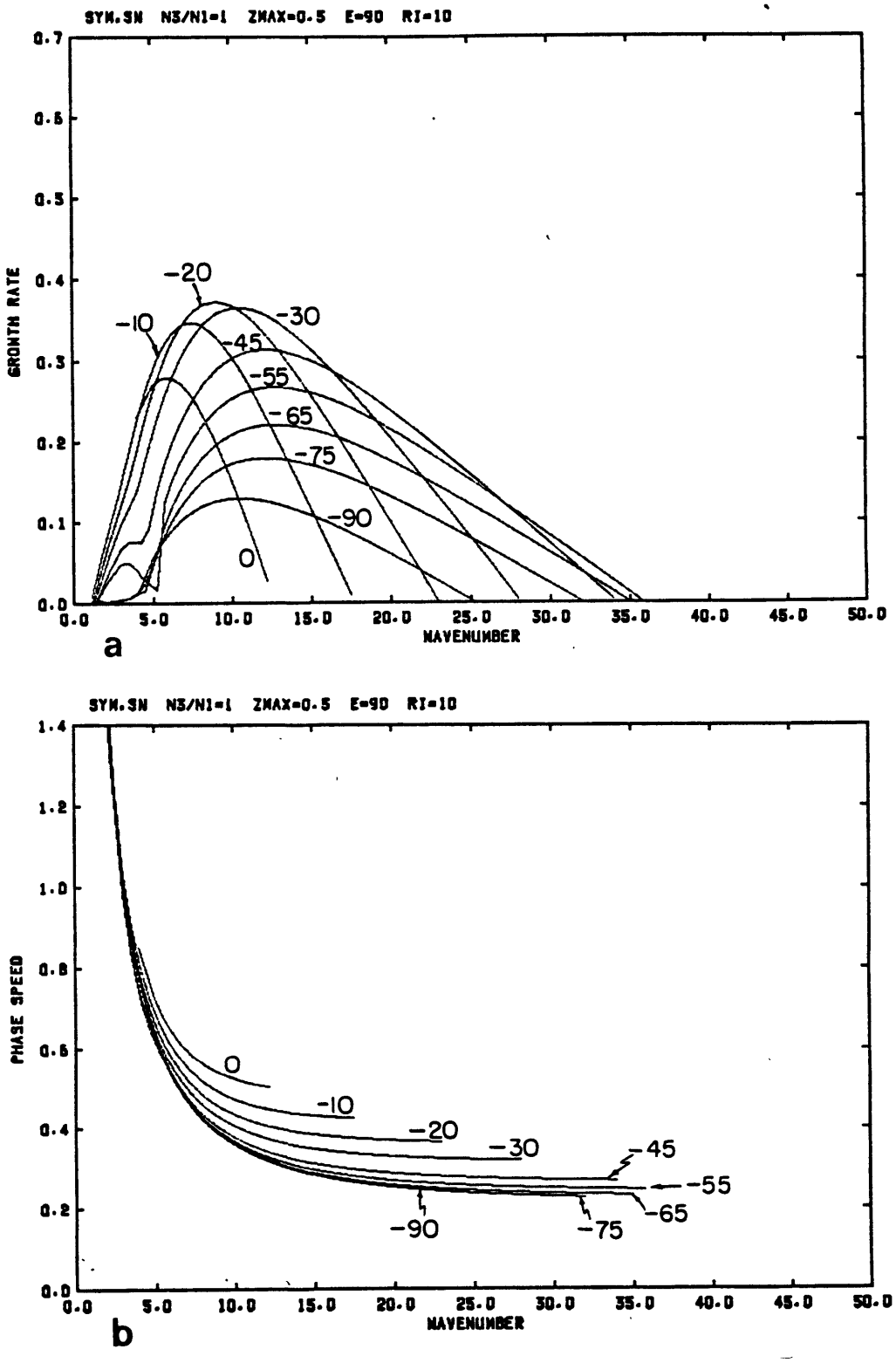

Fig. 4.24: As Fig. 4.11, but for N_s/N_t=1 and z_m=0.5.

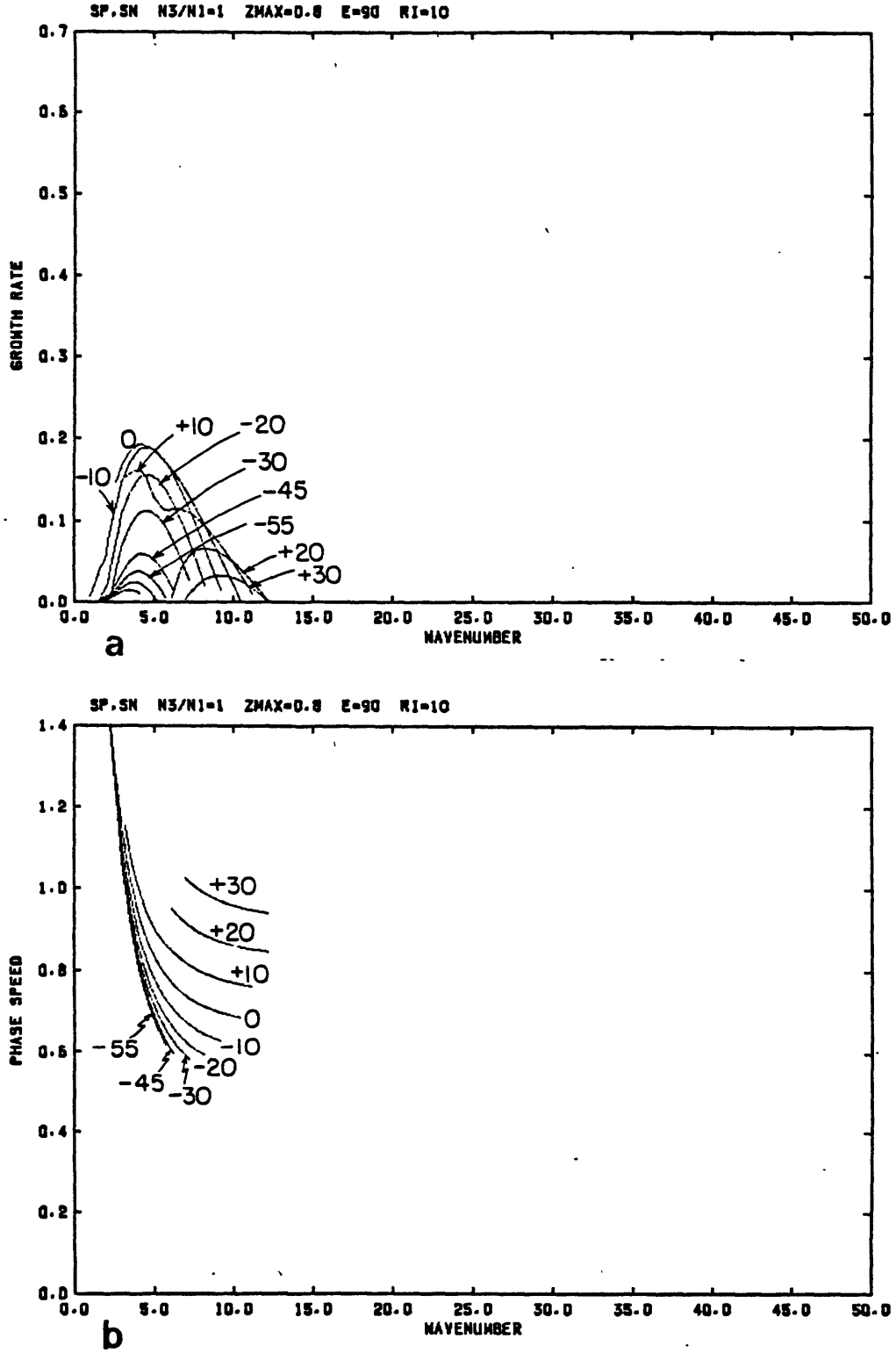

Fig. 4.25: As Fig. 4.11, but for N_s/N_t=1 and z_m=0.8.

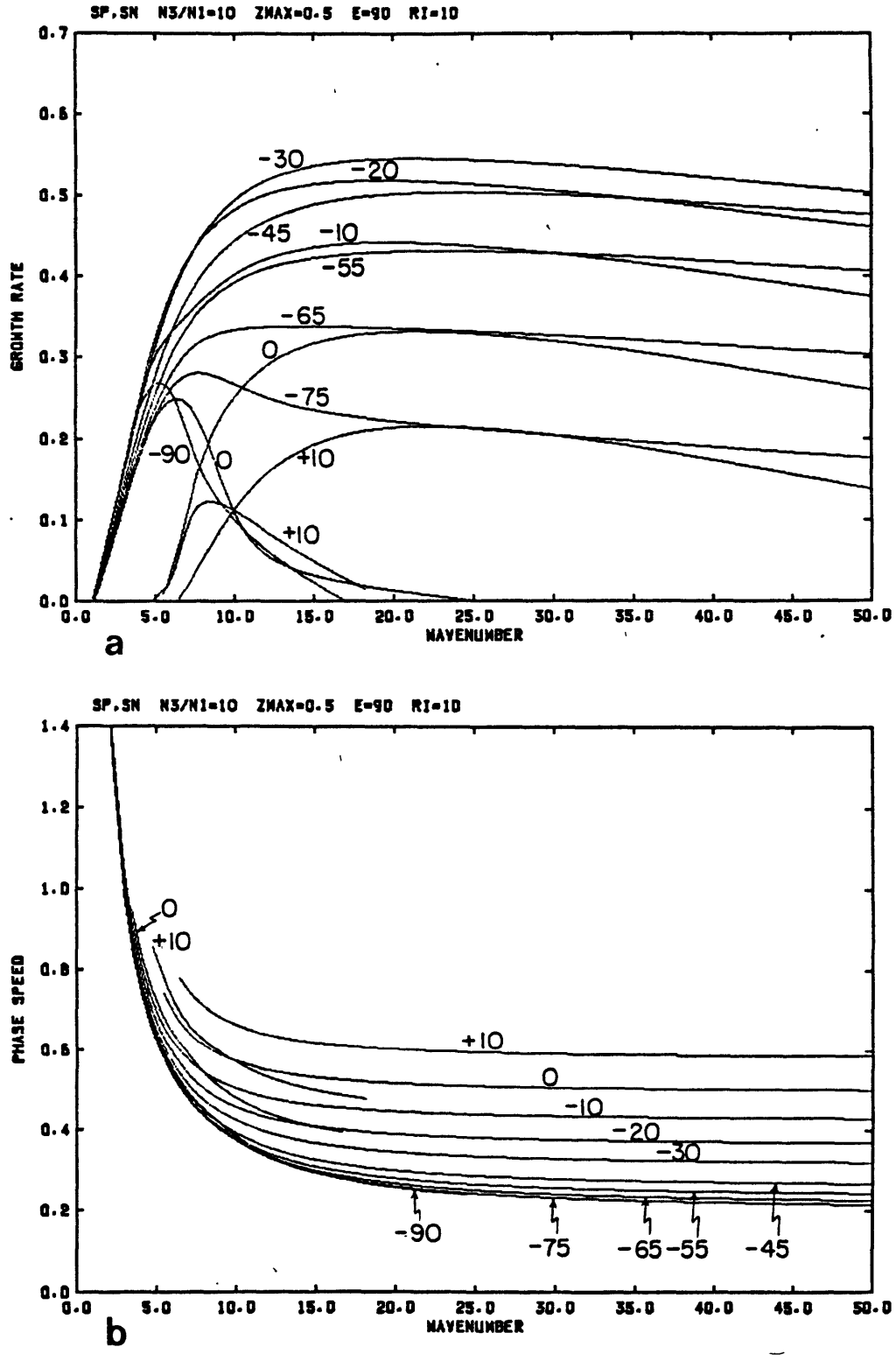

Fig. 4.26: As Fig. 4.11, but for N_s/N_t=10 and z_m=0.5.

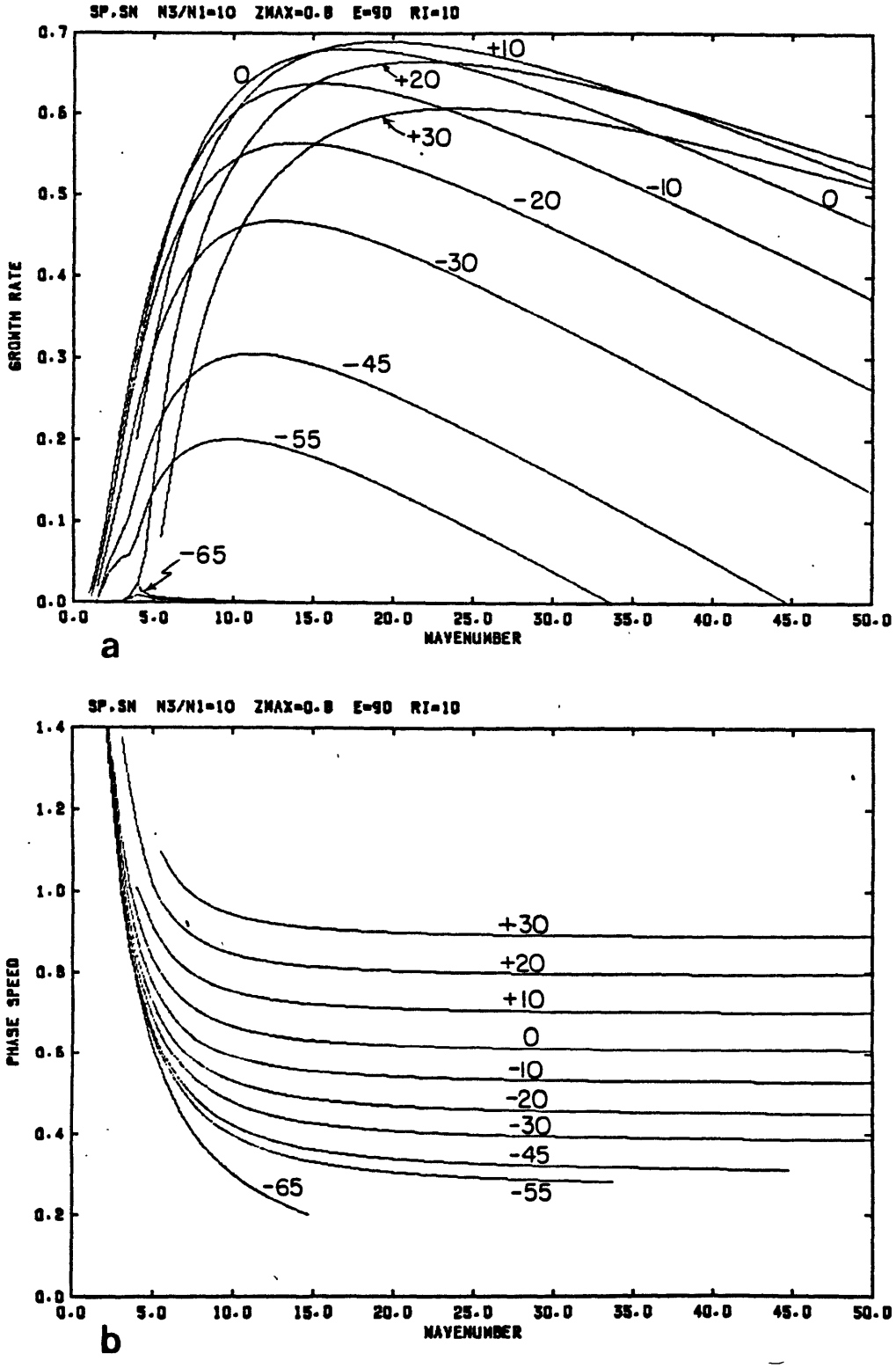

Fig. 4.27: As Fig. 4.11, but for N_s/N_t=10 and z_m=0.8.

rigid lid upper boundary condition, the short wave cutoff is removed and the growth rates approach an asymptotic value for large ℓ (see Fig. 4.28, 4.29). The phase speeds of the wave-CISK mode are not affected by the stratospheric stability. In the case of N_s/N_t=1000, another growing mode exists which propagates toward the cold air. It is shown in Fig. 4.30 and Fig. 4.31 for z_m=0.5, and Fig.4.32 and Fig. 4.33 for z_m=0.8. It also was discussed by Emanuel, for z_m=0.5 and α=0. It is similar to the southward propagating wave-CISK modes in that its largest growth rates occur at orientation angles that correspond to upshear propagation for z_m=0.5 (α=+30°), and downshear propagation for z_m=0.8 (α=-10°). Growth rates are somewhat larger for z_m=0.8. The growth rates are smaller than those of the southward propagating modes, by 38% to 43%. Differences in phase speed between the different angles are due to the Dopppler-shifts. There are no critical levels for these modes at any wavenumber or orientation angles.

For more realistic values of N_s/N_t, only the wave-CISK mode propagating toward the warm air can grow. The characteristics of the fastest growing wave-CISK mode for N_s/N_t values between 1 and 10 are shown in Table 4.2 and Fig. 4.34. The orientation angle of the most unstable mode shows no change for z_m=0.6 and z_m=0.7, a slight decrease for z_m=0.5 as Ns/N_t is increased from 1 to 2, and an increase for z_m=0.8 at N_s/N_t=5. The growth rates show a consistent increase with N_s/N_t, the magnitude of which depends strongly on the heating profile: for z_m=0.5 the growth rate is increased by 47% from N_s/N_t=1 to N_s/N_t=10, while for z_m=0.8 this increase is 259%. This difference in the sensitivity to N_s/N_t is again related to the different importance of the flux of wave energy through the tropopause. The

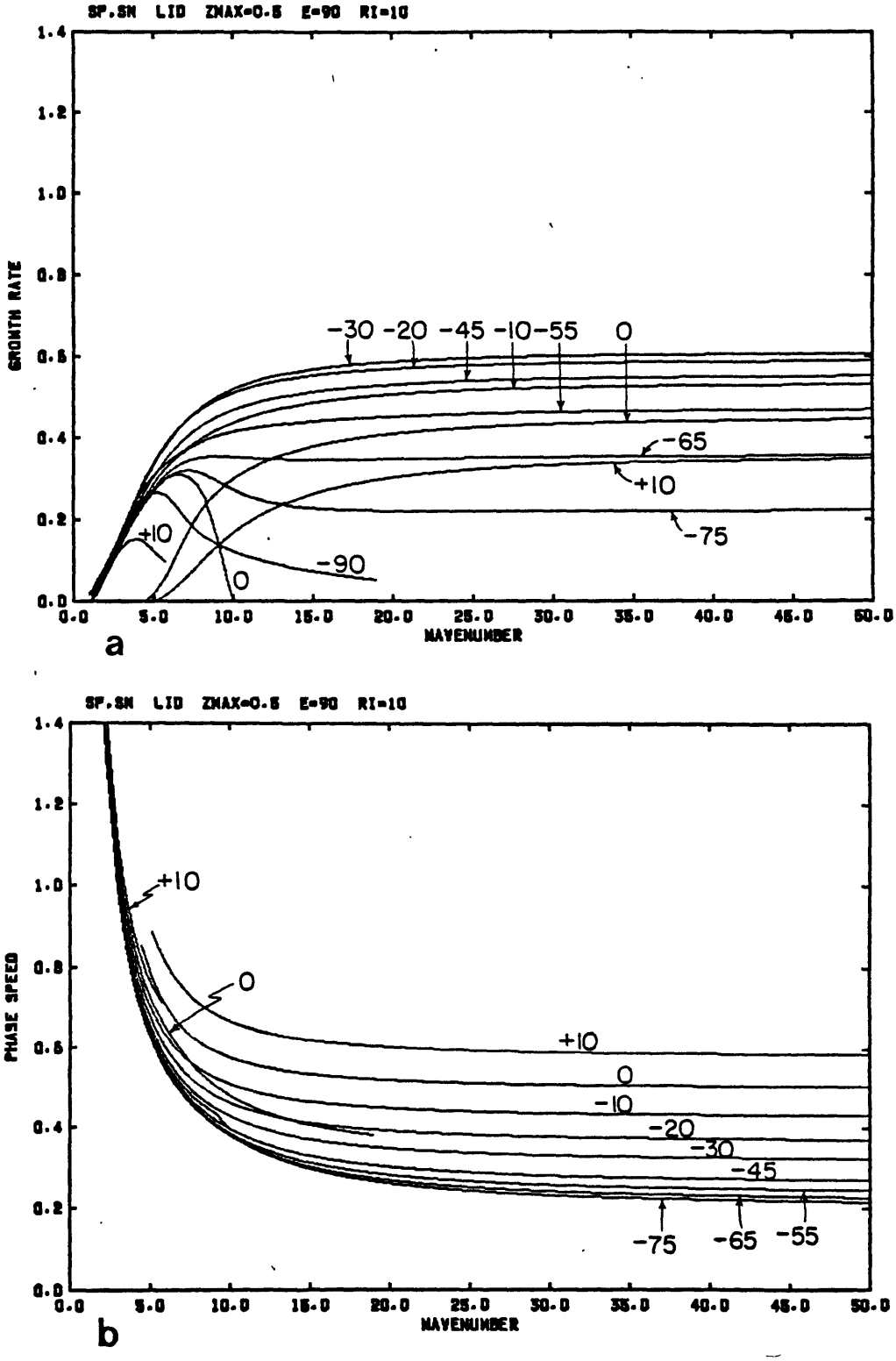

Fig. 4.28: As Fig. 4.11, but for N_s/N_t=1000 and z_m=0.5.

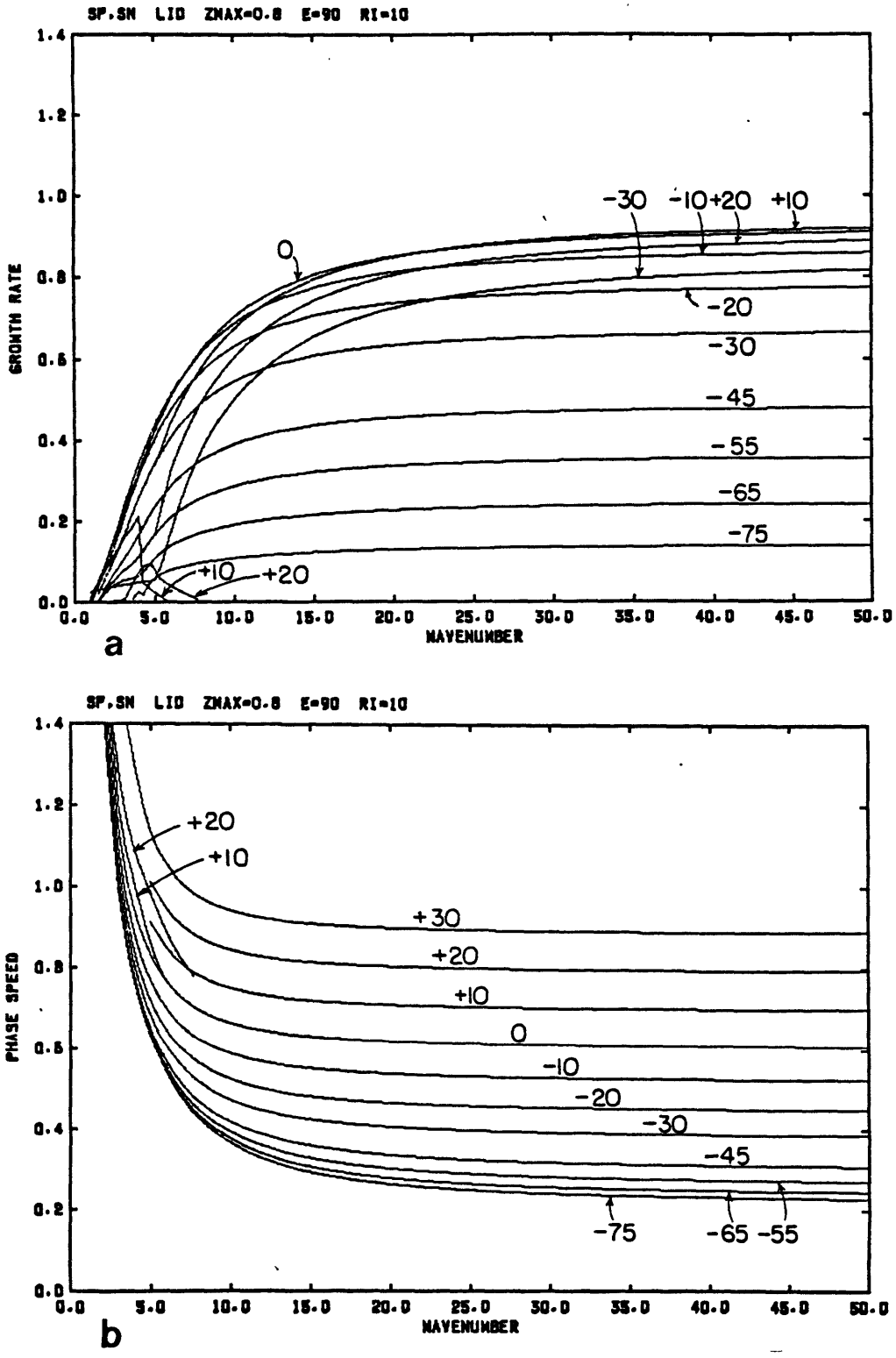

Fig. 4.29: As Fig. 4.11, but for N_s/N_t=1000 and z_m=0.8.

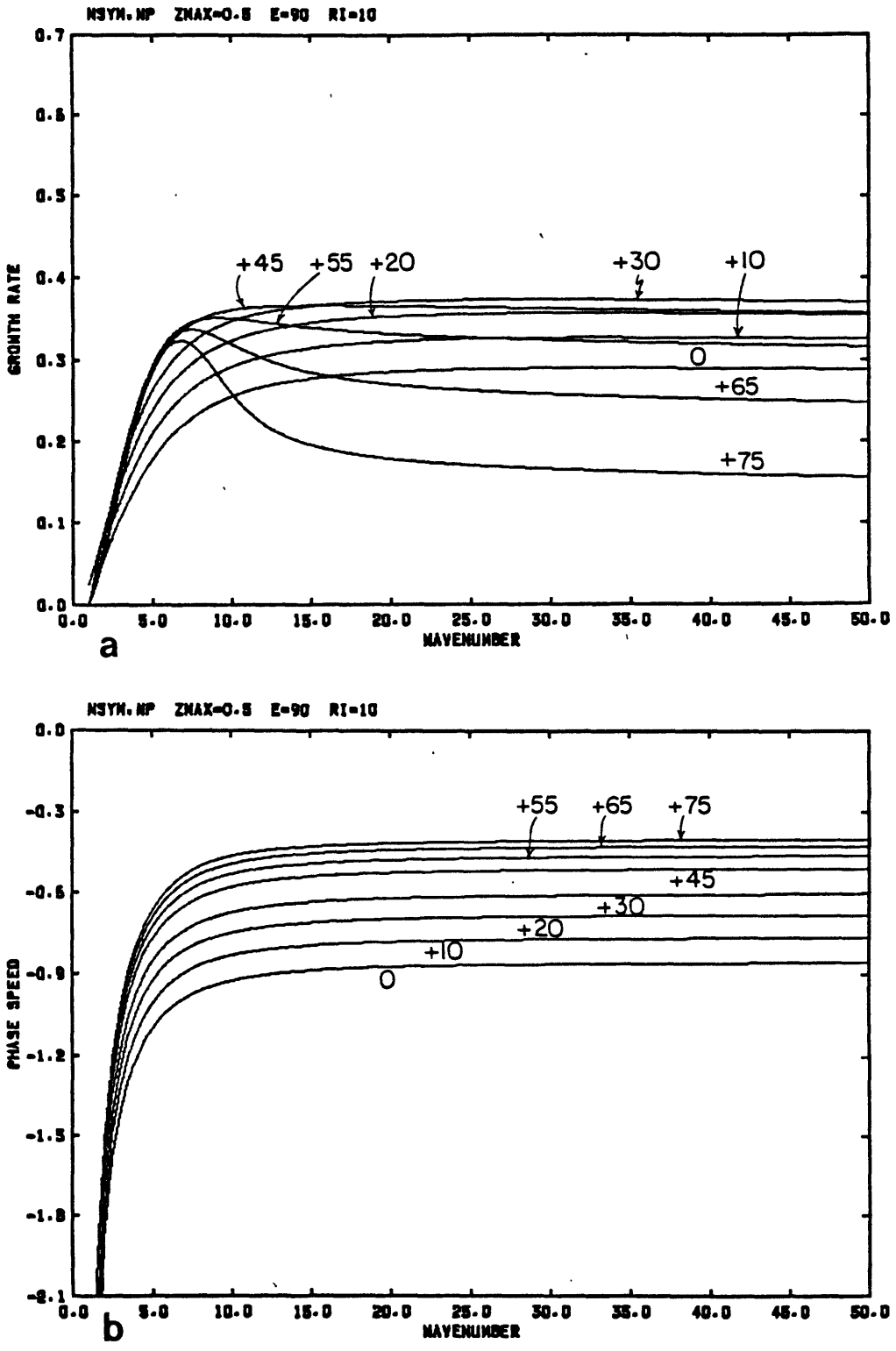

Fig. 4.30: As Fig. 4.11, but for mode N for positive angles, for N_s/N_t=1000 and z_m=0.5.

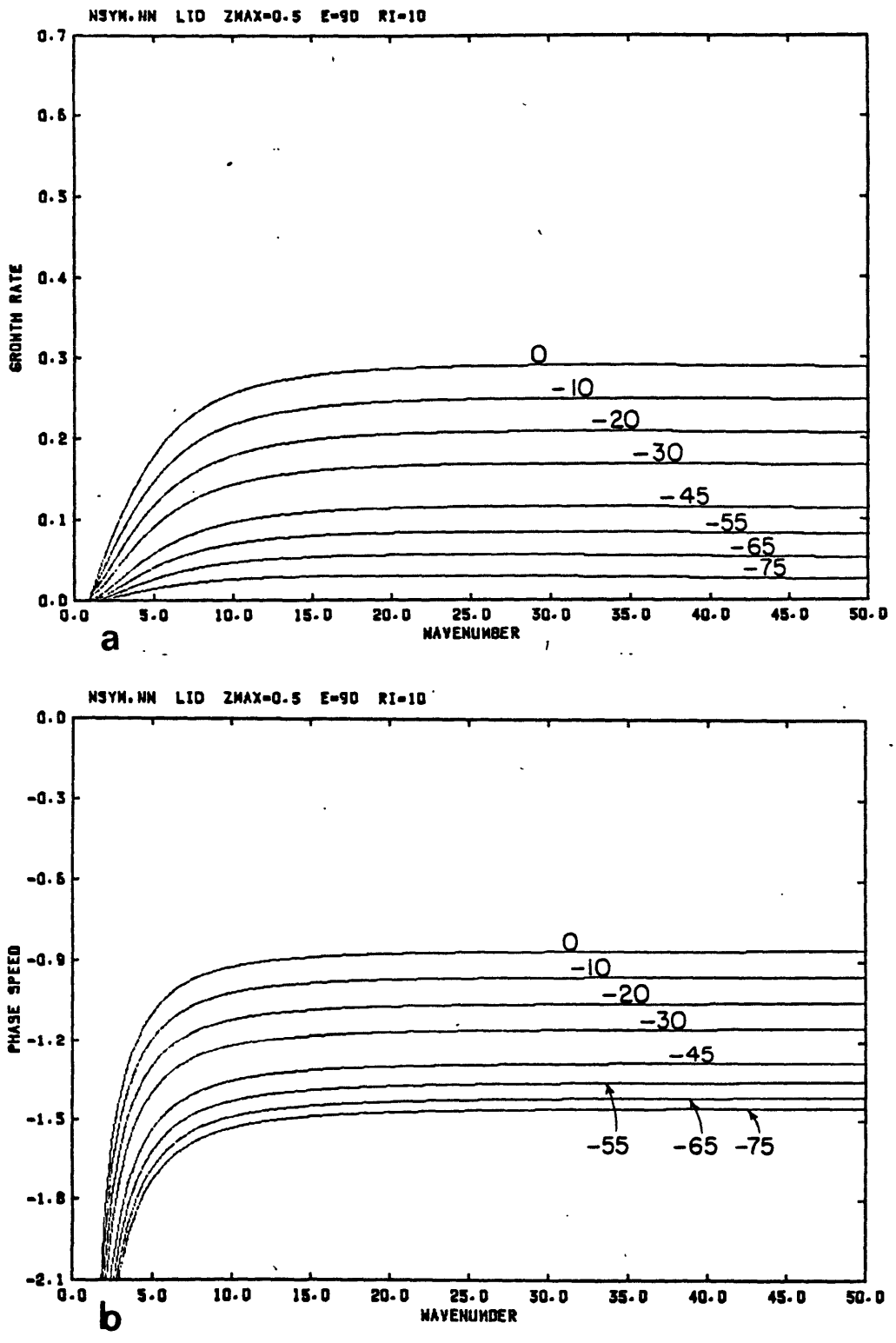

Fig. 4.31: As Fig. 4.11, but for mode N for negative angles, for N_s/N_t=1000 and z_m=0.5.

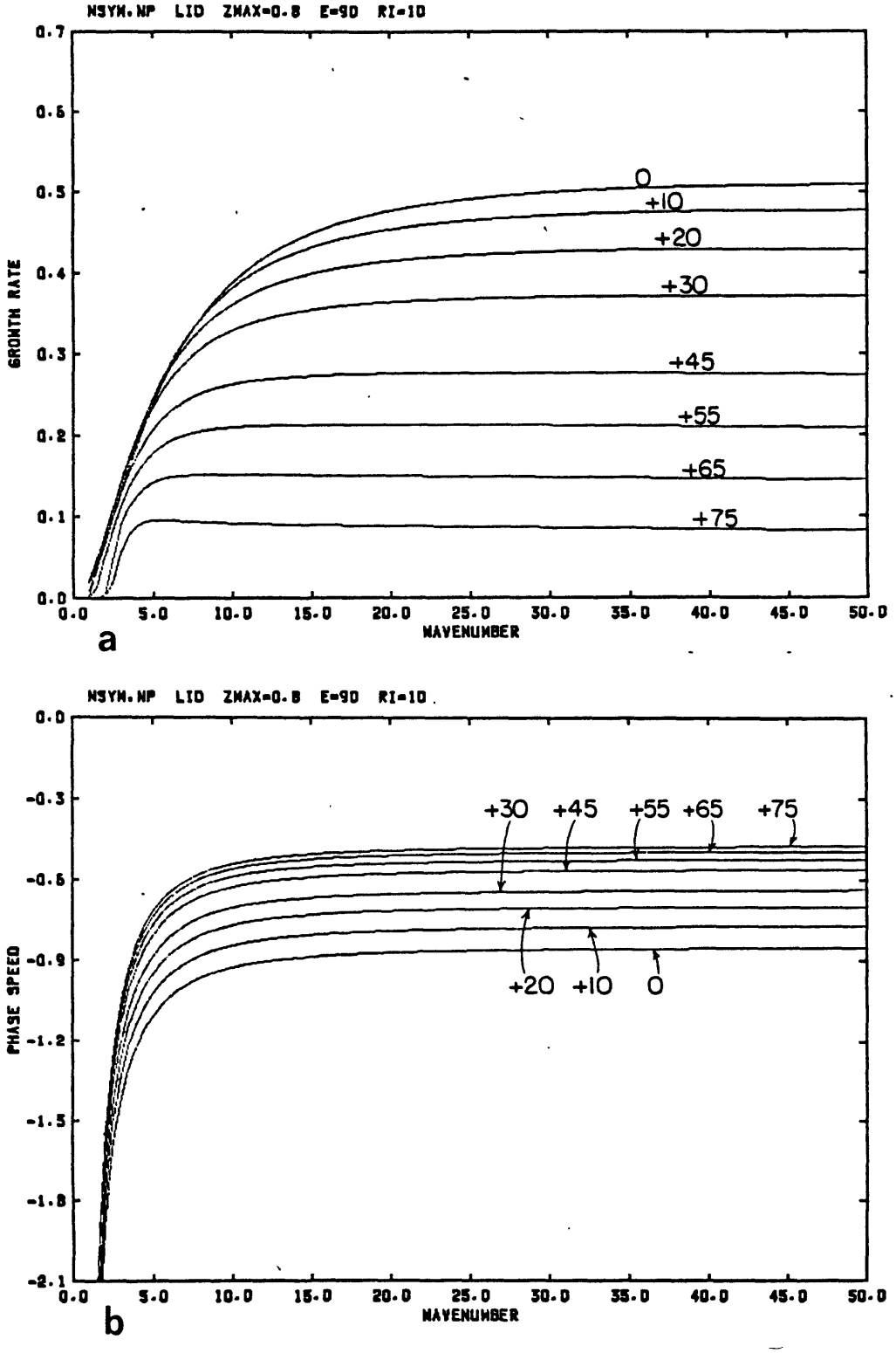

Fig. 4.32: As Fig. 4.11, but for mode N for positive angles, for N_s/N_t=1000 and z_m=0.8.

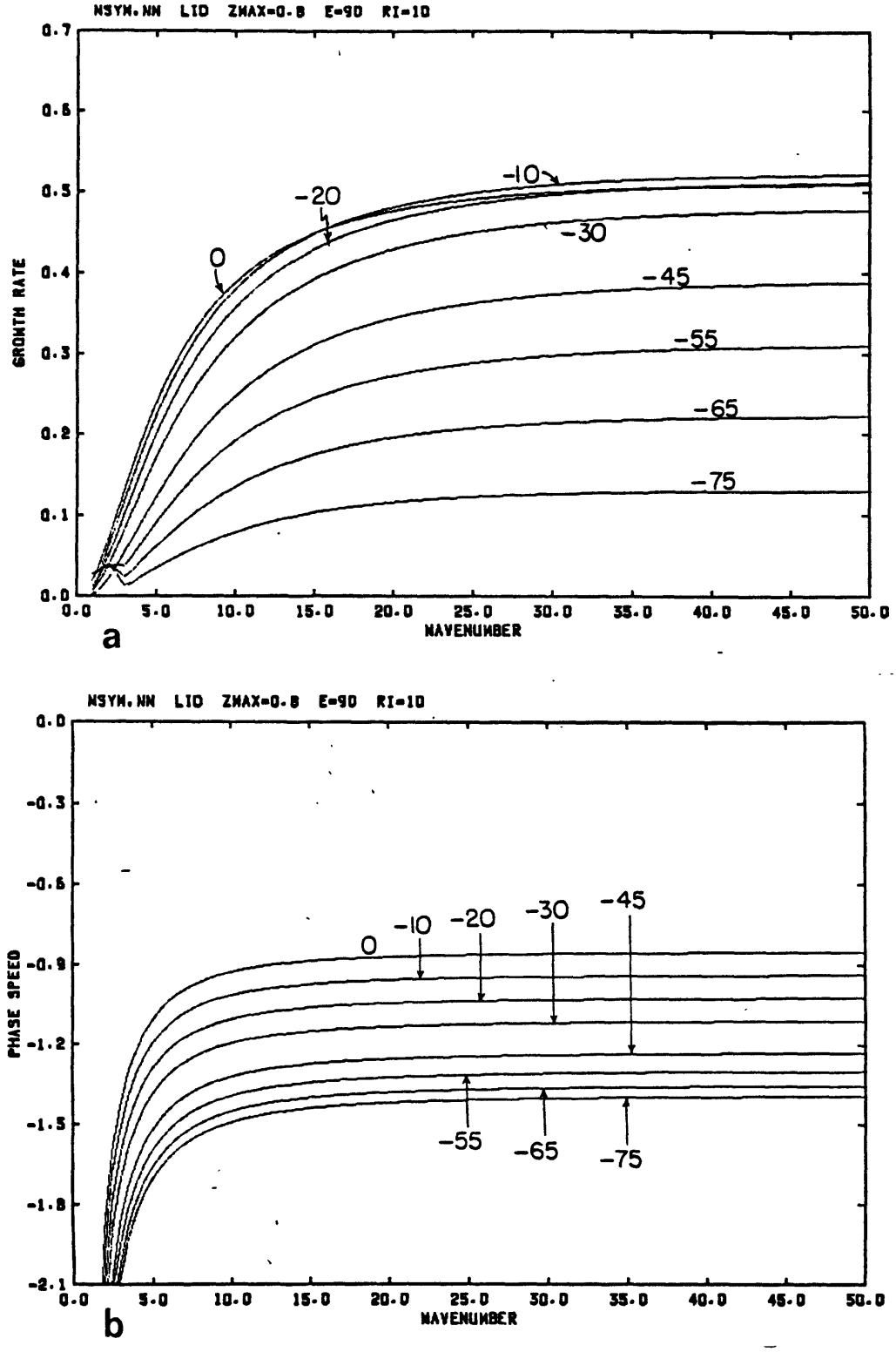

Fig. 4.33: As Fig. 4.11, but for mode N for negative angles, for N_s/N_t=1000 and z_m=0.8.

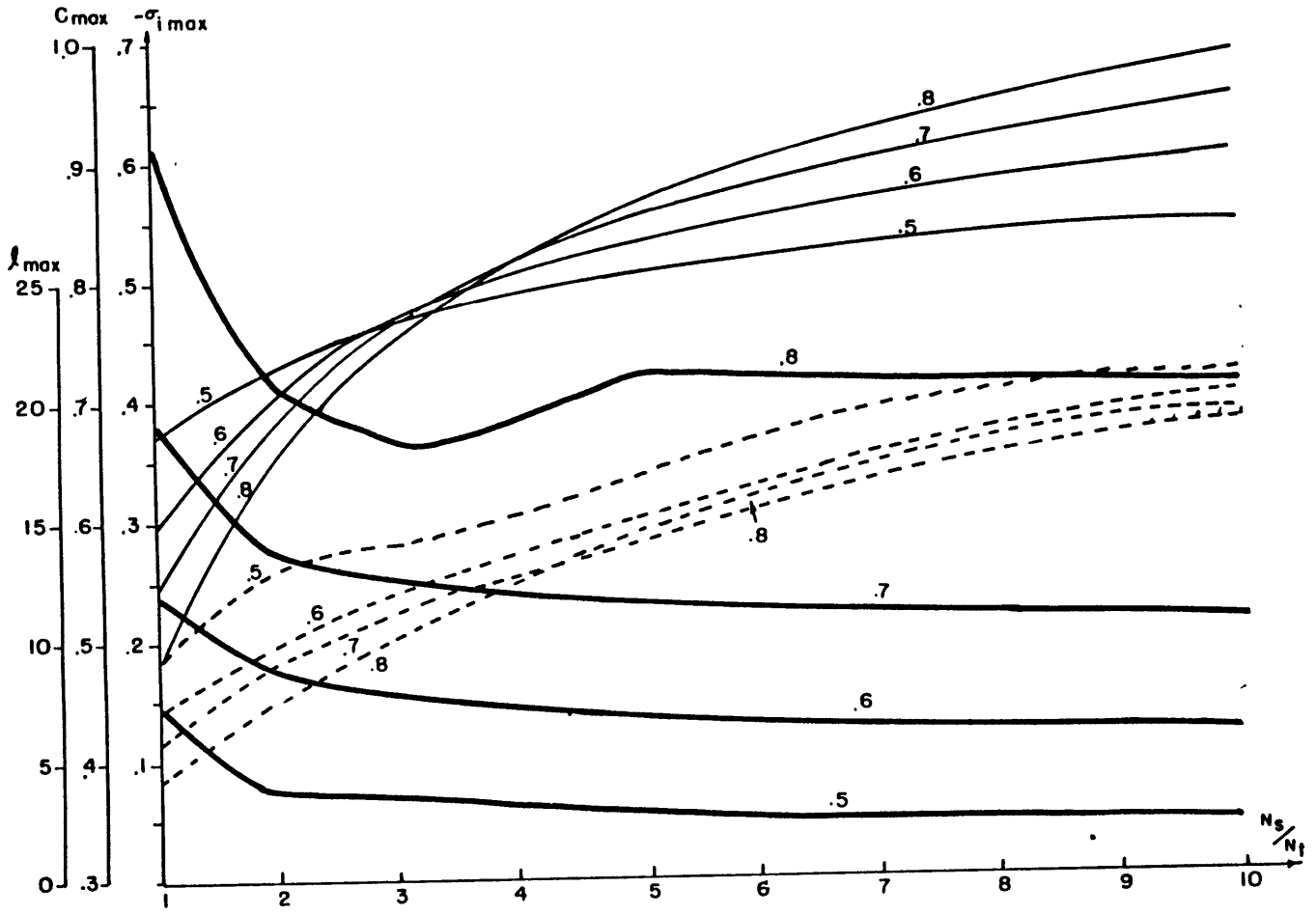

Fig. 4.34: As Fig. 4.23, but for the fastest growing wave-CISK mode as a function of the nondimensional stratospheric Brunt-Väisälä frequency, N_s/N_t.

different growth rate curves cross near $N_s/N_t=3$, which is the reference run parameter value. The wavenumber of maximum growth increases with N_s/N_t, due to the better tolerance for deep disturbance structures for larger stratospheric stabilities. The phase speed of the fastest growing mode is largely determined by the wavenumber behavior, with additional contributions due to the changing Doppler-shifts for $z_m=0.5$ and $z_m=0.8$.

Table 4.2: Orientation angle α of the fastest growing wave-CISK mode as a function of the nondimensional stratospheric Brunt-Väisälä frequency, N_s/N_t.

	N_s/N_t				
z_m	1	2	3	5	10
0.5	-20°	-30°	-30°	-30°	-30°
0.6	-20°	-20°	-20°	-20°	-20°
0.7	-10°	-10°	-10°	-10°	-10°
0.8	0°	0°	0°	+10°	+10°

4.4 Sensitivity to the bulk Richardson number

The Richardson number is the stability parameter of the basic state flow. Its value has a profound influence on dry and moist instabilities:

the dimensional growth rate of the dry Eady mode, for example, is approximately proportional to $Ri^{-1/2}$ (Stone, 1966), implying a constant nondimensional growth rate in the nondimensionalization used here. The wave-CISK mode has been calculated for Richardson numbers ranging from 1.3 to 50, which corresponds to vertical wind shears (for $N_t=10^{-2}$ s^{-1}) of $8.8x10^{-3}$ s^{-1} to $1.4x10^{-3}$ s^{-1}. Growth rate curves for $z_m=0.5$ and $z_m=0.8$ are shown for Ri=1.3 in Fig. 4.35, 4.36 and for Ri=50 in Fig. 4.37, 4.38. Nondimensional growth rates are generally slightly larger for smaller Richardson numbers. Since the nondimensional growth rate and wavenumber are both scaled by $Ri^{-1/2}$, the dimensional growth rate and wavenumber show a larger variation than what is apparent from the figures. Emanuel(1982) found that for $z_m=0.5$ and $\alpha=0$ the long wave mode was much more sensitive to this parameter than the short wave mode. The same holds here for other heating profiles, as well, as is apparent from a comparison of the $\alpha=0$ curves. At other orientation angles, the situation is somewhat more complicated. For all heating profiles and at all orientation angles, the growth rates are strongly decreased with increasing Ri at small ℓ; however, growth rates are also decreased at large ℓ for increased Ri, more so for $z_m=0.5$ and $z_m=0.8$ than for $z_m=0.6$ or $z_m=0.7$ (not shown here). Another effect of the larger shear values at smaller Ri is the increased selectivity with respect to the orientation angle. At Ri=1.3, the growth rates are essentially zero for orientation angles beyond the narrow range shown in Fig.4.35 and 4.36, while at larger Ri growing solutions exist for a wider range of orientation angles.

The phase speed curves show some variation with Ri as well. For small Ri the phase speed is more nearly constant at large ℓ, i.e. the

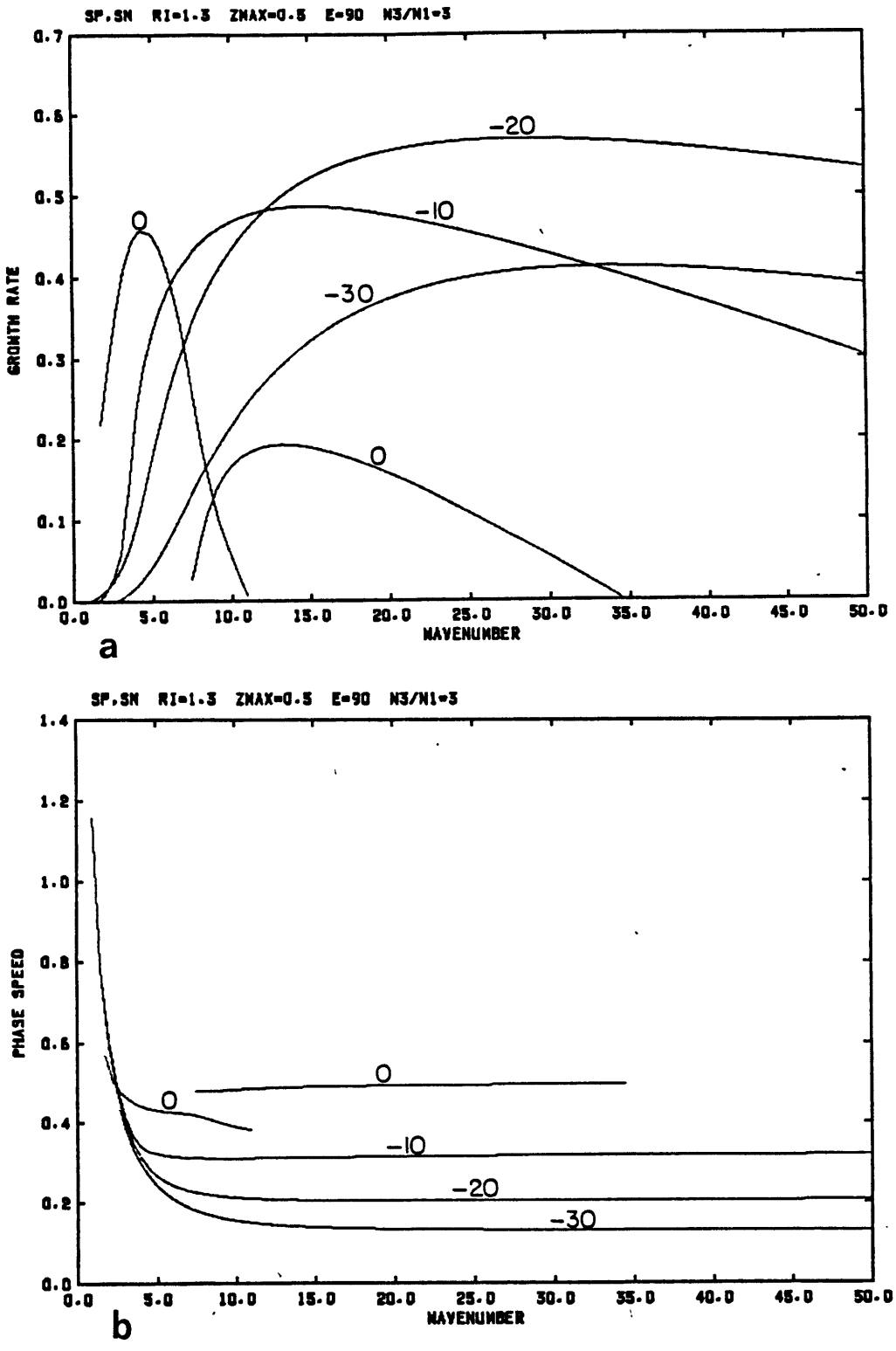

Fig. 4.35: As Fig.4.11, but for Ri=1.3 and z_m=0.5

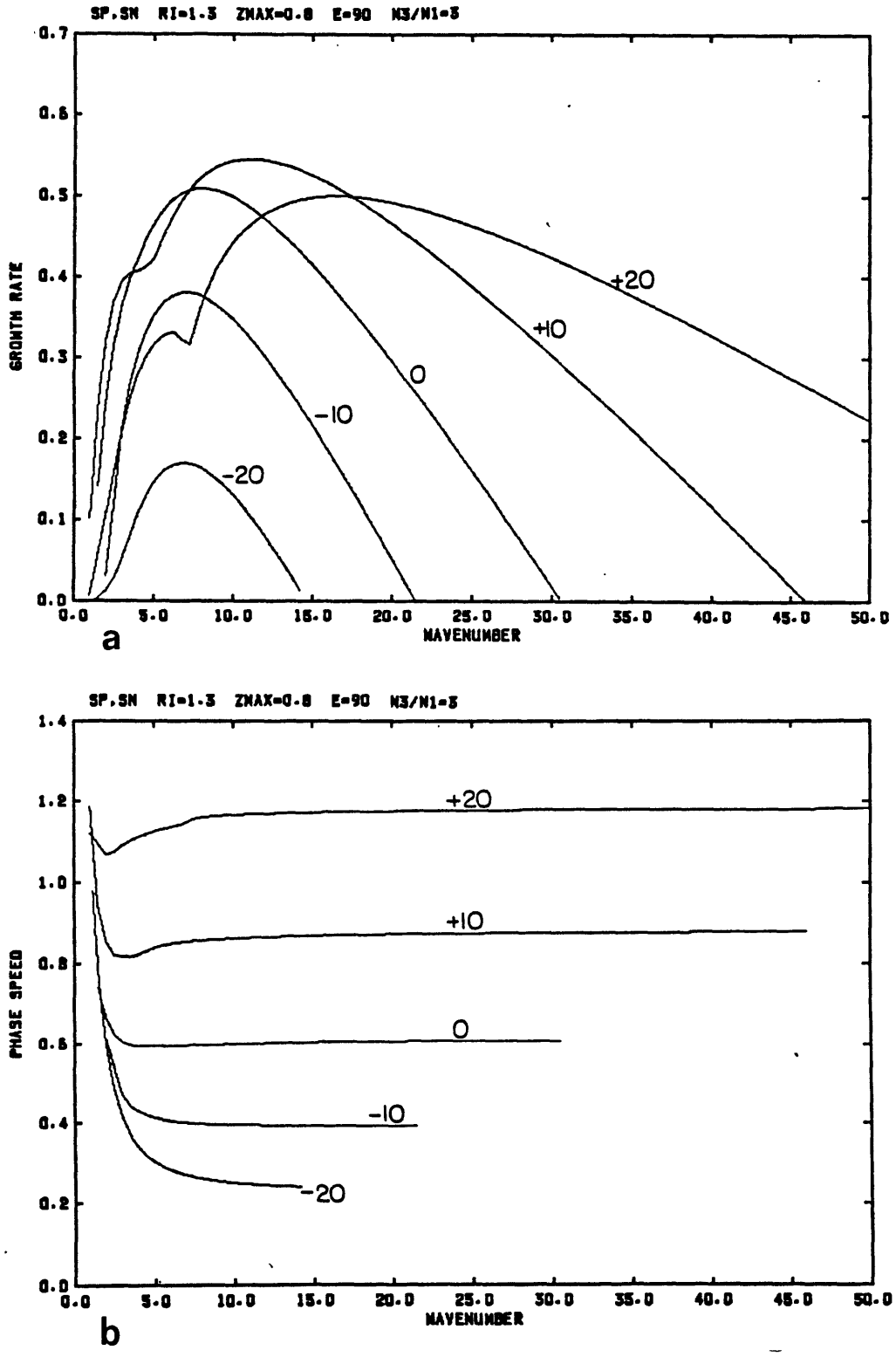

Fig. 4.36: As Fig.4.11, but for Ri=1.3 and z_m=0.8

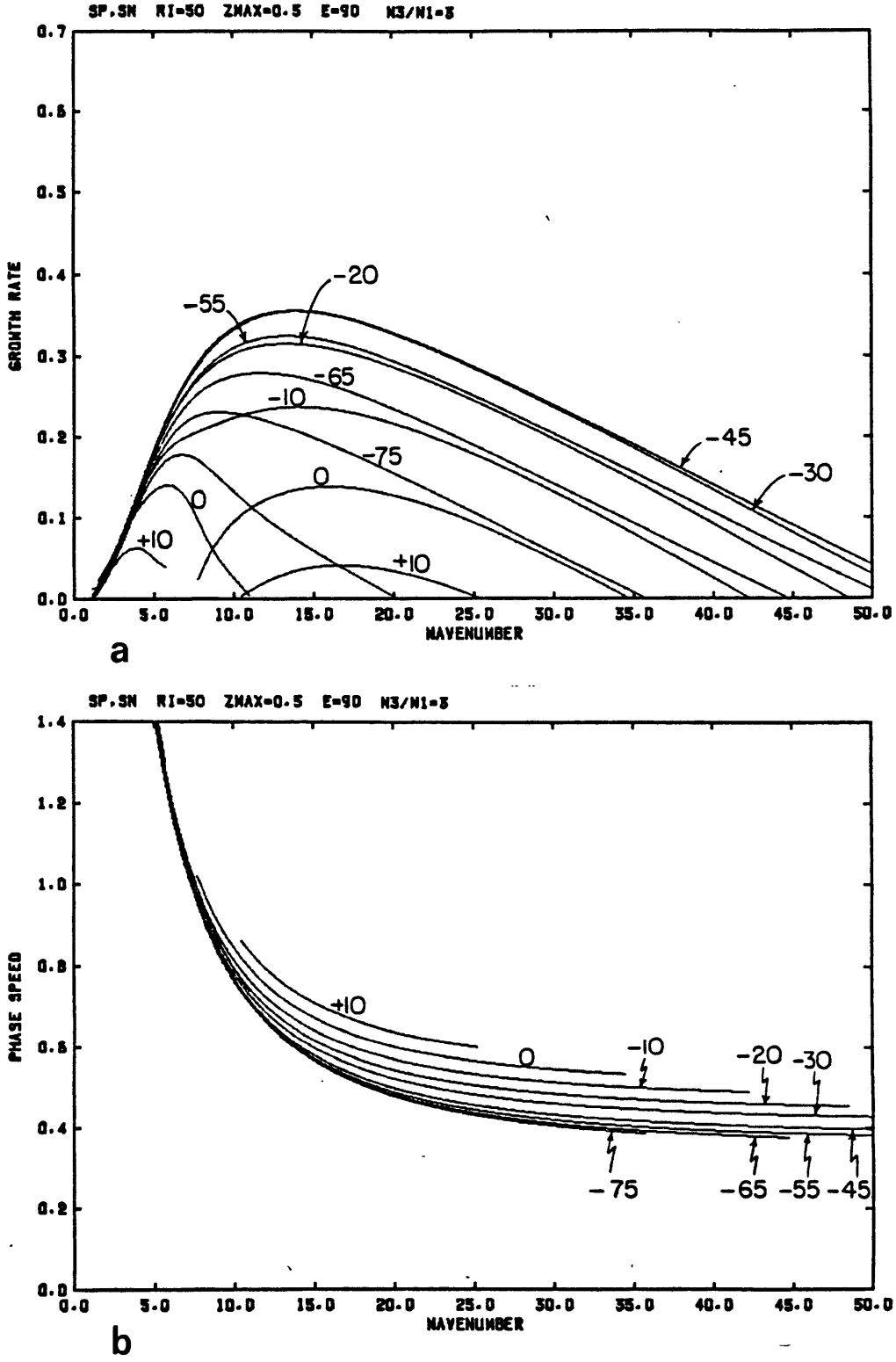

Fig. 4.37: As Fig.4.11, but for Ri=50 and z_m=0.5

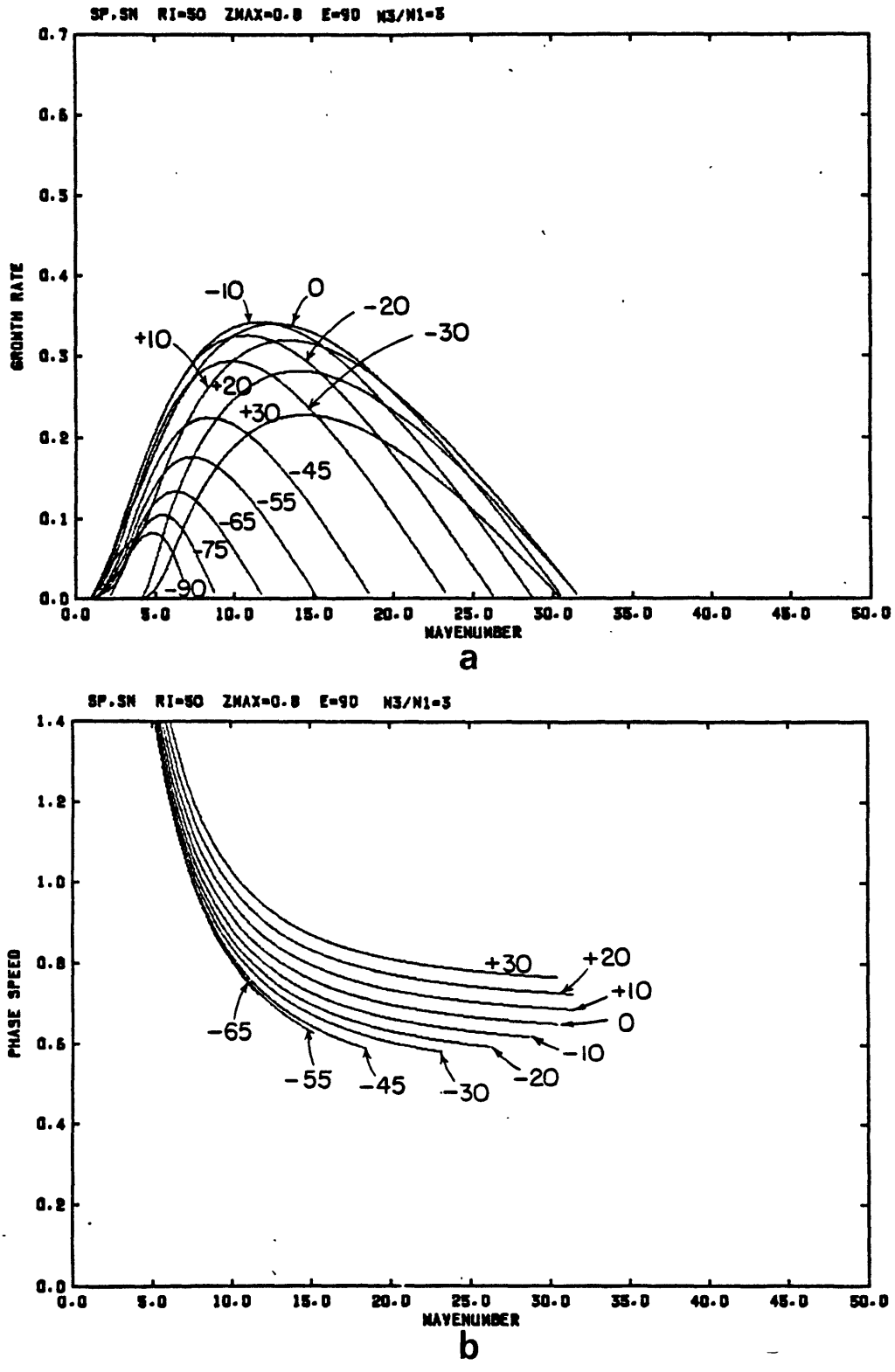

Fig. 4.38: As Fig.4.11, but for Ri=50 and z_m=0.8

waves are less dispersive, than at large Ri. The asymptotic value of c is unchanged at $\alpha=0$, since the gravity wave phase speed does not depend on the Richardson number, and the Richardson number does not appear in the scaling of the phase speed. The differences between different orientation angles are larger for smaller Ri, reflecting the increased values of the cross-line shear. At small wavenumbers the dimensional frequency approaches f for all Ri, which manifests itself as an increase of c with Ri in this nondimensionalization. There are again no critical levels, except at Ri=1.3 for $z_m=0.7$ and $z_m=0.8$ at $\alpha>0$, where the Doppler-shifted frequency is equal to f at a level in the domain for wavenumbers below 5.

Other modes exist at Ri=1.3 at negative orientation angles which propagate toward the cold air. These modes (not shown here) have growth rates of comparable magnitude to the symmetric modes at Ri=1.3, but they become essentially neutral for moderate Richardson numbers (Ri>5). These modes have a steering level and a +f singularity in the troposphere. For large wavenumbers and/or moderate Richardson numbers all the energy transformations are concentrated in such a shallow layer at the height of the singularities that the vertical resolution of the numerical method becomes insufficient to correctly calculate the eigenvalues of these modes. Their relevance to physical processes in the atmosphere is unclear, but their direction of propagation and their dependence on very large shears make them an unlikely candidate for an explanation of squall lines. Other low Richardson number modes, without heating, are discussed in Appendix B.

The characteristics of the most unstable wave-CISK mode that also exists at larger Ri are displayed in Fig. 4.39 and Table 4.3. The

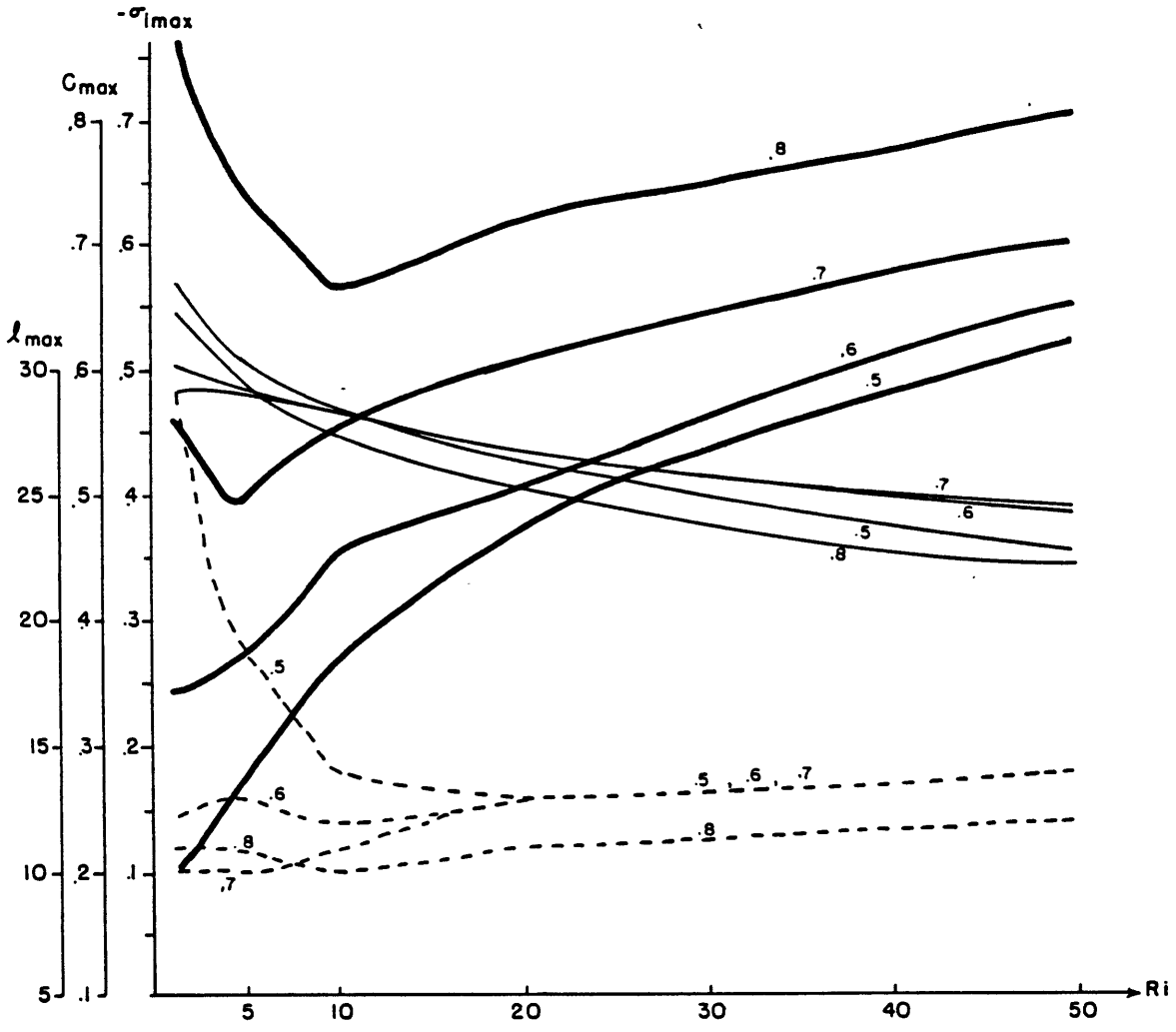

Fig. 4.39: As Fig.4.23, but for the fastest growing wave-CISK mode as a function of the bulk Richardson number, Ri.

nondimensional maximum growth rates are decreased slightly (by not more than 37%) over the whole range of Richardson numbers; the decrease is markedly larger for z_m=0.5 and z_m=0.8 than for z_m=0.6 and z_m=0.7. This is a result of the aforementioned difference in the sensitivity to Ri at large ℓ. Since the Richardson number enters the nondimensionalization, this slight decrease corresponds to a much larger (approximately 90%) decrease of the dimensional growth rate. Thus the growth rate is correctly scaled (from eq.(3.9)) by $Ri^{-1/2}$, i.e. by the value of the environmental shear. The nondimensional wavenumber of fastest growth shows even less variation with Ri, with the exception of a sharp increase from Ri=10 to Ri=1.3 for z_m=0.5. Thus the dimensional wavenumber of the most unstable mode is also approximately proportional to the value of the environmental wind shear. The increase of ℓ_{max} at low Ri for z_m=0.5 is a result of the fact that the heating amplitude is near the critical value (with respect to to the short wave cutoff) for that heating profile, so that any destabilization, such as a reduction in Ri, leads to a strong growth rate increase at large ℓ. The orientation angle tends to decrease as the Richardson number is increased. The phase speed increases with Ri as a result of generally increased phase speeds at low wavenumbers and, for z_m<0.8, smaller Doppler-shifts for nonzero α. The smaller Doppler-shift is responsible for the decrease in c for z_m=0.8 from Ri=1.3 to Ri=5, and a decreased α leads to decreases in c_{max} for

z_m=0.8 from Ri=5 to Ri=10, and for z_m=0.7 from Ri=1.3 to Ri=5.

Table 4.3: Orientation angle α of the fastest growing wave-CISK mode as a function of the bulk Richardson number, Ri.

	Ri				
z_m	1.3	5	10	20	50
0.5	-20°	-30°	-30°	-30°	-30°
0.6	-10°	-20°	-20°	-30°	-30°
0.7	0°	-10°	-10°	-10°	-20°
0.8	+10°	+10°	0°	0°	-10°

The relatively small variation of the nondimensional wavenumber of maximum growth makes it possible to make some general observations. The dimensional wavelength is related to the nondimensional wavenumber through eq.(3.9):

$$L^* = 2\pi/\ell^* = 2DRi^{1/2}/\ell \ ,$$

where D is the Rossby deformation radius $D=HN_t/f$, and ℓ is o(10) for the fastest growing wave-CISK mode. The aspect ratio of the most unstable mode is given by

$$\delta = 2H/L^* = \ell Ri^{-1/2}H/D = o(10^{-1})Ri^{-1/2} \ ,$$

and it is small compared to 1, thus validating the hydrostatic assumption. The aspect ratio, which is also a measure of the slope of the streamlines, is o(10) times larger than the slope of the isentropes ($Ri^{-1/2}f/N$). The wave-CISK modes thus satisfy the restrictions imposed by the density discontinuity at the tropopause (see section 3.2).

4.5 The effects of low level cooling

The heating profiles considered thus far are positive throughout the domain, implying that only net heating takes place in a vertical column where convection is occuring. In the presence of falling precipitation and evaporatively driven downdrafts it is possible for net evaporation to take place near and below cloud base. To account for these effects in this model, a modified heating profile G'(z) is defined as

$$G'(z) = G(z) - G_d(z),$$

where G(z) is given by (3.19) and $G_d(z)$ represents the effects of evaporative cooling. For the sake of convenience I assume the following functional form for $G_d(z)$:

$$G_d(z) = \begin{cases} D(\exp(z_i - z) - 1) & \text{for } z < z_i \\ 0 & \text{for } z > z_i \end{cases},$$

where $z_i = 2(z_m - 0.5)$, and D is a measure of the cooling magnitude. The level z_i, the inflection point of the unaltered heating profile, was chosen to ensure a smooth profile. As was mentioned in section 4.1, the

heating amplitude of the reference run corresponds to a large precipitation efficiency for the heating profiles without cooling; the same maximum heating amplitude corresponds to a smaller precipitation efficiency if low level cooling is included, which decreases the vertically integrated heating. If we denote the fractional decrease of precipitation efficiency due to the low level cooling, at an equal maximum heating rate, by β, the constant D can then be expressed as

$$D = \frac{2\beta}{\pi(\exp(z_i) - z_i - 1)} \quad .$$

Fig. 4.40 shows the modified heating profiles for z_m=0.8, and β=0, 1/6, 1/3. If β=0 corresponds to E=90%, an equal heating rate maximum corresponds to E=75% (60%) for β=1/6 (1/3). Calculations have been carried out for these heating profiles, and all other parameters as in the reference run. The contour plot of the growth rate in the wavenumber plane (Fig. 4.41) shows a shift of the growth rate maximum toward more positive angles and larger wavenumbers for increased low level cooling. The orientation angle of the most unstable mode is +10° for β=1/6, and +20° for β=1/3. Growth rates are increased at large wavenumbers, but the maximum growth rate is approximately constant from β=0 to β=1/3. The phase speeds (not shown) are increased slightly by low level cooling.

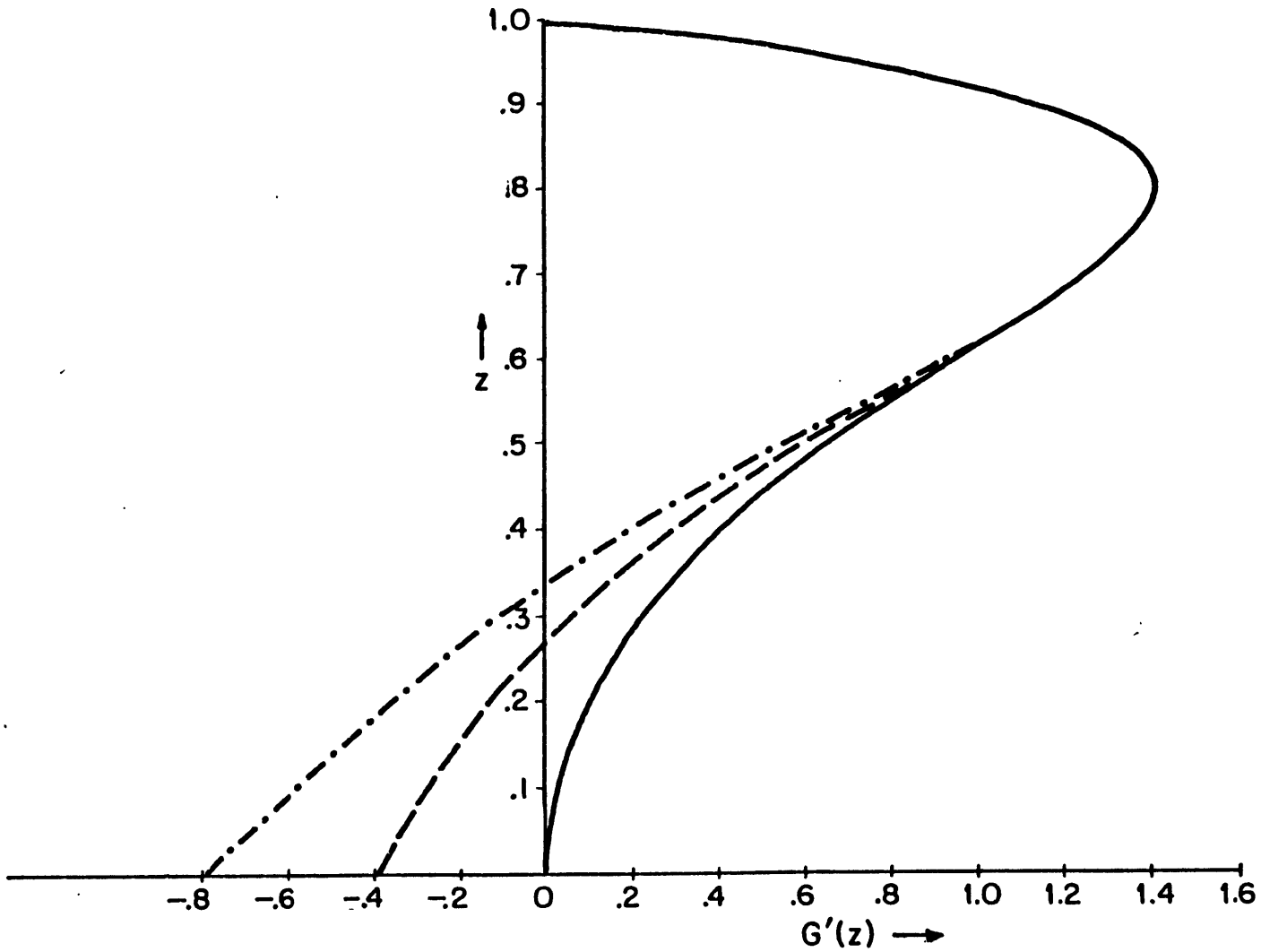

Fig. 4.40: The heating profile, as modified by downdraft cooling, for z_m=0.8 and β=0 (solid line), β=1/6 (dashed line), and β=1/3 (dash-dotted line).

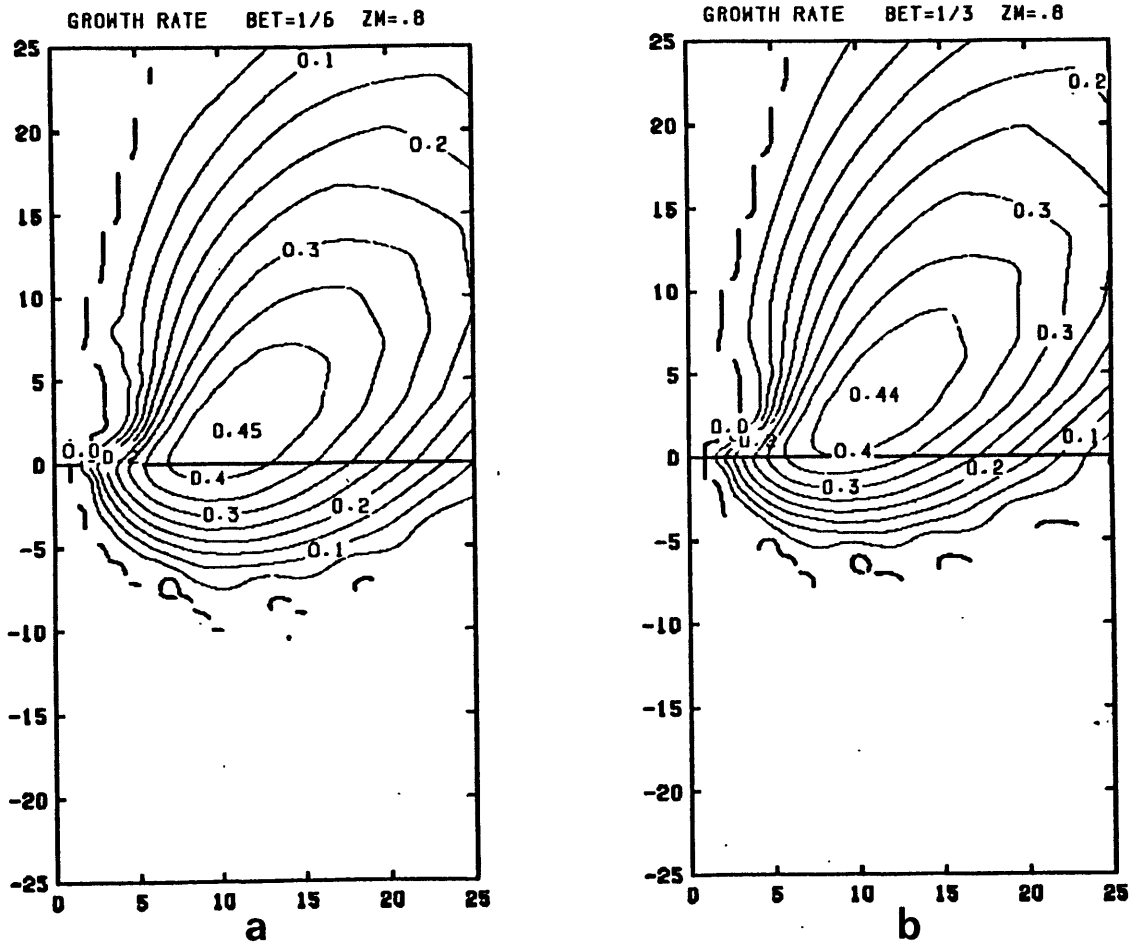

Fig. 4.41: Contour plot of growth rate for case of downdraft cooling; a): E=75%, β=1/6, b): E=60%, β=1/3. Plotting conventions same as in Fig. 4.1.

4.6 Summary of results

For representative values of the model parameters, two growing modes exist in the model. At small wavenumbers baroclinic instability (Eady) modes, modified by heating, have the largest growth rates. Wave-CISK modes are the fastest growing modes at larger wavenumbers, with orientation angles near the symmetric axis. Other growing modes exist only for extreme values of the Richardson number or the stratospheric static stability.

The Eady mode has its largest growth rate along the baroclinic axis, with dimensional[2] values of wavelength and e-folding time on the order of 3600 km and 26 hours, respectively. Its growth rate is only slightly higher than that of the adiabatic instability, and it is largest for a sinusoidal vertical heating profile (z_m=0.5).

The wave-CISK mode is the continuation to general orientation angles of the wave-CISK mode along the symmetric axis found by Emanuel (1982). The largest growth rate occurs near, but in general not on, the symmetric axis. The wavelength of fastest growth is on the mesoscale, with dimensional values (for the reference run) between 630 km and 450 km, and corresponding e-folding times on the order of 20 hours. The orientation angle is sensitive to the form of the vertical heating profile: disturbances are rotated clockwise by 30° from the direction of the environmental shear for a sinusoidal heating profile (z_m=0.5), and only by 20° (10°) for z_m=0.6 (z_m=0.7). These modes are propagating

2) For model parameters as in the reference run, and basic state parameters as in section 4.1.1.

upshear, and toward the warm air. For z_m=0.8, corresponding to a heating profile with a maximum in the upper troposphere, the fastest growing disturbance is aligned with the environmental shear. The value of the largest growth rate is not very sensitive to the form of the heating profile, however. The phase speed identifies the wave-CISK mode as a modified inertio-gravity wave. At small wavenumbers the dimensional frequency approaches the Coriolis parameter, and at large wavenumbers the phase speed asymptotically approaches that of a mode 2 gravity wave.

The vertical structure of the wave-CISK mode resembles that of a trapped, neutral gravity wave in the lower part of the domain. The upper part is characterized by streamlines that slope back toward the cold air. The generation of eddy available potential energy by convective heating is the single most important energy source for the wave-CISK mode. This energy generation, which is proportional to the correlation of heating and buoyancy, is positive in the upper part of the disturbance, and negative below. A larger wavenumber ℓ and a higher level of maximum heating z_m both lead to a deeper disturbance in the sense that the trapped gravity wave occupies a larger part of the domain, and that the perturbation amplitude at upper levels is increased. A heating profile with a large z_m, which more strongly weights energy generation in the upper troposphere, thus favors larger wavenumbers at equal orientation angles. A cross-line shear against the direction of propagation leads to a shallower disturbance; correspondingly, fastest growth for small z_m occurs at negative orientation angles α, and at less negative or zero α for larger z_m. For small z_m, the energy budget of the most unstable mode shows the heating generation of energy and mean flow interactions to be more important, and energy loss to the stratosphere to be less important than for the most unstable mode at larger z_m.

Sensitivity experiments of the wave-CISK mode were performed for different values of the heating rate (E), stratospheric static stability (N_s/N_t), and the Richardson number (Ri). For precipitation effiencies below 100% the maximum growth rate occurs at a finite wavenumber, which decreases as E is decreased. The growth rate strongly depends on E, and it essentially becomes zero for E below 30%. The angle of orientation does not vary much with E for small z_m, but for z_m=0.8 it changes from -20° (E=30%) to +20° (E=105%). Phase speeds are increased only slightly by larger heating rates, but the phase speed of the most unstable mode shows more of a variation as a result of changes in the wavenumber and orientation angle.

Changes in the stratospheric static stability lead to changes in the growth rates, especially at large ℓ and for large z_m. The short wave cutoff is removed for very large N_s/N_t. Growth rates are generally increased by an increase in N_s/N_t, while the phase speeds remain unchanged. The largest growth rate occurs at shorter wavelengths for larger N_s/N_t. The orientation angle is not very sensitive to N_s/N_t.

Variations of the Richardson number show a small decrease of the nondimensional growth rate for an increase of Ri, which corresponds to a much larger decline in the dimensional growth rate. The nondimensional wavenumber of fastest growth is essentially constant with respect to the Richardson number. The dimensional wavenumber and growth rate of the fastest growing mode are thus both approximately proportional to the value of the environmental shear (from (3.9)). Orientation angles tend to be more negative for smaller Richardson numbers.

Calculations for a modified heating profile that includes low level cooling (and thus implies smaller precipitation efficiencies for equal heating rate maxima) show a shift of the growth rate maximum to larger wavenumbers and positive orientation angles, with little change in the growth rate value.

5. Comparison with observations

The results described in the previous chapter possess certain characteristics which may be compared to observations of squall lines in the atmosphere. The vertical structure of the streamfunction and other perturbation variables should agree with cross sections of the numerous squall line case studies reported in the literature, if the wave-CISK theory is to be applicable to squall lines in the atmosphere. As will be shown in the next section, the gross features of the circulation do indeed compare favorably. Because of considerable uncertainties in the observations and relatively large variations of the predicted disturbance structures with model parameters, this agreement cannot be regarded as conclusive evidence.

The other aspects of the solutions present more of a problem. The growth rates, with e-folding times on the order of 20 hours, are certainly insufficient to account for the rapid intensification of squall lines; even so, the theory could still be useful for explaining the maintenance of the squall lines, once they are formed. The formation could then be thought of as a separate process, forced by mechanisms such as orographic forcing or the interaction of storm outflow boundaries. This scenario was proposed by Raymond (1984). If one interprets observed widths of squall lines, which are generally no larger than 100 km, as half-wavelengths, the wavelengths should be on the order of 200 km or less, about half or one-third of what is predicted by the model. One could argue that this discrepancy is due to the use of the duty-cycle approximation, which spreads the effects of the convection over a large portion of the wave. Allowing heating only for positive $w(z_o)$ would most likely result in a more concentrated updraft.

Finally, the predicted angle of orientation and the predicted phase speed provide the strictest test of the theoretical results. In the last section of this chapter, two independent observational studies are used to determine observed orientation angles and phase speeds. Calculations are then performed to reproduce these findings in the model by adjusting model parameters until the orientation angle of the fastest growing mode, which is the most sensitive and thus the most adjustable result, is predicted correctly; the phase speed of this fastest growing mode is then fixed by the previous choice of parameters and can be compared with observed values. As will be shown, the predicted phase speeds are 2-5 times larger than is observed, thus clearly establishing that the predictions from this model do not agree with the observations. The implications of this finding will be discussed in the next chapter.

5.1 The vertical structure of the perturbations

There is one feature common to all squall lines, be they tropical or midlatitude, frontal or prefrontal, and that is the existence of a mesoscale updraft which slopes backward with height. The solutions presented in the previous chapter all exhibit this circulation feature, although there is considerable variation in the details of the streamfunction profiles.

Cross sections through observed squall lines, as found in Newton (1950), Ogura and Liou (1980), and Bradberry (1981), consistently show a strong buoyancy deficit below and behind the updraft, and Ogura and Liou also show a weaker buoyancy maximum aloft. This structure agrees well

with the buoyancy fields of the fastest growing modes, shown in Fig. 4.15 and 4.20. The relative strength of the upper level buoyancy maximum compared to the low level minimum is somewhat larger than what is shown in Ogura and Liou; part of the observed buoyancy minimum, however, is due to convective scale evaporative cooling, an effect not included in the simulated buoyancy fields.

Finally, the perturbation pressure field at the surface would appear to a stationary observer as a lowering of pressure before passage of the squall line, followed by a pressure rise behind the leading edge. Although the horizontal structure of actual pressure variations is less uniform than what can be represented with a single plane-wave solution, the important features are in good agreement.

In summary then, the gross features of the circulation pattern and the buoyancy and pressure distribution of observed squall lines and model generated solutions are in good agreement.

5.2 Orientation angles and phase speeds

The phase speed and the orientation angle of a squall line are much easier to determine than details of its stucture; surprisingly, there have been no systematic studies of these parameters reported in the literature, other than for single case studies, until very recently. In the following, two such studies, based on independent data sets, will be used to determine characteristic values of orientation angle and phase speed.

Bluestein and Jain (1984, hereafter referred to as B) compiled characteristics of 42 severe (according to National Weather Service

criteria) squall lines that occurred in the months of April, May and June in Oklahoma, over an eleven-year period from 1971-1981. Squall lines[1] were identified and tracked from high time resolution photographs of weather radar screens. The properties of the environment were obtained from atmospheric sounding data, which was interpolated in time and space when necessary. They categorized their squall line cases into different types, based on the development of their radar echoes. "Broken line" storms formed from a line of discrete cells by a merger of the individual cells; "back builder" storms were formed by upstream development of new cells and subsequent merger with the old cells; "broken areal" formation was characterized by the transformation of an amorphous area of cells into a solid line; "embedded areal" lines were convective lines within a larger area of weak precipitation. Fig. 5.1 shows their result in the form of mean hodographs, in squall-line relative coordinates. The environmental winds for each case were transformed to a coordinate system that moved with the squall line and whose x-axis was in the direction of propagation; the result was then averaged over all cases in the sample. In Fig. 5.1, the v-axis corresponds to the squall line axis, and the angle between a line tangent to the wind profile and the v-axis is the orientation angle α used in the model. The squall line phase speed relative to the low-level flow is given by the distance between the lower endpoint of the wind profile and the v-axis. Examination of the hodographs reveals one

---

1) Squall lines were defined as echoes that form a pattern with a length-to-width ratio greater or equal to 5, a length of at least 50 km, and a duration of at least 15 minutes.

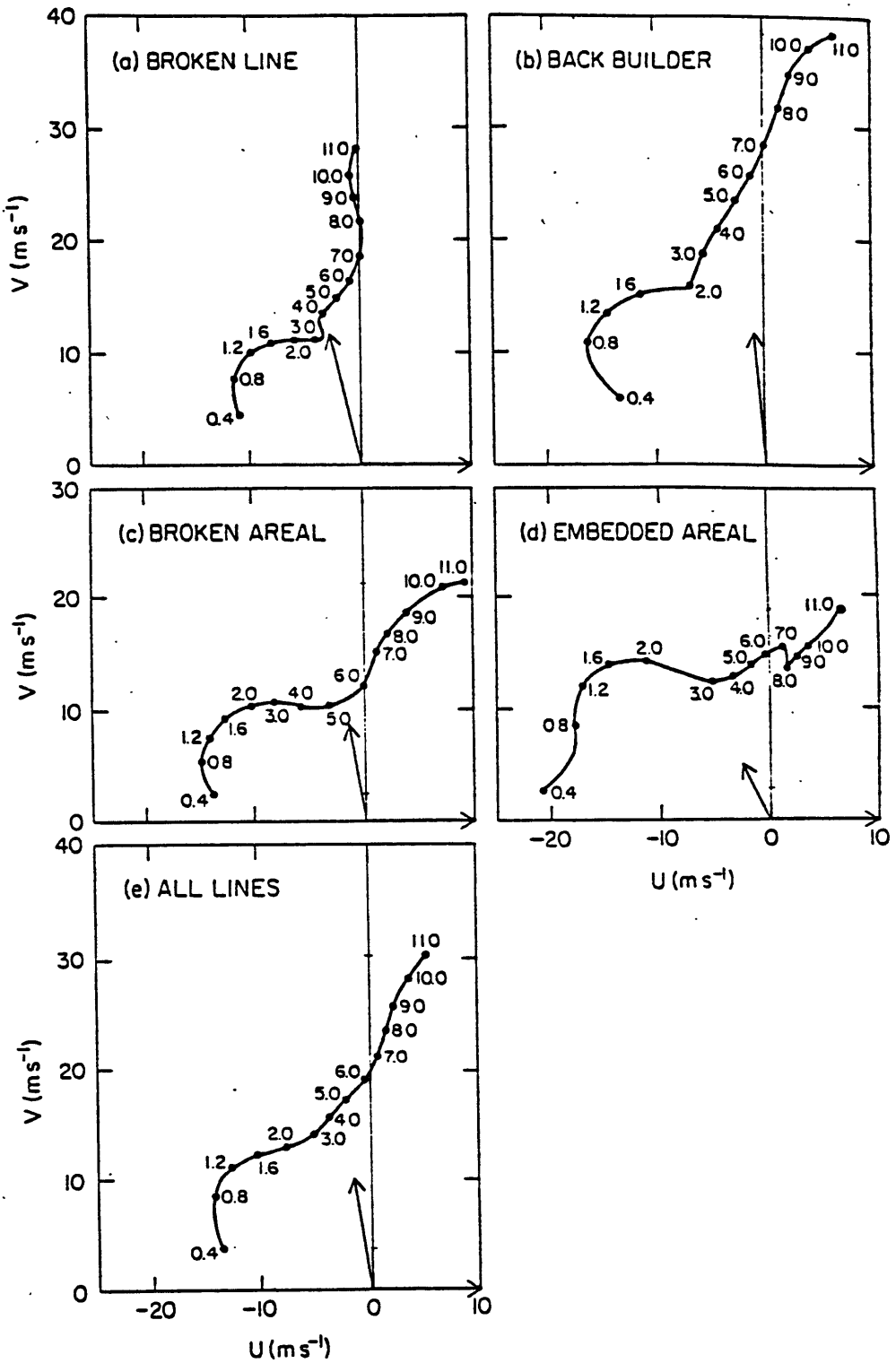

Fig. 5.1: Mean hodographs in squall line relative coordinates. The arrow indicates the cell motion. From Bluestein and Jain (1984).

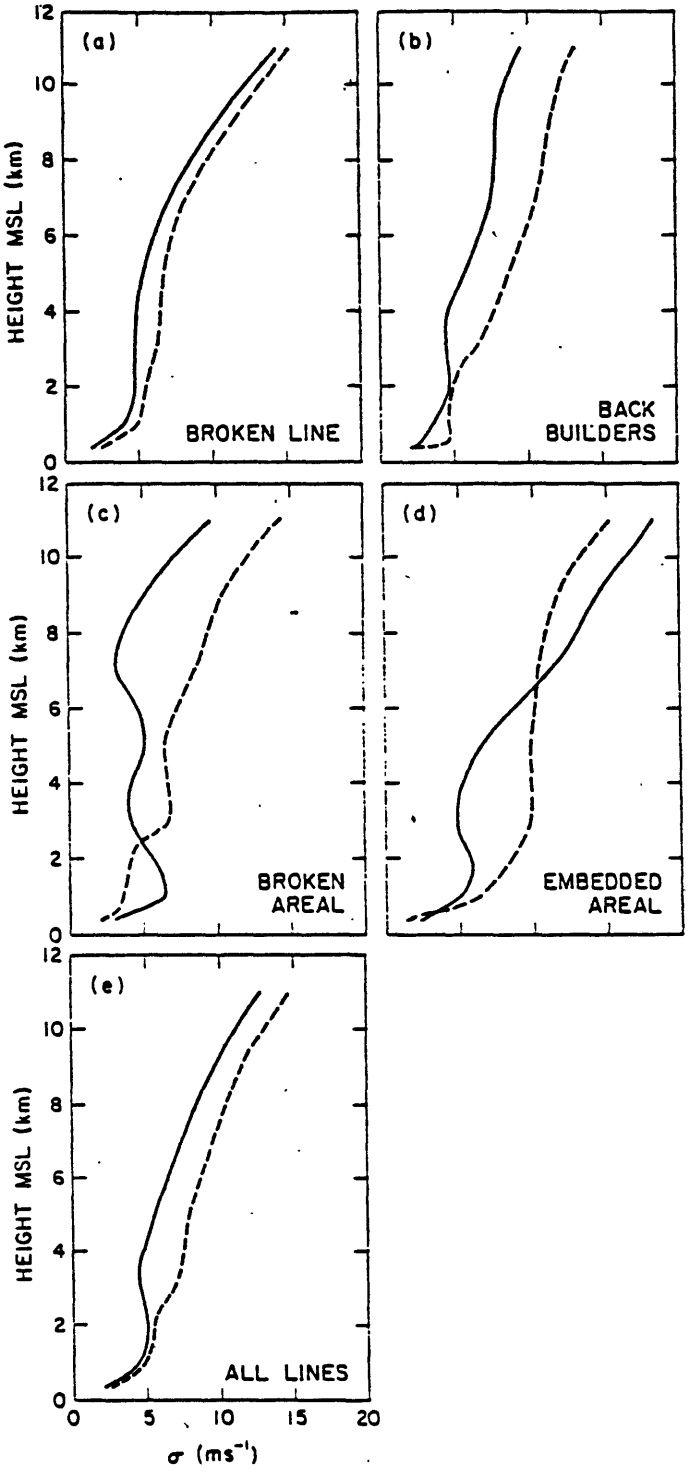

Fig. 5.2: Standard deviations of the mean hodographs in squall line relative coordinates. Solid line is the cross-line, dashed line the along-line component. From Bluestein and Jain (1984).

shortcoming of the model: the observed wind shear vector is changing direction in the lowest 2-3 km, and its magnitude is decidedly smaller aloft, in contrast to the idealized linear wind profile used in the model. Another noteworthy feature is the existence of a steering level at a height of 6-7 km.

The standard deviations are shown in Fig. 5.2. They increase with height, from less than 3 m/s to over 10 m/s. While part of this increase is due to larger measurement errors aloft, it also indicates that the low level environmental wind profile exerts more of a control on squall line propagation speed and orientation than that at upper levels. The standard deviation of the along-line component of velocity is generally larger than that of the cross-line component.

Table 5.1 summarizes the main features of Fig. 5.1: the mean magnitude of the vertically averaged wind shear, the mean and the standard deviation of the phase speed, and the orientation angle α. There are only minor differences between the different categories, and the overall average is a good representation of the subsamples with the exception of the "embedded areal" category. Since this category is the least common of all types, I will concentrate on the remaining categories as represented by the overall average. The mean thermodynamic sounding of B (not shown here) corresponds to mean tropospheric and stratospheric Brunt-Väisälä frequencies of $N_t=0.96\times10^{-2}$ s^{-1} and $N_s=1.9\times10^{-2}$ s^{-1}. The model parameters corresponding to the overall average of B are thus:

Ri=10, N_s/N_t=2, with solutions at α=+35° and a phase speed of 14 m/s.

Table 5.1: Properties of squall lines and their environment in Bluestein and Jain (1984).

Type	No. of cases	Squall line speed (m/s) Mean and stand. dev.	Mean shear ($ms^{-1}km^{-1}$)	Mean angle α
All Lines	40	13.7 ∓ 2	3.2	+35°
Broken Line	14	11.3 ∓ 2	2.5	+25°
Back Builder	13	13.4 ∓ 2	3.1	+31°
Broken Areal	8	14.2 ∓ 3	2.9	+39°
Embedded Areal	5	21.1 ∓ 2	3.0	+60°

Wyss and Emanuel (1984, hereafter referred to as W) used a different dataset and a different method in their squall line climatology. Prefrontal squall lines were identified on National Weather Service (NWS) radar summary charts, based on the following criteria:

- the maximum echo strength had to be at least VIP level 3
- the squall line had to be clearly separated from any surface fronts
- the squall line had to exist for at least 1/2 hour.

The environmental geostrophic winds were determined from NWS standard level (surface, 850 mb, 700 mb, 500 mb, and 300 or 250 mb) analyses. A total of 64 cases was analyzed, which occurred in the continental United States east of the Rocky Mountains from August 1981 to November 1983. The average length of these squall lines was 330 km, with a length-to-width ratio over 5. The distance of the lines from the surface cold front varied from 100 km to 700 km. The mean hodograph and the associated

standard deviations of the 64 cases are shown in Fig. 5.3. There are some important differences and similarities with B. In both cases, squall lines are rotated counterclockwise from the mean shear vector, and they have a steering level in the upper troposphere. The steering level is somewhat higher in W, the orientation angle is larger, and the environmental shear is much smaller. The standard deviations are generally larger than those in B, especially at lower levels; this reflects larger measurement errors of winds and phase speeds. Correlations of squall line orientation and wind shear direction were computed for all layers and were found to be largest for low-level shears, confirming the conclusions drawn from B's standard deviation profiles.

The data of W were analyzed further in an attempt to isolate those cases that had an environment most similar to the model basic state, i.e. those with an approximately linear wind profile. Subsamples of the data set were selected based on the criterion that the wind shear in each layer did not differ from the vertically averaged wind shear by more than a threshold value, which was given either in absolute terms ($ms^{-1}km^{-1}$), or as a fraction of the vertically averaged shear of each wind profile. The results are shown in Table 5.2. The orientation angle decreases somewhat as the threshold value is lowered, and the environmental shear is increased (decreased) as the relative (absolute) threshold value becomes lower. If the criterion is changed to require layer shears to be equal to the vertically averaged shear within the absolute and relative threshold value, cases which comply with only one of the criteria because of extremely small or large tropospheric shears are eliminated. The results from that analysis, shown in the last four rows of Table 5.2, again show a decrease of orientation angle and an increase of the shear value with

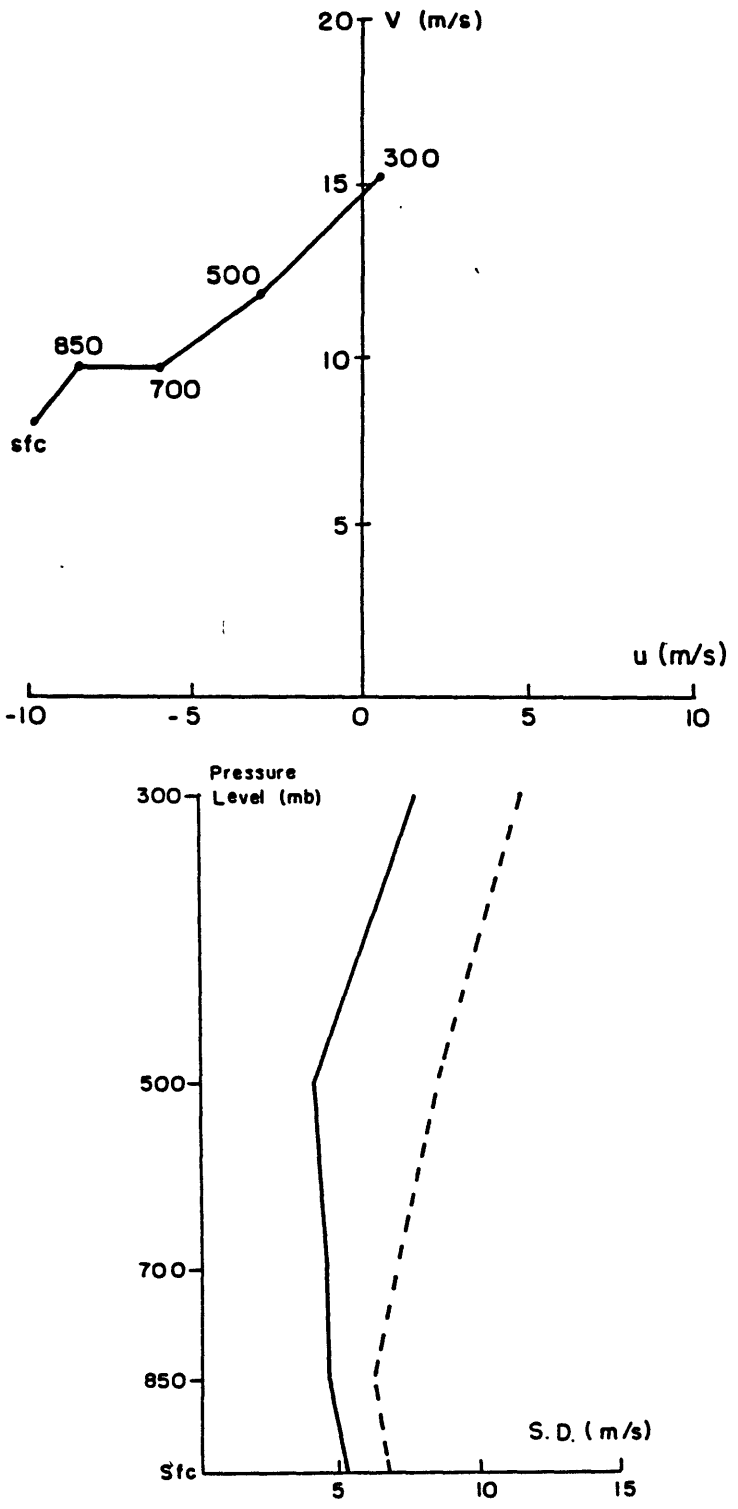

Fig. 5.3: Mean hodograph and associated standard deviations (solid line u, dashed line v) in squall line relative coordinates for all 64 cases. Data taken from Wyss and Emanuel (1984).

Table 5.2: Properties of squall lines and their environment in Wyss and Emanuel (1984).

Criterion	No. of cases	Squall line speed (m/s) Mean and stand. dev.	Mean shear ($ms^{-1}km^{-1}$)	Mean angle α
None	64	9.8 ∓ 5	1.3	+55°
5 $ms^{-1}km^{-1}$	47	9.2 ∓ 5	1.3	+52°
4 $ms^{-1}km^{-1}$	42	9.2 ∓ 6	1.3	+52°
3 $ms^{-1}km^{-1}$	26	8.0 ∓ 5	1.5	+45°
2 $ms^{-1}km^{-1}$	10	8.2 ∓ 4	1.0	+48°
4× mean shear	46	10.5 ∓ 6	1.6	+58°
3× mean shear	41	10.0 ∓ 6	1.5	+54°
2× mean shear	28	10.2 ∓ 5	1.6	+49°
1× mean shear	6	10.5 ∓ 5	2.6	+41°
5 $ms^{-1}km^{-1}$ 4× mean shear	38	9.6 ∓ 6	1.5	+52°
4 $ms^{-1}km^{-1}$ 3× mean shear	35	9.6 ∓ 6	1.5	+51°
3 $ms^{-1}km^{-1}$ 2× mean shear	20	9.3 ∓ 4	1.8	+44°
2 $ms^{-1}km^{-1}$ 1× mean shear	2	6.4 ∓ 8	2.1	+32°

decreasing threshold values. For the purpose of comparison with the model results, I choose the subsample with the strictest possible criterion that still consists of a large enough number of cases to produce a meaningful average. This subsample consists of 20 cases, with layer shears equal to the tropospheric shear to within less than 3 $ms^{-1}km^{-1}$ and twice the tropospheric shear. The mean hodograph and the standard deviations for this subsample are shown in Fig. 5.4. The environment is characterized by a shear of 1.8×10^{-3} s^{-1}, which corresponds to a Richardson number of 30 if we assume the same Brunt-Väisälä frequency as in B. The mean squall line characteristics correspond to a solution with an orientation angle of +45° and a phase speed of 9 m/s.

The results of the wave-CISK calculations in the previous chapter show growing modes at the observed orientation angles (+35° to +45°) only for heating profiles with maximum heating in the upper troposphere (z_m=0.7 and z_m=0.8). Even with those heating profiles, fastest growth occurred at zero or negative orientation angles; if evaporative cooling at low levels is included, the fastest growing mode is rotated counterclockwise from the shear vector, although by much less than observed. This suggests that if the wave-CISK model is to predict correctly orientation angles, a heating profile with upper level heating and low-level cooling has to be used.

The simulation of the squall line features described by B was undertaken with a choice of Ri=10 and N_s/N_t=2 for the model basic state parameters. Heating profiles with upper level heating and low level cooling were selected because of the knwon tendency toward positive angles of fastest growth for those profiles. For z_m=0.8, and for a heating amplitude that corresponds to a 90% efficiency in the abscence of

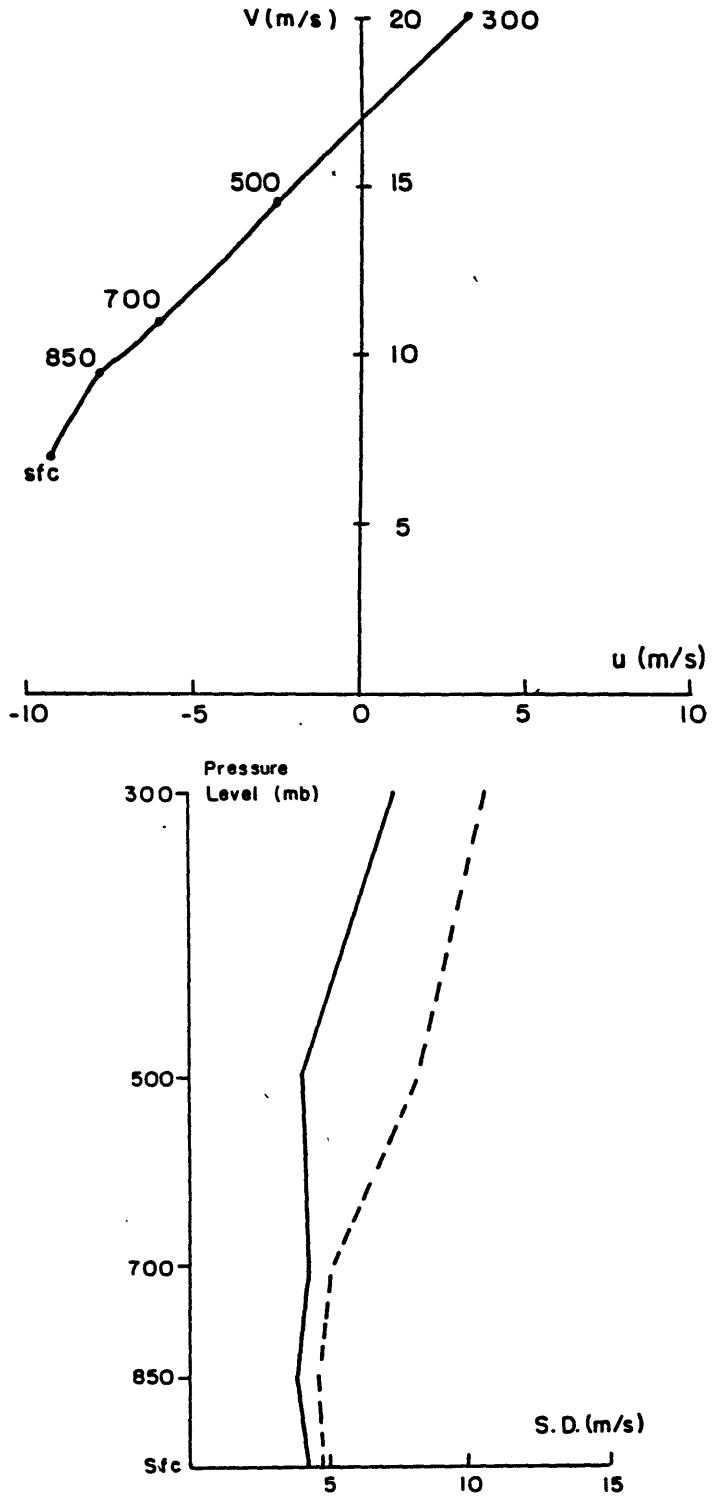

Fig. 5.4: As Fig. 5.3, but for the 20 case subsample with more nearly linear shear. Data taken from Wyss and Emanuel (1984).

cooling, the orientation angle can be increased beyond +15° by increasing the cooling strength β above 1/3. For β=0.6 and β=0.7, the orientation angle is +25°, still 10° less than that observed in B. A further increase of α is achieved by choosing a heating profile with z_m=0.9. In this case, the short wave cutoff is removed for α>60°; reducing the heating amplitude to a value of 85% efficiency for β=0 restores the finite length scale of fastest growth. The corresponding growth rate value is lower than that in the previous calculation with z_m=0.8. With the decreased heating amplitude, the orientation angle of fastest growth varies from +20° for zero cooling to +30° for β=0.5. The angle does not increase beyond +30°, even for values of β as large as 0.7. Variations of the cooling strength influence other parameters as well. The maximum growth rate decreases with increased low level cooling, and the phase speeds generally increase slightly.

The observed orientation angle of +35° is thus not reproduced here as the angle of fastest growth, even for extreme values of the heating profile parameters; it comes to within 5° of the observed value, however, which is a reasonably good agreement in light of the measurement errors and the variability in the data. The phase speeds of the growing modes at +35° are predicted to be quite large: their lower limit for z_m=0.9 and β=0.5 is 40 m/s, assuming a tropospheric depth H of 10 km. The lowest value of this lower limit is predicted for a heating profile with z_m=0.8 and zero cooling; the reference calculations of the previous chapter (recall that N_s/N_t does not affect the phase speed) show this value to be approximately 33 m/s, which is still more than twice the observed value. Thus even the lower limits of the phase speeds at +35° are larger than the observed values by a factor of 2.4 to 2.9.

The results of W are even more difficult to reproduce than those of B, because the orientation angle of the most unstable mode is smaller for larger Richardson numbers (see table 4.3). For a heating profile with z_m=0.8, and basic state parameters Ri=30 and N_s/N_t=2, the predicted orientation angle is below +10° for an evaporative cooling strength β of 1/3 or less; it is equal to +10° for β=0.4 and β=0.5, and equal to +15° for β=0.6 and β=0.7. Somewhat larger angles are again predicted if a heating profile with z_m=0.9 is chosen. A finite length scale of fastest growth is predicted for this heating profile and for a heating amplitude that corresponds to a 90% efficiency for zero cooling, in contrast to the results at Ri=10. If the cooling strength is increased to 0.5, the orientation angle is increased to +20°; a further increase of β up to 0.7 does not result in any change of α_{max}, however. Thus, the observed angle of +45° cannot be reproduced as the angle of fastest growth.

As was the case for Ri=10, there are growing modes at +45° with phase speeds that are larger than those observed. The lower limit of the phase speed at α=+45° is 35 m/s for z_m=0.8 and β=0.4. This value increases to 43 m/s for z_m=0.9 and β=0.5. Compared to the observed value of 9 m/s this is an overestimate by a factor of 3.9 to 4.9.

The results of this model thus do not agree with the phase speed and orientation angle data of two independent observational studies of midlatitude squall lines. While in the case of B the orientation angle can be made reasonably close to observed values, the predicted angle disagrees with that of W by 25°. In either case the predicted phase speeds at the observed orientation angles are too large, by a factor of 2.4 to 4.9. The implications of this discrepancy will be discussed in the next chapter.

6. Conclusions

A linear wave-CISK model has been developed for two-dimensional perturbations in a baroclinic basic state with constant vertical wind shear. The model allows for arbitrary orientation angles of the disturbance axis. Different forms of the vertical profile of convective heating have been used in the model.

Results show the existence of two growing modes in the model, a convectively amplified baroclinic instability (Eady) mode, and a smaller scale wave-CISK mode.

The Eady mode has its largest growth rate along the baroclinic axis, with dimensional values of wavelength and e-folding time on the order of 3600 km and 26 hours, respectively. Its growth rate is only slightly higher than that of the adiabatic instability, and it is largest for a sinusoidal vertical heating profile (z_m=0.5). The effects of heating on the Eady mode found here agree qualitatively with Mak's (1982) results.

The wave-CISK mode is the continuation to general orientation angles of the wave-CISK mode along the symmetric axis found by Emanuel (1982). The largest growth rate occurs near, but in general not on, the symmetric axis. The wavelength of fastest growth is on the mesoscale, with dimensional values (for the reference run) between 630 km and 450 km, and corresponding e-folding times on the order of 20 hours. The fastest growing mode propagates upshear unless a heating profile with maximum heating near the tropopause is used; if the effects of low level evaporative cooling are included, downshear propagation is predicted. The dimensional wavenumber and growth rate of the fastest growing mode are approximately proportional to the magnitude of the environmental shear. The phase speed of the wave-CISK mode corresponds to that of an

inertio-gravity wave that extends through approximately half the depth of the troposphere.

The vertical structure of the wave-CISK modes is characterized by a nearly upright circulation cell in the lower part of the domain and streamlines that are sloping back with height aloft. The lower circulation cell is similar to a neutral, trapped gravity wave. Generation of eddy available potential energy by convective heating, which is proportional to the correlation of perturbation buoyancy and heating, is the single most important energy source; the loss of energy to the stratosphere is an energy sink that becomes important at large wavenumbers.

The vertical structure is sensitive to the heating profile, the total wavenumber, and the orientation angle. A larger wavenumber ℓ and a higher level of maximum heating z_m both lead to a deeper disturbance in the sense that the lower circulation cell occupies a larger portion of the domain, and that the perturbation amplitude at upper levels is increased. This is accompanied by an increase of the energy loss to the stratosphere, and a decrease of that part of the domain in which the energy generation by convective heating is positive. A cross-line shear directed against the propagation of the squall line leads to a shallower disturbance. As a result of these different dependencies, the fastest growing mode is rotated clockwise by 30° for a sinusoidal heating profile, and by progressively smaller angles for higher levels of maximum heating; this change in α is accompanied by a small decrease in the wavenumber of fastest growth.

Sensitivity experiments establish the variation of the wave-CISK results for heating profiles without low level cooling over a large range

of heating amplitudes, stratospheric stabilities, and bulk Richardson numbers. The barotropic wave-CISK result of growth rates that are monotonically increasing with wavenumber is reproduced for heating amplitudes that correspond to large precipitation efficiencies (E>90%). For precipitation efficiencies below 30%, no growing wave-CISK modes exist. The orientation angle of the fastest growing mode shows a tendency for a clockwise rotation as the heating amplitude and the stratospheric stability are decreased, and as the Richardson number is increased. The growth rate and the wavenumber of the fastest growing mode are found to decrease with decreasing static stability of the stratosphere.

The comparison with observations shows some aspects of the solutions, such as the major circulation features, to be in general agreement. Wavelengths of the fastest growing mode are on the mesoscale, but the half-wavelengths exceed observed squall line widths. The growth rates predicted by the model are too small for the observed rapid intensification of squall lines, so that the wave-CISK mechanism is only applicable to the maintenance of the developed circulation. Growing modes at the observed average orientation angles of +35° to +45° exist for heating profiles with heating maxima at or above 0.7. The fastest growing mode occurs near the correct orientation angle only for heating profiles with maximum heating in the extreme upper troposphere and with a substantial amount of low level cooling. The predicted phase speeds at those orientation angles are too large by a factor of 2 to 5 compared to observed squall line speeds. This disagreement is so large that the wave-CISK theory, at least in its current formulation, has to be rejected because it cannnot properly account for the observed characteristics of atmospheric squall lines.

This failure of wave-CISK theory may be indicative of a fundamental flaw in the basic wave-CISK hypothesis, or it could be related to relatively minor defects of this specific model, such as an oversimplification of the basic state or the convective parameterization. Arguments for either point of view could be constructed.

In defense of wave-CISK theory one might argue that it is not essential that the fastest growing mode have the correct orientation angle as long as there is some nonzero growth at that angle, because the small growth rates make it unlikely that only the fastest growing mode would be observed in nature. This would relax the restrictions on the permissible heating profiles somewhat, although the maximum heating would still have to occur in the upper troposphere. The rather substantial disagreement in phase speeds still remains, however. The squall line relative mean hodographs presented in chapter 5 show that squall line environments are systematically different from the simple linear wind profile used in the model basic state. However, the properties of the subsample of W with more nearly linear wind profiles did not agree with model predictions either, suggesting that the reason for the disagreement is not due to the use of a linear wind profile. In the discussion of other model features it is instructive to consider the results of Raymond (1983,1984). His model differs from the one used here in two major aspects: the Coriolis force is neglected in his model, and he includes time lag effects in the parameterization of updraft and downdraft related heating and cooling. Because of the neglect of the earth's rotation, only the cross-line shear of the basic state affects his solution. His results show upshear and downshear propagating modes with phase speeds that are not influenced strongly by the cross-line shear; the downshear propagating mode has a

phase speed that is in general agreement with observations. It is unclear whether this improved agreement with observations is due to the neglect of the possibly important Coriolis effect, or due to the more realistic cumulus parameterization. His model results, however, have the common wave-CISK problem not encountered in the model here: growth rates increase monotonically with wavenumber, thus raising serious doubts as to whether the parameterization of convective effects is appropriate while dry circulations of the same scale are resolved explicitly. Despite these problems, his results at least raise the possibility that more realistic phase speeds could be obtained with the present model if time-lag effects were included in the convective parameterization.

One of the fundamental problems of the wave-CISK concept is the fact that the growth of the disturbance depends on convective heating of relatively warm air at upper levels, and, if low level cooling is included, cooling of cold air at low levels. Thus, for optimum growth of the mesoscale circulation the convection has to occur in that part of the wave that is the least conducive to convection, namely the statically most stable region. This somewhat paradoxical requirement is quite general and not limited to this specific wave-CISK model. In addition, the use of linear wave-CISK for the maintenance and not the initial growth stage of squall lines may not be appropriate since finite amplitude effects are likely to become more important in that part of the life-cycle. Finally, one may question if the forcing of convection is adequately represented by the low level convergence of the mesoscale circulation; indeed, the apparent failure of wave-CISK demonstrated here might be interpreted as proof that it is not.

Future research should attempt to establish whether minor modifications and refinements of the wave-CISK model lead to better agreement with the observations, or whether the simple wave-CISK approach is altogether inappropriate for midlatitude squall lines. The sensitivity of the results to the details of the heating parameterization indicates that refinements should concentrate on the cumulus parameterization. The neglect of cumulus momentum fluxes is not likely to play a large role, as results from Stevens and Lindzen (1978) and Raymond (1984) suggest. The inclusion of time lags in the heating response to the forcing, however, might lead to more realistic phase speeds. Preliminary calculations with the present model show a reduction in phase speed for the phase lag formulation of Davies (1979), but by less than 27% for time lags of one hour or less. This reduction is still insufficient to lead to realistic phase speeds, indicating that time lags in the heating would have to be unreasonably large for a better agreement of predicted and observed phase speeds. Before more complete calculations with time lags are carried out, however, this conclusion is still speculative.

One may further speculate what other aspects of the wave-CISK theory are unrealistic and lead to its failure. A crucial point may be the normal mode assumption, with the associated problem of "negative clouds". Since observed squall lines generally occur alone and not in a series, they are more properly represented by a wave-packet rather than a single Fourier component. The presence of several wave components will inevitably lead to wave-wave interactions, both directly (through nonlinear advection) and indirectly (through the stabilization of the basic state). Neither of these processes is present in the linear wave-CISK model described here. The importance of these different factors

could be ascertained with a series of progressively more complex models, in which the negative cloud assumption is removed, more than one Fourier component is computed, and finally wave-wave and wave-mean flow interactions are considered.

References:

A. Arakawa and W. Schubert, 1974: Interaction of a cumulus ensemble with the large scale environment, part I. J. Atmos. Sci., 37, 674-701.

Bluestein, H.B., and M.H. Jain, 1984: The formation of mesoscale lines of precipitation: severe squall lines in Oklahoma during the spring. Submitted to J. Atmos. Sci.

Bolton, 1980: Application of the Miles theorem to forced linear perturbations. J. Atmos. Sci., 37, 1639-1642.

Bradberry, J.S., 1981: Mesoscale structure of an Oklahome squall line. Mon. Wea. Rev., 109, 1110-1117.

Breiland, J.-G., 1958: Meteorological conditions associated with the development of instability lines. J. Meteor., 15, 297-302.

Bretherton, F.P., 1966: The propagation of groups of internal gravity waves in shear flow. Quart. J. Roy. Meteor. Soc., 92, 466-480.

Browning, K.A. ,and F.H. Ludlam, 1962: Airflow in convective storms. Quart. J. Roy. Meteor. Soc., 88,117-135.

Chang, C.B., D.J. Perkey, and C.W. Kreitzberg, 1981: A numerical case study of the squall line of 6 May 1975. J. Atmos. Sci., 38, 1601-1615.

Charney, J.G., and A. Eliassen, 1964: On the growth of the hurricane depression. J. Atmos. Sci., 21, 68-75.

Daniels, R.W., 1978: An introduction to numerical methods and optimization techniques. Elsevier North-Holland, Inc., New York.

Davies, H.C., 1979: Phase-lagged wave-CISK. Quart. J. Roy. Meteor. Soc., 105, 325-353.

Eady, E.T., 1949: Long waves and cyclone waves. Tellus, 1, 33-53.

Emanuel, K.A., 1982: Inertial instability and mesoscale convective systems. Part II: Symmetric CISK in a baroclinic flow. J.

Atmos. Sci., 39, 1080-1097.

Fritsch, J.M., C.F. Chappell, and L.K. Hoxit, 1976: The use of large scale budgets for convective parameterization. Mon. Wea. Rev., 104, 1408-1418.

Fulks, J.R., 1958: The instability line. Compendium of Meteorology, Amer. Meteor. Soc., Boston.

Hane, C.E., 1973: The squall line thunderstorm: numerical experimentation. J. Atmos. Sci., 30, 1672-1690.

Hayashi, 1971: Instability of large-scale equatorial waves with a frequency dependent CISK parameter. J. Meteor. Soc. Japan, 49, 59-62.

Hoxit, L.R., C.F. Chappell, and J.M. Fritsch, 1976: Formation of mesolows or pressure troughs in advance of cumulonimbus clouds. Mon. Wea. Rev., 104, 1419-1428.

Jones, W.L., 1967: Propagation of internal gravity waves in fluids with shear flow and rotation. J. Fluid Mech., 30, 439-448.

Kuo, H.L., 1978: A two-layer model of the combined barotropic and baroclinic instability in the tropics. J. Atmos. Sci., 35, 1840-1860.

Lindzen, R.S., 1974: Wave-CISK in the tropics. J. Atmos. Sci., 31, 156-179.

Lindzen, R.S., and K.K. Tung, 1976: Banded convective activity and gravity waves. Mon. Wea. Rev., 104, 1602-1617.

Lord, S.J., 1982: Interaction of a cumulus cloud ensemble with the large-scale environment. Part III: semi-prognostic test of the Arakawa-Schubert cumulus parameterization. J. Atmos. Sci., 39, 88-103.

Mak, M., 1982: On moist quasi-geostrophic baroclinic instability. J. Atmos. Sci., 39, 2028-2037.

Matsuno, T., 1966: Quasi-geostrophic motions in the equatorial area. J. Meteor. Soc. Japan, 44, 25-43.

Miller, D.A., and F. Sanders, 1980: Mesoscale conditions for the severe convection of 3 April 1974 in the East Central United States. J. Atmos. Sci., 37, 1041-1055.

Moncrieff, M.W., 1981: A theory of organized steady convection and its transport properties. Quart. J. Roy. Meteor. Soc., 107, 29-50.

Moorthi, S., 1983: Baroclinic and barotropic instability with cumulus heating and tropical cyclogenesis. Ph. D. Thesis, UCLA, Los Angeles, CA.

Newton, C.W., 1966: Circulations in large sheared cumulonimbus. Tellus, 18, 699-713.

Newton, C.W., 1950: Structure and mechanism of the prefrontal squall line. J. Meteor., 7, 210-222.

Newton, C.W., and H.R. Newton, 1959: Dynamical interactions between large convective clouds and environment with vertical shear. J. Meteor., 16, 483-496.

Ogura, Y., and M.-T. Liou, 1980: The structure of a mid-latitude squall-line: A case study. J. Atmos. Sci., 37, 553-567.

Ooyama, K., 1964: A dynamical model for the study of tropical cyclone development. Geofis. Intern., 4, 187-198.

Raymond, D.J., 1984: A wave-CISK model of squall lines. J. Atmos. Sci., 41, 1946-1958.

Raymond, D.J., 1983: Wave-CISK in mass flux form. J. Atmos. Sci., 40, 2561-2572.

Raymond, D.J., 1976: Wave-CISK and convective mesosystems. J. Atmos. Sci., 33, 553-567.

Raymond, D.J., 1975: A model for predicting the movement of continuously propagatong storms. J. Atmos. Sci., 32, 1308-1317.

Reed, R.J., and E.E. Recker, 1971: Structure and properties of synoptic-scale wave disturbances in the equatorial Western Pacific. J.

Atmos. Sci., 28, 1117-1133.

Schlesinger, R.E., 1973: A numerical model of deep moist convection: Part I. Comparative experiments for variable ambient moisture and wind shear. J. Atmos. Sci., 30, 835-856.

Seitter, K.L., and H.-L. Kuo, 1983: The dynamical structure of squall-line type thunderstorms. J. Atmos. Sci., 40, 2831-2854.

Stark, T.E., 1976: Wave-CISK and cumulus parameterization. J. Atmos. Sci., 33,2383-2391.

Stone, P.H., 1970: On nongeostrophic baroclinic instability: Part II. J. Atmos. Sci., 27, 721-726.

Stone, P.H., 1966: On nongeostrophic baroclinic instability. J. Atmos. Sci., 23, 390-400.

Thorpe, A.J., M.J. Miller, and M.W. Moncrieff, 1982: Two-dimensional convection in non-constant shear: a model of midlatitude squall lines. Quart. J. Roy. Meteor. Soc., 108, 739-762.

Wilhelmson, R.B., and J.B. Klemp, 1981: A three-dimensional numerical simulation of splitting severe storms on 3 April 1964. J. Atmos. Sci., 38, 1581-1600.

Wyss, J., and K.A. Emanuel, 1984: to be submitted to Mon. Wea. Rev.

Zipser, E.J., 1977: Mesoscale and convective-scale downdrafts as distinct components of squall-line structure. Mon. Wea. Rev., 105, 1568-1589.

Appendix A: Numerical Procedures

A.1 Numerical integration

The complex frequency σ is computed as the eigenvalue of a generalized matrix problem. This is accomplished by writing eq.(3.10) in finite difference form. Eq.(3.10) is of the form

$$\psi_{zz} + a\psi_z + b\psi = c\psi(z_o) \ , \qquad (A.1)$$

where the coefficients a, b, and c are known functions of σ, ℓ, α, and z. We now solve this equation on a grid with $z_n=(n-1)\Delta z$, and approximate derivatives by centered differences:

$$\psi_{zz} = \frac{\psi_{n+1} - 2\psi_n + \psi_{n-1}}{(\Delta z)^2}$$

$$\psi_z = \frac{\psi_{n+1} - \psi_{n-1}}{2\Delta z}$$

Then we can write (A.1) as

$$A_n\psi_{n+1} + B_n\psi_n + C_n\psi_{n-1} = D_n\psi_m \ , \qquad (A.2)$$

where

$$A_n = 1 + a_n\Delta z/2$$

$$B_n = -2 + b_n(\Delta z)^2$$

$$C_n = 1 - a_n\Delta z/2$$

$$D_n = c_n \ ,$$

and where m denotes the grid level at which $z_m=z_o$. Eq. (A.2) is valid for n=2,3,...,N, where N=1/Δz. N, the number of levels in the vertical, has been set to 100 for all computations reported here. Sensitivity tests showed the eigenvalue to be quite insensitive to N for this value, while errors on the order of a few percent appeared for N below 50.

At the boundaries, a finite difference form of (3.12) and (3.18) is used. At z=0, the appropiate equation is simply

$$\psi_1 = 0 \quad , \tag{A.4}$$

which is equivalent to (A.2) with $A_1=C_1=D_1=0$, and $B_1=1$. At z=1, i.e. n=N+1, the radiation condition (3.18) is

$$\psi_z(1-) = d\psi(1-) \quad ,$$

where d is a known function of model parameters. In finite difference form this equation is written as

$$B_{N+1}\psi_{N+1} + \psi_N = 0 \quad , \tag{A.5}$$

which is a form of (A.2) with $A_{N+1}=D_{N+1}=0$, $C_{N+1}=1$, and

$$B_{N+1} = d\Delta z(1 + a_{N+1}\Delta z/2) - (1 - \Delta z^2 b_{N+1}/2) \quad .$$

We can now combine equation (A.2) with the boundary conditions (A.4) and (A.5) into a single matrix equation

$$\tilde{\mathbf{L}}\,\vec{\psi} = \vec{\mathbf{D}}\,\psi_m \quad , \tag{A.6}$$

where $\tilde{L}$ is an (N+1)×(N+1) tridiagonal matrix given by

$$L_{ij} = \begin{cases} 0 & \text{for } j<i-1 \text{ and } j>i+1 \\ C_i & \text{for } j=i-1 \\ B_i & \text{for } j=i \\ A_i & \text{for } j=i+1 \end{cases} ,$$

$\vec{\psi}$ is the column vector $(\psi_1,\ldots,\psi_{N+1})^T$, and $\vec{D}=(D_1,\ldots,D_{N+1})^T$. We can remove the inhomogeneity in (A.6) by bringing the forcing term on the left hand side of the equation:

$$\tilde{L}\,\vec{\psi} - \vec{D}\,\psi_m = \tilde{M}\,\vec{\psi} = 0 \quad . \tag{A.7}$$

The matrix $\tilde{M}$ is identical to $\tilde{L}$ except that all elements L_{im} in column m are altered by subtracting D_i. Nontrivial solutions to (A.7) exist only if

$$\det\left|\tilde{M}\right| = 0.$$

The eigenvalue of the problem is that value of σ for which the corresponding coefficient values A_i, B_i, C_i, D_i result in a zero determinant of matrix $\tilde{M}$. We determine the eigenvalues iteratively by adjusting subsequent guesses for σ to produce smaller values of $\det\left|\tilde{M}\right|$. The iteration procedure is described in the next section.

The calculation of the determinant is facilitated by the special form of the matrix $\tilde{M}$. We can eliminate the elements in column m in rows 2 through m-2 in two elimination steps. First, we multiply row i+1 by D_i/D_{i+1}, and subtract the result from row i:

$$M_{ij}^{(1)} = M_{ij}^{(0)} - M_{i+1,j}^{(0)} D_i / D_{i+1} \quad . \tag{A.8}$$

This operation is performed on rows 2 through m-3. The resulting matrix has one element (R_i) to the right of the upper diagonal in rows 2 through m-2, which is given by

$$R_i = \begin{cases} -D_i & \text{for } i=m-2 \\ -A_{i+1} D_i / D_{i+1} & \text{for } i=2,3,\ldots,m-3 \end{cases} \quad .$$

This element is eliminated by performing the following operation on rows m-2 through 2:

$$M_{ij}^{(2)} = M_{ij}^{(1)} - M_{i+1,j}^{(2)} R_i / R_{i+1} \quad . \tag{A.9}$$

Here $M_{ij}^{(2)} = M_{ij}^{(1)} = M_{ij}^{(0)}$ for $i>m-2$, and $M_{ij}^{(1)} = M_{ij}^{(0)}$ for $i=m-2$. In the case of zero heating all elements D_i are zero, and steps (A.8) and (A.9) are omitted. A final Gaussian elimination step, performed sequentially on rows N,N-1,...,2, brings the matrix into a lower triangular form:

$$M_{ij}^{(3)} = M_{ij}^{(2)} - M_{i+1,j}^{(3)} M_{i,i+1}^{(2)} / M_{i+1,i+1}^{(3)} \quad . \tag{A.10}$$

Here $M_{ij}^{(3)} = M_{ij}^{(2)}$ for $i=N+1$. The determinant of this lower triangular matrix is then simply the product of the elements of the diagonal.

The calculation of the eigenvalue of a tridiagonal system was performed in this way by Seitter (1983, personal communication), who modified the eigenvalue solver described by Kuo (1978).

Once an eigenvalue has been found, the corresponding eigenfunction can easily be computed by backward substitution (see, e.g., Daniels, 1978). In the case of nonzero heating we treat the forcing as known for this purpose by assuming an arbitrary value for ψ_m. We then perform operation (A.10) on the tridiagonal matrix $\tilde{L}$, augmented by an additional column vector D. Upon completion of this step, we operate with

$$L_{ij}^{(4)} = \left[L_{ij}^{(3)} - L_{i,i-1}^{(3)} L_{i-1,j}^{(3)}\right] / L_{i,i}^{(3)}$$

on rows i=3,...,N+1. The modified column vector $\vec{D}^{(4)}$ is then identical to $\vec{\psi}$, aside from a multiplicative constant. In the case of zero heating we can directly substitute for ψ_i from one level to the next without any prior matrix transformations.

A.2 Iteration Procedure

After the determinant of the matrix $\tilde{M}$ is computed for the first guess value of σ, the calculation is repeated with new values of σ that are obtained by adding and subtracting a small, arbitrary number ε to σ. The value of σ for the next iteration is then determined from Laguerre's formula as

$$\sigma^{\nu+1} = \sigma^{\nu} - \frac{N\,R^{\nu}}{\dot{R}^{\nu} \mp \left[(N-1)^2(\dot{R}^{\nu})^2 - N(N-1)R^{\nu}\ddot{R}^{\nu}\right]^{1/2}} \quad , \qquad (A.11)$$

where the sign of the radical is taken to maximize the absolute value of the denominator. Here the supercript denotes the level of iteration, R is the value of $\det\left|\tilde{M}\right|$ for $\sigma=\sigma^{\nu}$, $\dot{R}^{\nu}$ is its derivative with respect to σ:

$$\dot{R}^{\nu} = \frac{R(\sigma^{\nu} + \varepsilon) - R(\sigma^{\nu} - \varepsilon)}{2\varepsilon} \quad , \qquad (A.12)$$

and $\ddot{R}^{\nu}$ is the second derivative of $R(\sigma)$:

$$\ddot{R}^{\nu} = \left[R(\sigma^{\nu} + \varepsilon) + R(\sigma^{\nu}) - 2R(\sigma^{\nu})\right] \quad . \qquad (A.13)$$

N is an arbitrarily selected large integer; for N=2, eq.(A.11) implies a quadratic approximation of $R(\sigma)$ near σ. Subsequent guesses of σ are obtained in the same manner, except that the arbitrary constant ε is replaced by the difference between subsequent guess values, i.e. $\sigma^{\nu}-\sigma^{\nu-1}$. The use of Laguerre's method was described in Kuo (1978); it is implemented here with a modification suggested by Seitter (1983, personal communication).

Comparisons between using (A.11) and a Newton's method formula showed that Laguerre's method requires fewer iteration and that subsequent guesses are closer to the solution than with Newton's method; for first guesses that were not very close to the solution, Laguerre's method converged and Newton's method did not in some cases. Laguerre's method has been used throughout this thesis because of this improved convergence behavior in spite of a slightly increased computation time due to an additional integration for each iteration. Laguerre's method performed better for N=10 than for N=2.

The above method will in general only converge if the first guess is sufficiently close to the solution. In this thesis, the first guesses were obtained from the known results for special values of the model parameters, i.e. those of Emanuel (1982) for $\alpha=0^\circ$ and $z_m=0.5$, and those of Stone (1970, 1966) for E=0. These results were extended to previously unexplored areas of parameter space by gradual changes of the model parameters. To insure that all growing modes were calculated, general searches for eigenvalues at specific wavenumbers and orientation angles were carried out for selected values of model parameters. In these general searches, first guesses were evenly spaced on a grid in the complex σ-plane. The grid separation was chosen such that known solutions would be converged to several times, and the range of phase speeds and growth rates of the first guesses was larger than that of the calculated eigenvalues.

Appendix B: Adiabatic modes at low Richardson numbers

The wave-CISK model described in this thesis can be used to investigate adiabatic instabilities simply by letting E=0. This was done for calculations of the adiabatic Eady modes (section 4.1.1) for a radiation boundary condition and a Richardson number of 10. Similar calculations were carried out with a rigid lid boundary condition and smaller Richardson numbers, in order to test the model by comparing its results to those of Stone (1970). The investigation of adiabatic instabilities is interesting in its own right, as well.

At Richardson numbers below 1, Stone (1970) calculated nongeostrophic instability modes with wavenumbers larger than those of the geostrophic Eady modes. These modes had their maximum growth rate along the symmetric axis, at large wavenumbers. The separate Eady growth rate maximum along the baroclinic axis was found to exceed the symmetric instability growth rate for Richardson numbers larger than 0.95. The non-geostrophic instabilities still existed for Richardson numbers equal to and larger than the critical value for symmetric instability (Ri=1), but for Ri>2 their growth rate became too small for their calculation in Stone's model.

The wave-CISK calculations described in section 4.4 uncovered growing modes at Ri=1.3 , in the presence of convective heating, that were not related to the wave-CISK modes at larger Richardson numbers. These modes had negative orientation angles and phase speeds, i.e. they propagated downshear and toward the cold air. Their growth rates became small as the heating was reduced to small values, or the Richardson number increased to moderate values.

The adiabatic results of Stone (1970) and the wave-CISK calculations

both suggested the existence of growing modes unrelated to the previously calculated Eady or wave-CISK modes at small Richardson numbers above 1. Thus a systematic exploration of adiabatic instabilities seemed warranted. As a starting point, the nongeostrophic instability calculations of Stone (1970) were repeated with the current model for Ri=0.5 and Ri=1.0. An attempt to extend these results to larger Richardson numbers failed because the growth rates became too small for Ri>1.4. Thus, an extensive general search for unstable eigenvalues was conducted for the following choice of model parameters:

$$Ri = 1.5$$

$$N_s/N_t = 3$$

$$E = 0.$$

This search was conducted at wavenumbers ℓ=0.6, 1.0, 4.0, 10.0, and 20.0, and at orientation angles $\alpha=\mp 20°$, $\mp 45°$, $\mp 75°$, and 90°. The first guesses for the eigenvalue σ were spaced apart by 0.1, ensuring that the known solutions (the Eady modes) were converged to from several first guesses. The range of σ considered for first guess values was chosen to be several times larger than the range of the known eigenvalues: growth rates of up to 2, and phase speeds of up to ∓ 3 (∓ 4 for ℓ=1.0, ∓ 5 for ℓ=0.6) were used.

The results from this search recovered the Eady modes at small wavenumbers. At ℓ=0.6 the Eady mode growth rate was nonzero for all angles, but at ℓ=1.0 only for $|\alpha|<30°$. Calculations of the Eady mode at intermediate wavenumbers and orientation angles showed the growth rate curves toward larger total wavenumbers at small α, both for a radiation and rigid lid upper boundary condition. This is in contrast to quasi-geostrophic theory, which predicts geometrically similar growth rate curves whose amplitudes are scaled by $|\sin \alpha|$. The Eady modes had a steering level in the middle of the domain.

Aside from the Eady mode, slowly growing modes were found for wavenumbers $\ell>0.6$. Their growth rates were very small, several times to one or two orders of magnitude smaller than those of the Eady mode. These modes all had a steering level and a level where the real part of the Doppler-shifted frequency was equal to +f or -f. Because of the small growth rates, the coefficients of the governing differential equation became near singular at those levels, leading to a deterioration of the convergence behavior of the numerical method. This manifested itself in the apparent convergence to several values of σ in close vicinity on the complex σ-plane, and, in cases where the singularities were near the top of the domain, in poor matching of the pressure across the tropopause. The growth rates of these modes tended to increase with wavenumber; at $\ell=20$, they reached approximately half the Eady mode value. At that wavenumber, their phase speeds approached the basic state wind speed at the top or the bottom of the domain. An analysis of the energetics of these modes showed another effect of the small values of the Doppler-shifted frequency: the energy conversion terms were all concentrated near the singularities, which in the case of moderate and large wavenumbers was a region on the order of the vertical resolution of the numerical integration scheme. The numerical calculation of the eigenvalues was thus severely limited by the singular nature of the solutions.

An attempt was made to extend the solutions at $\ell=20$ to moderate Richardson numbers. As was the case with the nongeostrophic modes discussed in Stone (1970), their growth rates decayed rapidly with increasing Richardson numbers. For Richardson numbers of 2-3, the growth rates were only a tenth of the Eady mode value.